PRESSURE EFFECTS ON THE BAND STRUCTURE AND HALL MOBILITY OF NAPHTHALENE

by

MAHMOUD A. EL HAMAMSY

A dissertation submitted to the Graduate Faculty in Physics in partial fulfillment of the requirements for the degree of Doctor of Philosophy, The City University of New York

1976

This manuscript has been read and accepted for the Graduate Faculty in Physics in satisfaction of the dissertation requirement for the degree of Doctor of Philosophy.

April 29 1976
date

Arthur C. Damask
Chairman of the Examining Committee

April 29, 1976
date

Myriam P. Sarachik
Executive Officer

Professor George J. Dienes
Professor Milton Furst
Professor Arthur Paskin
Professor Martin Pope
Professor William Whitten
Doctor Stephen Arnold

Supervisory Committee

Abstract

PRESSURE EFFECTS ON THE BAND STRUCTURE AND
HALL MOBILITY OF NAPHTHALENE

by

Mahmoud A. El Hamamsy

Advisor: Professor Arthur C. Damask

The pressure dependence, up to 5.5 kilobars, of the lattice parameters of naphthalene were determined in a neutron diffraction experiment. Assuming linear compressibilities, a possible set of elastic constants was calculated. The effect of pressure on the band structure of naphthalene was then investigated. Calculations were carried out using three different band models, obtained by taking into consideration various combinations of interactions: resonance integrals, exchange effects, and vibrational overlap. The variation with pressure of the Hall and drift mobility tensors of naphthalene were obtained in the relaxation time approximation. By assuming the relaxation time in a particular direction to be inversely proportional to the bandwidth in that direction, it is found that the anisotropies of the drift mobility tensor are in good agreement with the predictions of a band model that takes into consideration the resonance and exchange integrals, as well as the intramolecular vibrations, and for which the mean free path λ rather than the mean free time τ is constant. To verify this result, the pressure dependence, up to 2.2 kilobars, of the Hall mobility tensor of naphthalene was determined. Measurements were carried out along the directions that gave the largest Hall signal; these correspond to the current and magnetic field along either the a or b axes. Due to large uncertainties in the measurements, it was found that the variation with pressure of the Hall mobility could not be used alone to favor one band model over the other. However, the signs of the Hall mobilities of naphthalene correspond to those predicted by calculations carried out in the constant λ approximation, using a band model that takes into consideration the resonance and exchange integrals, as well as the vibrational overlap. These results, along with similar

conclusions regarding the drift mobility tensor, thus seem to favor a band conduction mechanism in naphthalene, where the mean free path, rather than the mean free time, is constant.

Acknowledgments

The author wishes to express his sincere gratitude to his advisor, Professor Arthur C. Damask. The skills and values which he imparted were as significant as his explicit help in providing the facilities, equipment, and encouragement that made this work possible.

The author also wishes to express his appreciation to Doctor William B. Whitten for discussions, frequent suggestions, and his valuable advice. The design and development of the high-pressure system would not have been possible without the experience and help provided by Professor William B. Daniels of the University of Delaware. Special thanks are also due to Doctor David E. Cox of Brookhaven National Laboratory for his collaboration on the neutron diffraction work, and to Professor George J. Dienes for his guidance of the elastic constants work.

Appreciation is here expressed for the support of this research by the U.S. Air Force Office of Scientific Research, and by the City University of New York. The author has also benefited by the use of the facilities provided by Brookhaven National Laboratory.

TABLE OF CONTENTS

TABLES

FIGURES

Introduction

The two main goals of this work are to calculate the pressure dependence of the Hall and drift mobilities of charge carriers in naphthalene, using different band models, and to verify these calculations by attempting to measure the variation with pressure of the Hall effect of holes in single crystals of high purity naphthalene. In this chapter, the various theories regarding charge transport in organic semiconductors, band theory, hopping motion, and tunneling models are contrasted. The role of excitons in producing charge carriers in organic crystals is discussed, and the objectives of this investigation are stated.

1. General Characteristics of Organic Semiconductors

At atmospheric pressure, organic crystals such as naphthalene are not really semiconductors, in that they do not exhibit intrinsic conductivity. They are called semiconductors, however, because their dark electrical conductivity increases exponentially with temperature as $\sigma \approx \sigma_o \exp(-E/kT)$ where σ_o is referred to as the pre-exponential factor. For naphthalene, a typical organic semiconductor, $E \approx 1.85$ ev , $\sigma_o \approx 10^{13} (\Omega - \text{cm})^{-1}$, and $\sigma_{15°C} \approx 10^{-19} (\Omega - \text{cm})^{-1}$.[1] And since 2E is smaller than the band gap of 5.2 ev for naphthalene[5], there can be no measurable intrinsic conductivity in the solid state. Any current that flows at room temperature is probably due to carrier injection by some extrinsic means, e.g., by light absorption, contacts, adsorbed gases, or impurities.

Organic semiconductors belong to the class of solids known as molecular crystals. Such crystals are held together by means of van der Waals interactions, and the molecules are relatively far from one another. Naphthalene is a planar polycyclic aromatic hydrocarbon[2]; it has a monoclinic crystal structure with two molecules per unit cell (see fig. 1.1), and its space group is $P2_1/a$.[3]

As is typical for van der Waals crystals, the intermolecular interactions are generally weak, and the molecular energy levels are relatively undisturbed in a molecular crystal. The electronic states of aromatic molecules are assumed to factor into non interacting sets of σ-orbitals

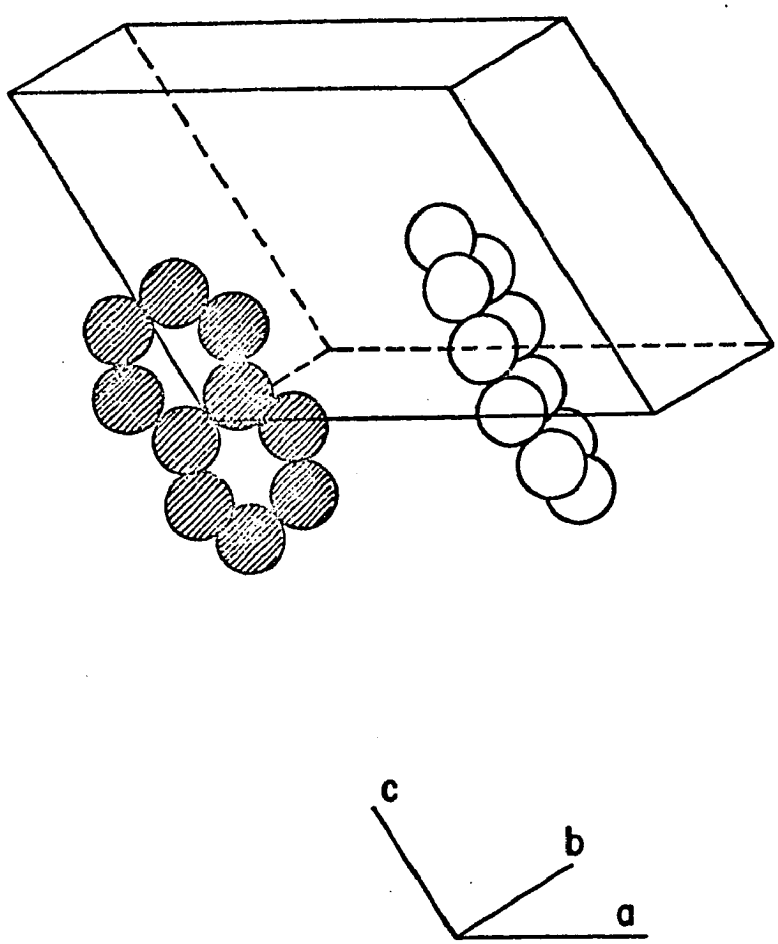

FIG. 1.1

and π-orbitals. The σ-orbitals are symmetrical around the bond axis, giving localized C-C and C-H bonds, while the π-orbitals are perpendicular to the molecular plane. Any π-orbital overlaps both of its neighbors equally so that the π-electrons are completely delocalized. In the ground state of the molecule, these π-electrons occupy all the bonding orbitals.

In order to obtain charge transport, it is necessary, at the very least, to excite an electron from the highest bonding orbital of the naphthalene molecule to the lowest antibonding orbitals of its neighbors. The lowest lying excited states of the naphthalene crystal are the first triplet and singlet states, respectively. These are shown schematically, relative to the singlet ground state, in fig. 1.2 [4]. The band gap is approximately 5.2 ev [5].

2. Models for Charge Transport

The theories that have been used to describe charge transport in molecular crystals are the band theory, the hopping model, and the tunneling model.

Band theory considers charge carriers to be completely shared by the entire crystal lattice. Bloch momentum eigenfunctions of the perfect lattice are used as basis functions, and crystal imperfections, phonon or other, are treated as perturbations that scatter carriers among the perfect lattice states. In this model, the π-orbitals, extending from the molecular planes, overlap with one another so that their energy levels are broadened into bands belonging to the entire crystal.

Calculations of the energy band structure of naphthalene, at atmospheric pressure, have been performed by Thaxton et al[6], Katz et al[7], Silbey et al[8] and Glaeser and Berry[9]. These calculations, along with the differences between the various band structures used, are discussed in more detail in chapter three. The tight binding approximation was used in all the calculations, because of the relatively small interactions between molecules in a molecular crystal, compared to the separations of the states of the isolated molecule (and crystal). Leblanc[10] and Friedman[11] then calculated the Hall and drift mobilities (μ_H and μ_D), at atmospheric pressure, assuming either a constant relaxation time or a constant mean free path.

The bandwidths obtained are narrow, of the order of kT. However, all

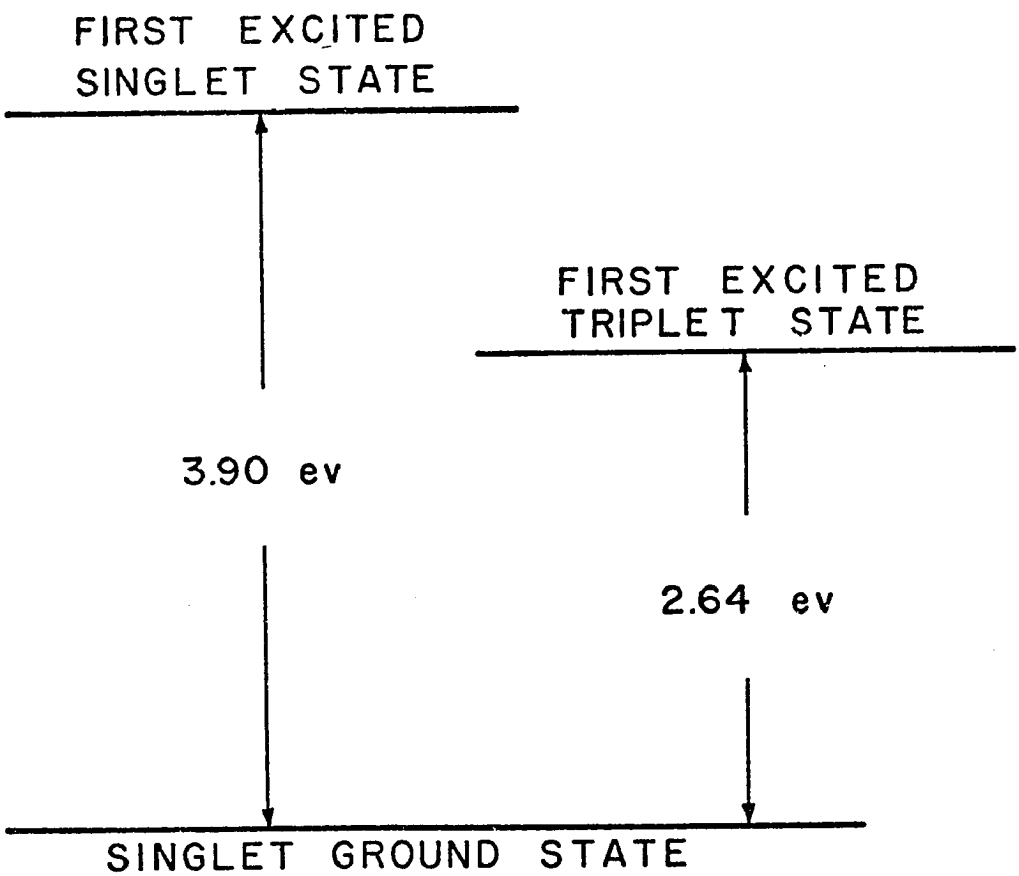

FIG. 1.2

band models correctly predict the experimentally observed decrease in drift mobility with increasing temperature ($\mu_D \sim T^{-n}$ with $n \sim 1\text{-}3$)[12].

As a consequence of the narrow bandwidths, the conventional result $(\mu_H/\mu_D) \approx +1$ is no longer obtained. In fact, the sign, as well as the magnitude, of this ratio can change. This effect occurs if the bands are sufficiently narrow for an electron (or hole) to be thermally excited into the top of the conduction band (bottom of the valence band) where it would be in a negative effective mass state. In the presence of a magnetic field, an electron (or hole) in a negative effective mass state would be deflected in the opposite direction from one in a positive effective mass state. Then, depending upon the statistical contributions of all states, it is possible for the Hall effect to be anomalous for electrons and holes. Measurements of the Hall effect should therefore be a sensitive probe of the details of the band structure used.

The difficulties that arise when a band picture is applied to low-mobility transport have been discussed by Frohlich and Sewell[13] and Glarum[14]. For the band model to be a consistent physical description, the electron-phonon coupling must be weak compared to the intermolecular electronic coupling so that the energy broadening caused by the finite lifetime of the Bloch states is less than the electron bandwidth, i.e. $W > \hbar/\tau$, where W is the bandwidth and τ the relaxation time. This led Glarum to conclude that the band model would be appropriate for drift mobilities $\gg 1$ cm^2/V-sec, and the hopping polaron model for drift mobilities $\ll 1$ cm^2/V-sec. However, the available drift mobility data for naphthalene[12,15,16] show values of the order of 1 cm^2/V-sec, thus being an intermediate case between band and hopping conductions.

The hopping model, developed by Holstein and Friedman[17,18], considers the carriers to interact so strongly with the intermolecular lattice vibrations that the lattice is severely distorted in its neighborhood. The rate of motion of the carrier is then determined by the rate at which the lattice distortion can relax; this involves multiple phonon absorption and reemission. The motion of an electron together with its induced lattice deformation is called polaron motion. Polaron motion results in drift mobilities that increase exponentially with temperature when $T > \frac{1}{2}\theta_{Debye}$. Below this temperature, the motion is described in terms of a polaron band theory, where the drift mobility is a decreasing function of temperature.

Hopping models used in references 17 and 18 do not predict an anomalous Hall effect.

The tunneling model considers the carrier to tunnel through the potential barrier of adjacent molecules[19]. In this model, the temperature dependence of the drift mobility is obtained from a variation of the potential barrier width as the molecules undergo lattice vibrations. However, as pointed out by Tredgold[20], such a model results in drift mobilities that increase exponentially with temperature, contrary to experimental observations.

In recent investigations, Munn and Siebrand[21] suggested a model intermediate between hopping and band-like transport to predict the temperature dependence of the drift mobility[22] and the anomalous Hall effect in anthracene[23]. However, their approach is based on assuming a large number of parameters that are characteristic only of anthracene. Besides, in the case of naphthalene, it will be seen (chapters four and five) that a band model, taking into consideration the intramolecular vibrations, can account for the signs of the Hall mobilities of holes, as well as the magnitude of the pressure dependence.

3. Role of Excitons in Charge Carrier Production

It is well known that photoconductivity in molecular crystals can take place by means of two different mechanisms. The first one is the direct process of carrier generation, in which a molecule in the crystal is ionized, thus resulting in an electron hole pair. In the second mechanism, excitons, which are otherwise energetically incapable of carrier pair production, can produce either a hole or an electron as a result of a dissociation process at an electrode, impurity, or defect site. The different exciton processes have been reviewed by Leblanc[5], Pope and Kallmann[24], Castro[25], and Braun and Dobbs[26].

The various exciton mechanisms, and in particular the ones involving triplet excitons, are now known to be magnetic field sensitive. In a series of investigations, Johnson et al[27], Ern and Merrifield[28], Avakian and Merrifield[29], and Johnson and Merrifield[30] reported a magnetic field effect on the mutual annihilation of triplet excitons in anthracene crystals. Also, magnetic field effects on the change in photoconductivity of anthracene were presented as evidence of a variation in the interaction between tri-

plet excitons and trapped carriers by Geacintov et al[31], Frankevich et al[32] and Bouchriha et al[33]. More recently, similar effects were reported by Bouchriha et al[34] and Pope et al[35], in pyrene and tetracene, respectively.

Such effects, depending upon their magnitude, are therefore expected to affect the Hall mobility measurements of naphthalene. In chapter five, this will be seen to be the case.

4. Thesis Objectives

One of the two goals of this investigation was to calculate the effect of pressure on the band structure of naphthalene. This is carried out in chapter three, using three different band models. These were obtained by taking into consideration various combinations of interactions: resonance integrals, exchange effects, and vibrational overlap.

But first, the linear compressibilities of naphthalene single crystals had to be determined. These were measured in a neutron diffraction experiment at the Brookhaven High Flux Beam Reactor, and are presented in chapter two. In this same chapter, a possible set of elastic constants of naphthalene is also calculated on the basis of the measured linear compressibilities.

Chapter four gives the calculations of the pressure dependence of the Hall and drift mobility tensors of naphthalene. These were carried out in the constant τ and constant λ approximations, using the three band models. Computations done in the constant λ approximation, and using a band model which takes into consideration the resonance and exchange integrals as well as the intramolecular vibrations, are shown to predict the correct anisotropies for the drift mobility tensor of naphthalene.

The second goal was to verify these calculations, by measuring the variation with pressure of the Hall effect of holes in naphthalene. For this purpose, a high-pressure apparatus was developed. This is described in chapter five, along with the experimental techniques used to measure the Hall effect. The measured Hall mobilities are also given in the same chapter. These tend to confirm the results of chapter four that, for conduction in narrow bands, the assumption of a constant mean free path gives a better agreement with the experimental results than the assumption of a constant mean free time.

References - Chapter 1

1. H. Pick and G. Wissman, Z. Physik, 138, 436 (1954).

2. D.W.J. Cruickshank, Acta Cryst., 10, 504 (1957).

3. S.C. Abrahams, J.M. Robertson and J.G. White, Acta Cryst., 2, 238 (1949).

4. F. Gutmann and L.E. Lyons, Organic Semiconductors, p.659, Wiley, Inc., New York, 1967.

5. O.H. Leblanc, Jr., Physics and Chemistry of the Organic Solid State, vol. 3, p.167, (Eds. D. Fox, M.M. Labes and A. Weissberger), Wiley-Interscience, New York, 1967.

6. G.D. Thaxton, R.C. Jarnagin and M. Silver, J. Phys. Chem., 66, 2461 (1962).

7. J.L. Katz, S.A. Rice, S.I. Choi and J. Jortner, J. Chem. Phys., 39, 1683 (1963).

8. R. Silbey, J. Jortner, S.A. Rice and M.T. Vala, Jr., J. Chem. Phys., 42, 733 (1965); 43, 2925 (1965).

9. R.M. Glaeser and R.S. Berry, J. Chem. Phys., 44, 3797 (1966).

10. O.H. Leblanc, Jr., J. Chem. Phys., 39, 2395 (1963).

11. L. Friedman, Phys. Rev., 133, A1668 (1964).

12. W. Mey and A.M. Hermann, Phys. Rev. B, 7, 1652 (1973).

13. H. Frohlich and G.L. Sewell, Proc. Phys. Soc. (London), 74, 643 (1959).

14. S. Glarum, J. Phys. Chem. Solids, 24, 1577 (1963).

15. M. Silver, J. Rho, D. Olness and R.C. Jarnagin, J. Chem. Phys., 38, 3030 (1963).

16. D.H. Spielberg, A.I. Korn and A.C. Damask, Phys. Rev. B, 3, 2012 (1971).

17. T. Holstein, Ann. Phys., 8, 325, 343 (1959).

18. L. Friedman and T. Holstein, Ann. Phys., 21, 494 (1963).

19. R.A. Keller and H.E. Rast, J. Chem. Phys., 36, 2640 (1962).

20. R.H. Tredgold, Proc. Phys. Soc. (London), 80, 807 (1962).

21. R.W. Munn and W. Siebrand, J. Chem. Phys., 52, 6391 (1970); 53, 3343 (1970); Chem. Phys. Letters, 3, 655 (1969); Phys. Rev. B, 2, 3435 (1970).

22. R.G. Kepler, Organic Semiconductors, (Eds. J.J. Brophy and J.W. Buttrey), MacMillan, New York, 1962.

23. A.I. Korn, R.A. Arndt and A.C. Damask, Phys. Rev., 186, 938 (1969).

24. M. Pope and H. Kallmann, Disc. Faraday Soc., 51, 7 (1971).

25. G. Castro, IBM J. Res. & Develop. (USA), 15, 27 (1971).

26. C.L. Braun and G.M. Dobbs, J. Chem. Phys., 53, 2718 (1970).

27. R.C. Johnson, R.E. Merrifield, P. Avakian and R.B. Flippen, Phys. Rev. Letters, 19, 285 (1967).

28. V. Ern and R.E. Merrifield, Phys. Rev. Letters, 21, 609 (1968).

29. P. Avakian and R.E. Merrifield, Molec. Cryst., 5, 37 (1968).

30. R.C. Johnson and R.E. Merrifield, Phys. Rev. B, 1, 896 (1970).

31. N.E. Geacintov, M. Pope and S. Fox, J. Phys. Chem. Solids, 31, 1375 (1970).

32. E.L. Frankevich and I.A. Sokolik, Solid State Commun., 8, 251 (1970).

33. H. Bouchriha, G. Delacote, P. Delannoy and M. Schott, J. Phys. (Paris), 35, 577 (1974).

34. H. Bouchriha, M. Schott and J.L. Fave, J. Phys. (Paris), 36, 399 (1975).

35. M. Pope and Y. Solowiejczyk, Molec. Cryst. Liq. Cryst., 30, 175 (1975).

Chapter Two

Hydrostatic Pressure Effect on the Lattice Parameters of Naphthalene

1. Introduction

Two types of interactions hold molecular crystals of aromatic molecules together. First, the molecules in the crystal show weak van der Waals interactions. The cohesion energy $W(R_{ij})$ due to two atoms i and j located on different molecules is given by:

$$W(R_{ij}) = B \exp(-CR_{ij}) - A/R_{ij}^{6} \qquad (2.1)$$

R_{ij} being the distance between the two atoms; the coefficients A, B and C are given by Kitaigorodski[1].

Second, the different atoms in a molecule are strongly coupled via covalent interactions. The covalent bond is formed by electrons, one from each atom participating in the bond; these electrons are then shared by all the atoms forming the bond.

Because of the weak van der Waals intermolecular interactions, these crystals may be expected to be quite compressible, even at relatively low pressures. The first quantitative investigations of the volume compressibilities of organic compounds were carried out by Bridgman[2,3]. He used dilatometric techniques to measure the volume compressibilities, up to 40 kilobars, of a number of such compounds, including naphthalene. Then Kabalinka[4], using a special X-ray camera, observed compressibility anisotropies, up to 12 kilobars, along the crystallographic directions of the polyphenyls. More recently, Vaidya and Kennedy[5] used differential piston displacements methods to measure the volume compressibilities, up to 45 kilobars, of 18 organic solids, including naphthalene.

Since however the dispersion forces between conjugated π-electrons systems are anisotropic, and since a detailed knowledge of the shape of the unit cell as well as the structure of the molecules that form its basis is a prerequisite for a band structure calculation at the various pressures, data on the linear compressibilities of naphthalene are required.

For the range of pressures used in this work, there are no pressure induced intramolecular changes since these do not start to occur before 10^5 atm. Therefore, only the variation with pressure of the lattice parameters of naphthalene was determined; this was done in a neutron diffraction experiment using single crystals. The apparatus, techniques and procedures used will be described in this chapter. But first, a linear theory of elasticity is presented to indicate the relationship between the linear compressibilities of a monoclinic crystal and its elastic stiffness constants.

2. Linear Theory of Elasticity

2a. Hooke's Law

The approach given here is basically that of Nye[6]. We shall consider the elastic properties of a crystal viewed as a homogeneous continuum medium, rather than as a periodic array of atoms. If the stress applied to a solid body is below a certain limiting value, the elastic limit, the strain is recoverable. Furthermore, below that limit, stress σ and strain ϵ are linearly related by Hooke's law

$$\epsilon = S\,\sigma \tag{2.2}$$

where S is the elastic compliance constant or the compliance.

Now a homogeneous stress and a homogeneous strain are each specified, in general, by second-rank tensors symbolically written as σ_{kl} and ϵ_{ij} respectively. The generalized form of Hooke's law may therefore be written as:

$$\epsilon_{ij} = S_{ijkl}\,\sigma_{kl} \qquad (i,j,k,l = 1,2 \text{ or } 3) \tag{2.3}$$

the 81 S_{ijkl} being the compliances of the crystal.

As an alternative to eq. (2.3), the stresses may be expressed in terms of the strains by the equation:

$$\sigma_{ij} = C_{ijkl}\,\epsilon_{kl} \tag{2.4}$$

where the C_{ijkl} are the 81 stiffness constants of the crystal.

The 81 compliances S_{ijkl} form a fourth-rank tensor. Similarly, the 81 stiffness constants C_{ijkl} form another fourth-rank tensor. But since:

$$\epsilon_{ij} = \epsilon_{ji} \tag{2.5}$$

and $$\sigma_{ij} = \sigma_{ji} \tag{2.6}$$

we see that $$S_{ijkl} = S_{ijlk} = S_{jikl} \tag{2.7}$$

and $$C_{ijkl} = C_{ijlk} = C_{jikl} \tag{2.8}$$

Equations (2.7) and (2.8) reduce the number of independent S_{ijkl} and C_{ijkl} from 81 to 36.

2b. The Matrix Notation

Due to the symmetry of S_{ijkl} and C_{ijkl} in the first two and the last two suffixes, it is possible to use a matrix notation in which the stress and strain components are written with a single suffix running from 1 to 6

$$\begin{bmatrix} \sigma_{11} & \sigma_{12} & \sigma_{31} \\ \sigma_{12} & \sigma_{22} & \sigma_{23} \\ \sigma_{31} & \sigma_{23} & \sigma_{33} \end{bmatrix} \rightarrow \begin{bmatrix} \sigma_1 & \sigma_6 & \sigma_5 \\ \sigma_6 & \sigma_2 & \sigma_4 \\ \sigma_5 & \sigma_4 & \sigma_3 \end{bmatrix} \qquad \begin{bmatrix} \epsilon_{11} & \epsilon_{12} & \epsilon_{31} \\ \epsilon_{12} & \epsilon_{22} & \epsilon_{23} \\ \epsilon_{31} & \epsilon_{23} & \epsilon_{33} \end{bmatrix} \rightarrow \begin{bmatrix} \epsilon_1 & \frac{1}{2}\epsilon_6 & \frac{1}{2}\epsilon_5 \\ \frac{1}{2}\epsilon_6 & \epsilon_2 & \frac{1}{2}\epsilon_4 \\ \frac{1}{2}\epsilon_5 & \frac{1}{2}\epsilon_4 & \epsilon_3 \end{bmatrix} \tag{2.9}$$

In the S_{ijkl} and the C_{ijkl} the first two suffixes are abbreviated into a single one running from 1 to 6, and the last two are abbreviated in the same way, according to the scheme,

tensor notation	11	22	33	23,32	31,13	12,21
matrix notation	1	2	3	4	5	6

At the same time factors of 2 and 4 are introduced as follows:

$S_{ijkl} = S_{mn}$ when m and n are 1,2 or 3,

$2S_{ijkl} = S_{mn}$ when either m or n are 4,5 or 6,

$4S_{ijkl} = S_{mn}$ when both m and n are 4,5 or 6.

In general, therefore, eq.(2.3) takes the shorter form:

$$\epsilon_i = S_{ij}\,\sigma_j \qquad (i,j = 1,2,\ldots,6) \tag{2.10}$$

For the C_{ijkl} no factors of 2 or 4 are necessary. For if we write simply: $C_{ijkl} = C_{mn}$ $(i,j,k,l = 1,2,3;\ m,n = 1,\ldots,6)$

then eq.(2.4) takes the form:

$$\sigma_i = C_{ij}\, \epsilon_j \qquad (i,j = 1,2,\ldots,6) \tag{2.11}$$

By substituting from eq.(2.10) into eq.(2.11)

$$\sigma_i = C_{ij}\, S_{jk}\, \sigma_k$$

which gives:

$$C_{ij}\, S_{jk} = \delta_{ik}$$

i.e.

$$S = C^{-1} \tag{2.12}$$

The arrays of S_{ij} and C_{ij} can be thus written out in squares:

$$\begin{pmatrix} S_{11} & S_{12} & S_{13} & S_{14} & S_{15} & S_{16} \\ S_{21} & S_{22} & S_{23} & S_{24} & S_{25} & S_{26} \\ S_{31} & S_{32} & S_{33} & S_{34} & S_{35} & S_{36} \\ S_{41} & S_{42} & S_{43} & S_{44} & S_{45} & S_{46} \\ S_{51} & S_{52} & S_{53} & S_{54} & S_{55} & S_{56} \\ S_{61} & S_{62} & S_{63} & S_{64} & S_{65} & S_{66} \end{pmatrix} \quad \text{and} \quad \begin{pmatrix} C_{11} & C_{12} & C_{13} & C_{14} & C_{15} & C_{16} \\ C_{21} & C_{22} & C_{23} & C_{24} & C_{25} & C_{26} \\ C_{31} & C_{32} & C_{33} & C_{34} & C_{35} & C_{36} \\ C_{41} & C_{42} & C_{43} & C_{44} & C_{45} & C_{46} \\ C_{51} & C_{52} & C_{53} & C_{54} & C_{55} & C_{56} \\ C_{61} & C_{62} & C_{63} & C_{64} & C_{65} & C_{66} \end{pmatrix} \tag{2.13}$$

which are the matrices (S_{ij}) and (C_{ij}).

Finally, from general symmetry considerations, it can be shown that these matrices are symmetrical about the leading diagonal

$$C_{ij} = C_{ji} \qquad S_{ij} = S_{ji} \tag{2.14}$$

thus reducing the number of independent components from 36 to 21.

Also, from additional symmetry considerations pertinent to a monoclinic crystal the number of independent components is further reduced from 21 to 13 , as shown in the following diagram

$$\begin{pmatrix} o & o & o & . & o & . \\ & o & o & . & o & . \\ & & o & . & o & . \\ & & & o & . & o \\ & & & & o & . \\ & & & & & o \end{pmatrix}$$

where the following notation is used: . represents a component equal to zero and o a non-zero component.

2c. Variation of the Lattice Parameters Under Hydrostatic Pressure

In case of applied hydrostatic pressure on the crystal, there are no shear stresses

$$\sigma_{kl} = - P \delta_{kl} \tag{2.15}$$

We now calculate the proportional decrease in volume of a crystal when subjected to unit hydrostatic pressure, that is, its volume compressibility. Substituting eq.(2.15) into eq.(2.3) gives:

$$\epsilon_{ij} = - P S_{ijkl} \delta_{kl} = - P S_{ijkk} \tag{2.16}$$

For the dilation Δ , we have:

$$\Delta = \epsilon_{ii} = - P S_{iikk} \tag{2.17}$$

And so the volume compressibility is:

$$- \frac{\Delta V}{V} = - \Delta / P = S_{iikk} \tag{2.18}$$

In matrix notation the volume compressibility is:

$$- \frac{\Delta V}{V} = S_{11} + S_{22} + S_{33} + 2(S_{12} + S_{23} + S_{31}) \tag{2.19}$$

The linear compressibility of a crystal is defined as the relative decrease in length of a line when the crystal is subjected to unit hydrostatic pressure. For a monoclinic crystal, it varies with direction. Under pressure P the stretch of a line in the direction of the unit vector ℓ_i is:

$$\epsilon_{ij} \ell_i \ell_j = - P S_{ijkk} \ell_i \ell_j \tag{2.20}$$

from eq.(2.16) . And so the linear compressibility is:

$$\eta = S_{ijkk} \ell_i \ell_j \tag{2.21}$$

Written out in matrix notation, the expression for η is:

$$\eta = (S_{11} + S_{12} + S_{13})\ell_1^2 + (S_{12} + S_{22} + S_{23})\ell_2^2 + (S_{13} + S_{23} + S_{33})\ell_3^2 + (S_{15} + S_{25} + S_{35})\ell_3\ell_1 \tag{2.22}$$

For the linear compressibility α in the a direction, we have:

$$\ell_1 = 1 \quad , \quad \ell_2 = \ell_3 = 0$$

therefore $$\alpha = (S_{11} + S_{12} + S_{13}) \tag{2.23}$$

Similarly for the linear compressibility $\varkappa$ in the b direction we get:

$$\ell_1 = \ell_3 = 0 \quad , \quad \ell_2 = 1$$

therefore $$\varkappa = (S_{12} + S_{22} + S_{23}) \tag{2.24}$$

Also, for the linear compressibility γ in the c direction we have:

$$\ell_1 = \cos\beta_o \quad , \quad \ell_2 = 0 \quad , \quad \ell_3 = \sin\beta_o$$

thus $$\gamma = (S_{11} + S_{12} + S_{13})\cos^2\beta_o + (S_{13} + S_{23} + S_{33})\sin^2\beta_o + (S_{15} + S_{25} + S_{35})\sin\beta_o\cos\beta_o \tag{2.25}$$

Finally, to calculate the variation in the angle β , we write:

$$\sin\beta = \sin(\beta_o + \beta) = \frac{|\vec{a} \times \vec{c}|}{|\vec{a}||\vec{c}|} \tag{2.26}$$

After some manipulations, we obtain in first order:

$$\Delta\beta = P\left[(S_{15} + S_{25} + S_{35})\sin^2\beta_o + (S_{11} + S_{12} + S_{13})\sin\beta_o\cos\beta_o - (S_{13} + S_{23} + S_{33})\sin\beta_o\cos\beta_o\right] \tag{2.27}$$

Therefore, the compressibility δ in the angle β can be written as:

$$\delta = \frac{\Delta\beta}{P\beta_o} = \frac{1}{\beta_o}\left[(S_{15} + S_{25} + S_{35})\sin^2\beta_o + (S_{11} + S_{12} + S_{13})\sin\beta_o\cos\beta_o - (S_{13} + S_{23} + S_{33})\sin\beta_o\cos\beta_o\right] \tag{2.28}$$

Table 2.1 summarizes the results of this section.

Having presented the relevant aspects of the linear theory of elasticity, we are ready to describe the experiment. However, before doing that, we give an outline of the crystal growing and preparation techniques that were used in this work.

3. The Purification and Growth of Large Naphthalene Crystals

3a. Purification of Naphthalene

Single crystals of high purity were required for a precise determi-

Table 2.1 - Linear compressibilities of a monoclinic crystal in terms of the elements of the compliance matrix S.

Lattice parameter	Linear compressibility
a	$S_{11} + S_{12} + S_{13}$
b	$S_{12} + S_{22} + S_{23}$
c	$(S_{11} + S_{12} + S_{13})\cos^2\beta_o + (S_{13} + S_{23} + S_{33})\sin^2\beta_o + (S_{15} + S_{25} + S_{35})\sin\beta_o\cos\beta_o$
β	$\frac{1}{\beta_o}\left[(S_{15} + S_{25} + S_{35})\sin^2\beta_o + (S_{11} + S_{12} + S_{13})\sin\beta_o\cos\beta_o - (S_{13} + S_{23} + S_{33})\sin\beta_o\cos\beta_o\right]$

nation of the parameters of the unit cell at the various pressures, as well as for measurements of the electrical transport properties in naphthalene, because impurities generate trapping states that alter these properties[7,8,9]. Various methods are available for purification which include chromatography, multiple vacuum sublimation, vacuum sublimation with sulphuric acid treatment[10], normal freezing[11], fusion over potassium[12] and zone refining[13,14]. In general, it has not been proved that any one of the above methods (excluding zone refining) possess advantages over others. Thus one must carry out the purification by a combination of more than one of these methods.

Purification of naphthalene extracted from coal tar distillates (Eastman 168) was done by repeated vacuum sublimation and zone refining. All purification processes were performed under yellow "safe" lights to prevent photo-chemical reactions from generating impurities.

The major impurities in coal tar naphthalene are fluorene, biphenyl, β-methylnaphthalene and indane[15].

(i) Vacuum Sublimation

The coal tar naphthalene was first purified by vacuum sublimation. The apparatus used for this purpose was a combined sublimation apparatus and zone refining tube, shown in fig. 2.1 .

100 to 120 grams of the material were loaded into the left-hand bulb, the filling tube sealed and the apparatus pumped down to a pressure that was less than 50 microns. The left-hand bulb was placed in a furnace maintained at a temperature of 65 °C , while the other bulb was wrapped with wet towels to insure that the naphthalene, subliming under continuous evacuation, would deposit into it. The most volatile impurities were pumped off and trapped. When approximately 90% to 95% of the naphthalene had passed over to the second bulb, the furnace was turned off and the remaining, impure, naphthalene sealed in the first bulb by melting the constriction. The apparatus was flushed three times and filled to 3/4 atm. with pure nitrogen (research grade). The naphthalene was then melted into the zone refining tube and allowed to solidify.

(ii) Zone Refining

Next, zone refining was carried out in a Fisher zone refiner. A schematic representation of the zone refining process is depicted in fig. 2.2 .

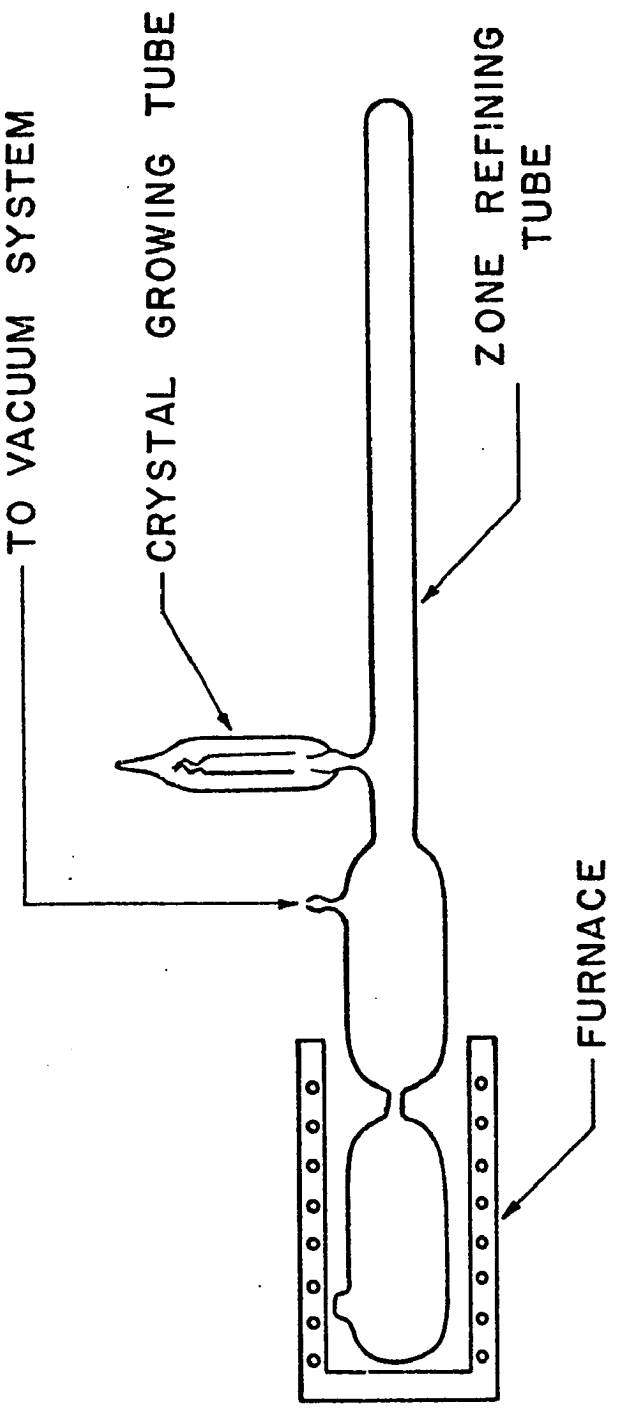

FIG. 2.1

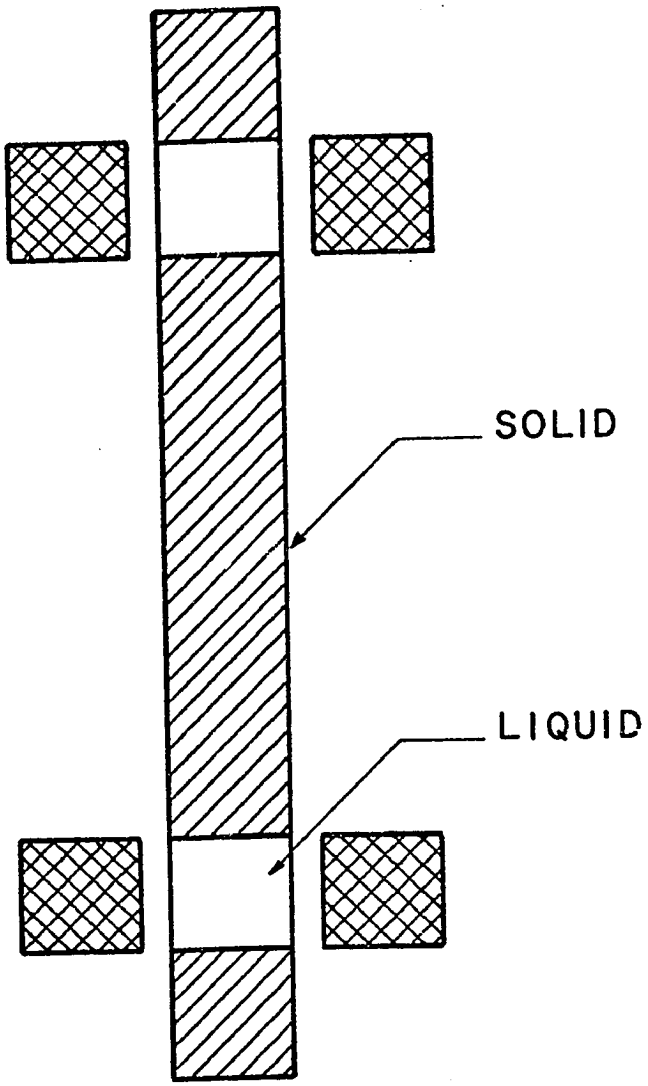

FIG. 2.2

The refining was carried out in thick walled pyrex tubing (2-3 mm wall), to reduce the possibility of breakage which could occur as a result of the considerable expansion on melting which is characteristic of organic compounds. Tube fracture was also avoided by the use of air coolers above the heaters to stabilize the width of the molten zone, and by starting zone melting at the free surface. The presence of an inert gas in the tube prevented serious sublimation of naphthalene up the tube.

About 30 zones of $\frac{1}{2}$ to 1 inch in length were passed down an 18 inch column, at the rate of one inch per hour. The heaters were maintained at the lowest temperature that would permit the formation of a good zone, so that thermal decomposition could be minimized.

Impurities which lower the freezing point of the host substance, naphthalene, traveled with the molten zone, and tended to segregate at the bottom end of the naphthalene column; these impurities have a segregation coefficient that is less than one (the segregation coefficient is defined as the ratio of the impurity mole fraction in the solid to the impurity mole fraction in the liquid)[16]. Impurities which raise the freezing point traveled in a direction opposite to the molten zone and therefore tended to segregate at the top of the naphthalene column; these impurities have a segregation coefficient that is greater than one. Thus, as the molten zone repeatedly sweeps along a bar of impure material, the impurities concentrate at either end, leaving pure material in between.

When zone refining was completed, the tube was cracked open and the upper and lower ends were rejected. The center portion of the naphthalene column was then combined with other similar material and loaded into combined sublimation, zone refining and crystal growing tubes. The material was sublimed as before, and melted into the combined zone refining and crystal growing tubes. The material was then zone refined. After zone refining, the top end of the column was melted into the empty sublimation bulb. The center portion of the column was then melted into the crystal growing tube which was then sealed off from the zone refining tube. In this way, the transfer was effected without exposing the naphthalene to atmospheric oxidation and the crystal was grown in the same atmosphere as used for the final zone refining.

3b. Growth of Naphthalene Crystals

Crystals were grown by the Bridgman method; this is based on achie-

ving a suitable temperature gradient along with a reliable method of initiating a single crystal nucleus and of propagating it through a large volume of material. The best form of temperature gradient is shown schematically in fig. 2.3 next to the furnace used in growing the naphthalene crystals. The upper furnace was kept at a temperature of 86 °C while the lower one was kept at 70 °C (the melting point of naphthalene is 80 °C). The difficulties in growing large naphthalene crystals are mainly due to its great supercooling tendencies and low thermal conductivity. Almost all the heat of fusion of the growing crystal must be removed through the solid, which means that naphthalene due to poor thermal conductivity will take much time to solidify. Hence, the lowering rate of the crystal growing tube was very slow, of the order of 1 mm/hr .

A diagram of the crystal growing tube is shown in fig 2.4 . The tube was suspended in the furnace, as shown in fig. 2.3 , so that the tip was just below the melting point isothermal, and the lowering mechanism was then turned on; crystallization was thus begun by cooling the tip of the tube. This prevented supercooling and the subsequent formation of crystallites.

As the tube is lowered, crystallites grow until, just below the bent capillary, several large crystallites occupy the tube. The bent capillary inevitably selects a particular seed which grows into the upper tube as a large crystal. If the angle between the capillary and the tube axis is less than 45°, the ab cleavage plane will grow parallel to the tube axis. If the angle is greater than 45°, it will grow perpendicular to the tube axis[17].

When growth was complete, the crystal and tube were annealed by cooling the lower furnace to room temperature over a period of three days. The crystal tube was then opened and the crystal boule was easily slid from the inner tube which had already been treated with a release agent; this consisted of a solution of 1% "Dow Corning 200" silicone, dissolved in methyl ethyl ketone. After treatment, and before filling, the crystal tube had been baked for one hour at 250 °C. The release agent reacted chemically with the glass surface, and when a crystal was grown, contamination of the crystal, due to the release agent, was unlikely.

3c. Cutting, Orienting and Shaping a Sample from a Crystal Boule

From the crystal boule, good single crystal areas were chosen. These

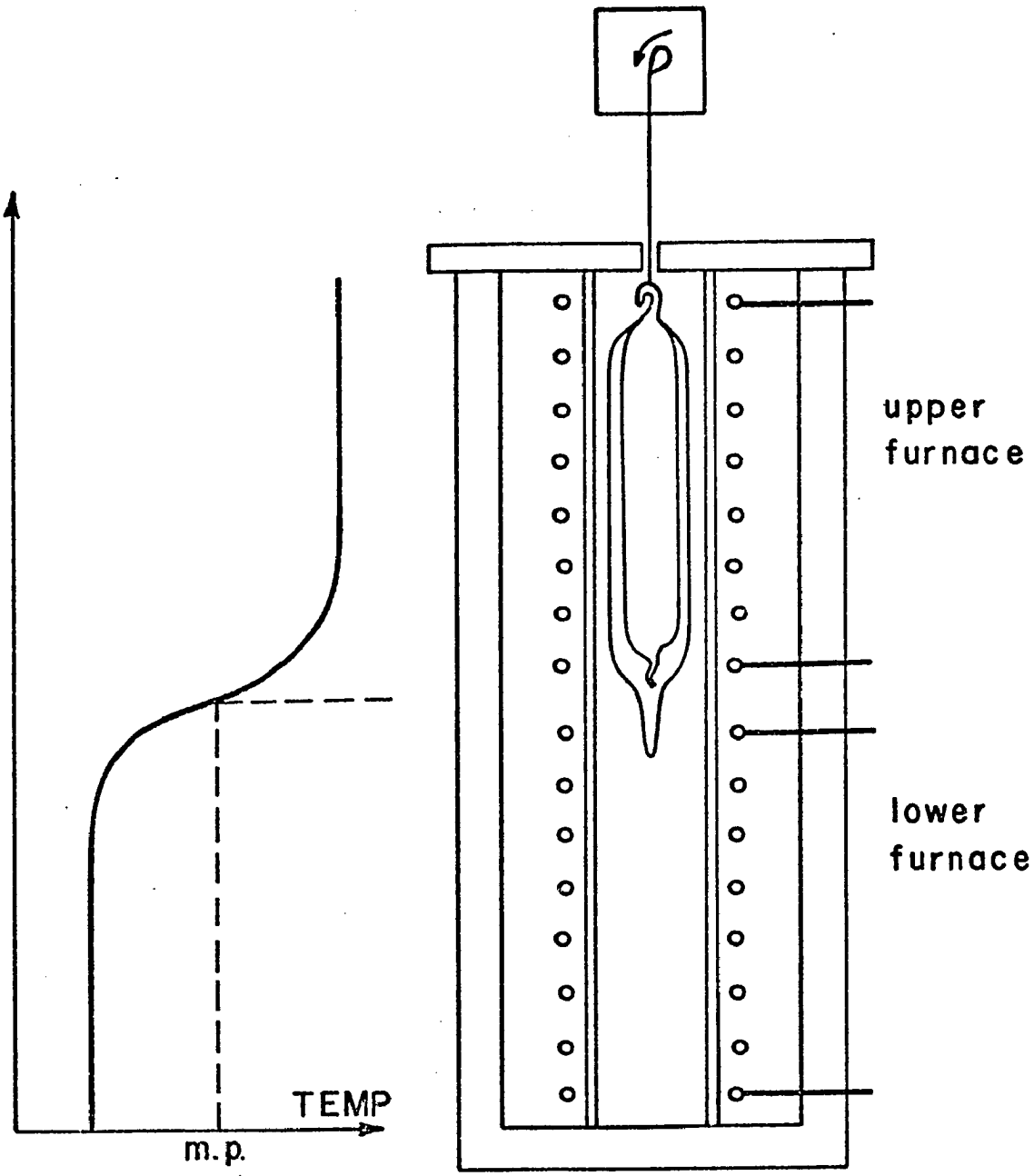

FIG. 2.3

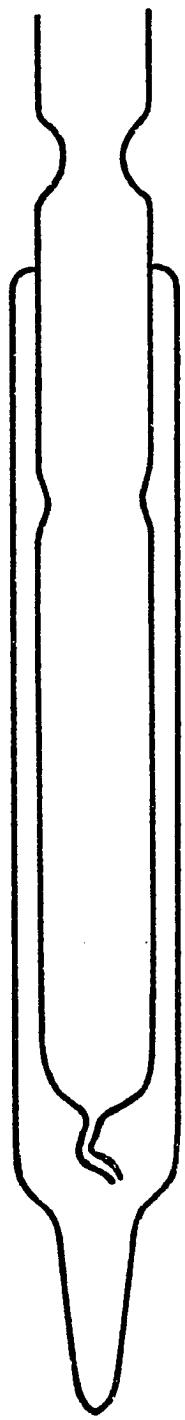

FIG. 2.4

were oriented by recognizing the ab crystal cleavage planes, then locating the a or b directions by using a polarizing microscope[18] along with the double refraction properties of the crystal[19]. With this information, the crystal could be cut in any desired orientation of the a , b or c' directions.

After orientation, the crystals were cut with a string saw, using xylene as a solvent. An optical finish was then obtained by polishing the crystal on a glass slide covered with a soft tissue, soaked in ethyl alcohol. Typical dimensions of a crystal used in the neutron diffraction experiment were 6 mm x 3 mm x 2 mm .

4. Description of the Experiment

4a. The Neutron Beam

The experiment was performed at the Brookhaven High Flux Beam Reactor. Neutrons, resulting from nuclear reactions, were slowed down by making many collisions with a moderator of heavy water and thus tended to come into thermal equilibrium at the reactor temperature. A collimator inserted into the face of the reactor allowed a beam of these neutrons to be extracted. The nature of the wavelength distribution in such a collimated beam is shown in fig. 2.5 [20]. A monochromatic beam of wavelength about 2.4645 Å was reflected from the (002) planes of a pyrolytic graphite monochromator[21,22]. The half wavelength component was essentially removed with a highly oriented pyrolytic graphite filter; the transmission ratio of the 2.4645 Å neutrons was about 3/4 , while the transmission ratio of the $\lambda/2$ component was approximately 1/1500 . The resulting neutron flux was about $10^6 - 10^7$ neut/cm^2/sec . This beam, which was subsequently defined by cadmium slits, was then available for diffraction by a specimen placed in the high-pressure cell; the latter was bolted on the rotating table, at the axis of the spectrometer (see fig. 2.6). The rotational arrangement allowed for three degrees of freedom. The diffracted neutrons were then received in a proportional counter (filled with BF_3 enriched in the boron isotope of mass 10) which could be rotated about the center of the spectrometer.

4b. The High-Pressure Apparatus

The experimental setup, shown in fig. 2.7, used helium as a pressure transmitting fluid. The gas was pumped up to an intermediate pressure of

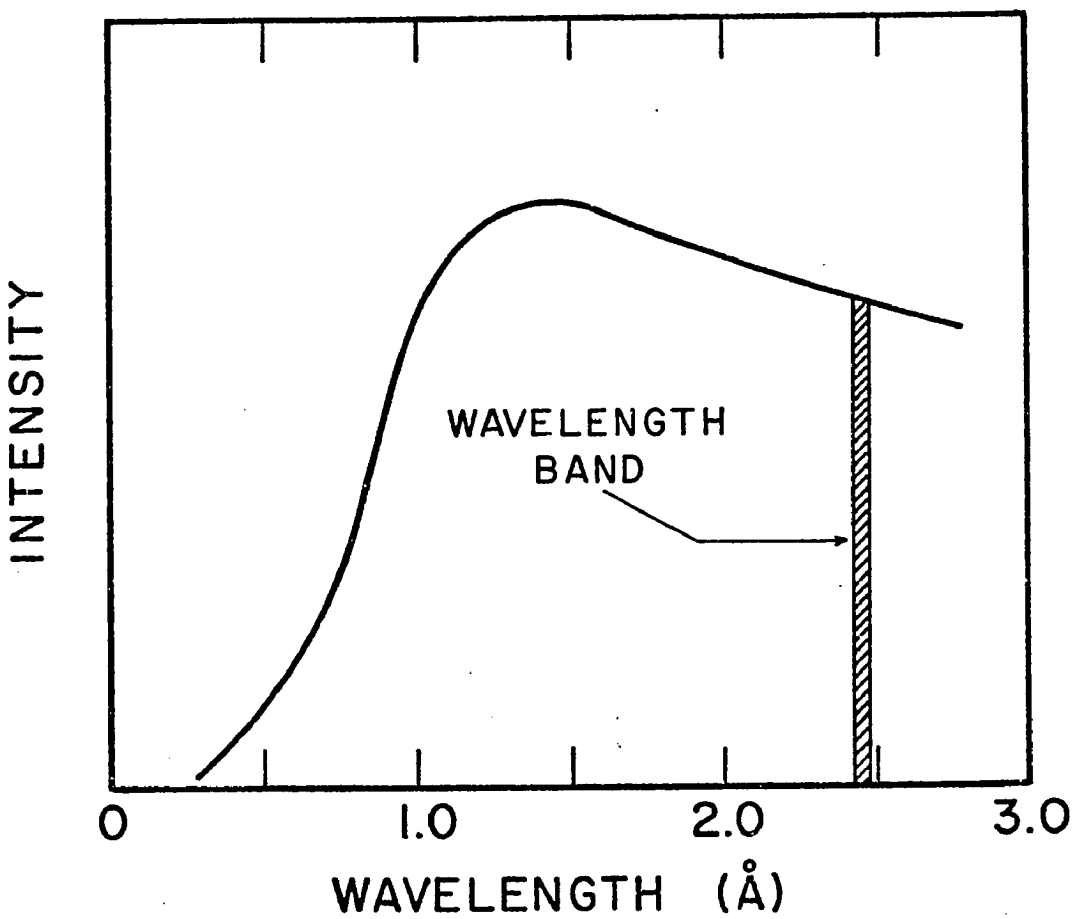

FIG. 2.5

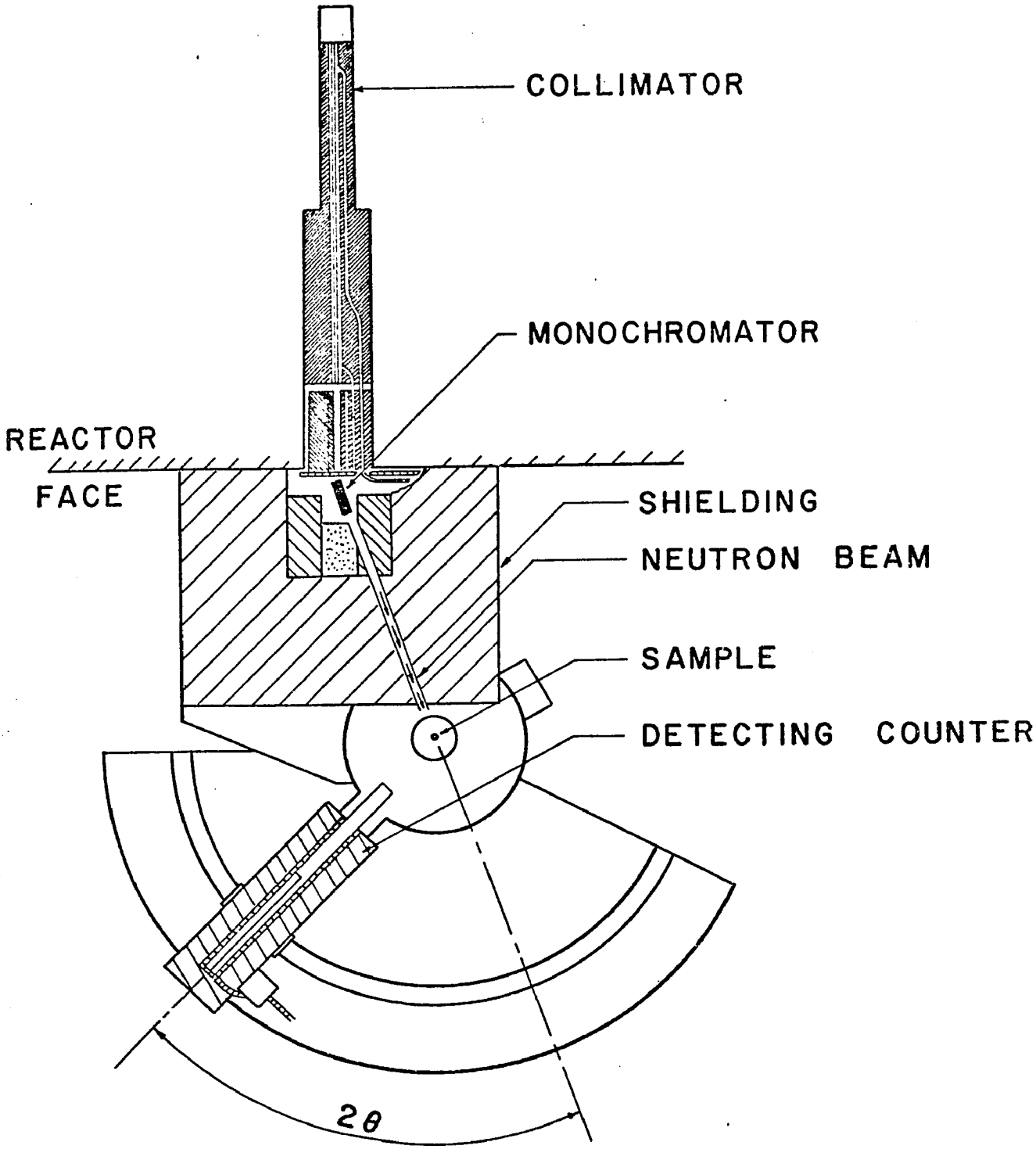

FIG. 2.6

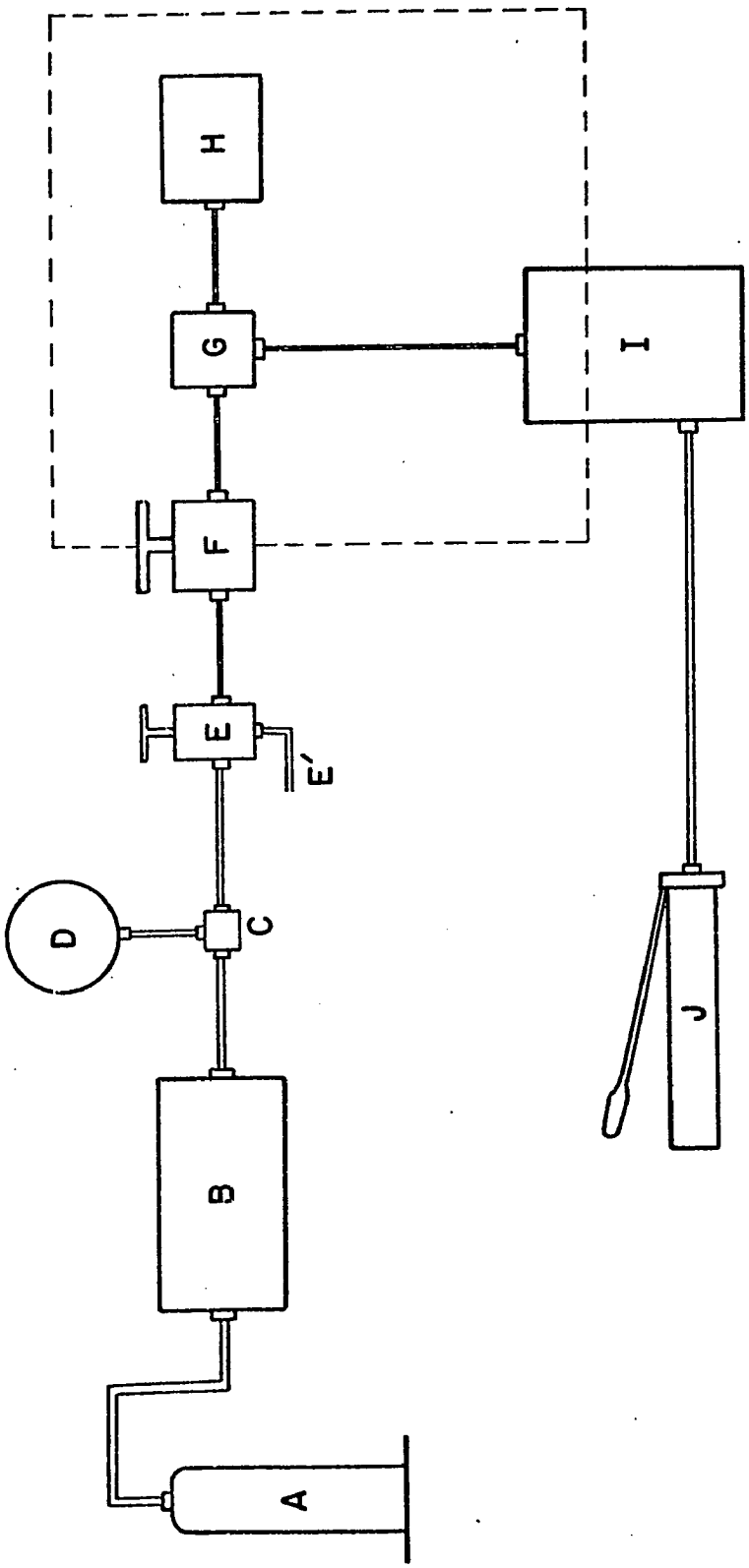

FIG. 2.7

about 30,000 psi by means of a two stage air-operated compressor B (American Instruments Co. # 46-14021). The pressure at this relatively low pressure side was monitored by a spring gauge D (range 50,000 psi); it could also be released through a three-way valve E (HIP # 60-13HF2) whenever compressor B was not being used, in order to protect the latter's diaphragms.

The high-pressure side, enclosed in dotted lines, was then isolated from the intermediate-pressure side by means of valve F (HIP # 150-11XF6). Pressure on this high-pressure side could then be brought up to the desired value by means of an intensifier I (Harwood Engineering Co., Inc., # A 2.5 J ; for gas service up to 200,000 psi; intensification ratio 15:1). The intensifier was driven by a hand pump J (Enerpac oil hand pump). The pressure was measured through the change of resistance of a thin manganin wire enclosed in gauge G (details about the dimensions and construction of the manganin coil are reported in chapter five). The gauge was connected to the sample containing cell. The latter was made out of aluminum, which has a large transmission factor for neutrons (about 94% for wall thicknesses of 1/4 inch)[20].

5. Techniques and Results

To determine which crystal reflections were to be used in performing the measurements, naphthalene data (lattice parameters, fractional coordinates of all atoms and atomic scattering factors for carbon and hydrogen) were fed into a computer program giving the positions and relative intensities of the first 120 peaks of a monoclinic crystal.

Reflections from the (001), (002), (200) and (020) crystal planes were then chosen because of their reasonably large intensities, in addition to giving each lattice parameter as independently of the others as possible (only the (020) reflections give b directly from the measured Bragg angles).

Separate measurements were then carried out on two naphthalene single crystals, with long dimensions along the a and b crystallographic axes respectively. Each crystal was oriented such that its longest axis was perpendicular to the incident neutron beam. The alignment of the first crystal was carried out by noting the relative positions of the a and b axes, then rotating the counter to the expected position of the (020) peak

and keeping it there. The rotating table was then slightly pivoted (3rd-axis rotation), until a maximum count could be recorded. It was fixed in this position and the cell was rocked through the two remaining degrees of freedom of the goniometer, until the highest count was observed. The rotating table was then loosened and the whole process repeated, until the best possible alignment was obtained.

To insure that it was indeed the (020) peak that was being observed, a check on the positions of the (001) and (002) reflections was performed; for this purpose, the table had first to be rotated counterclockwise through an angle of 90°.

Measurements of the Bragg angles for the (020) and (002) peaks were recorded for this crystal, in the pressure range 0 to 5.5 kilobars. These gave the variation with pressure of b and csinβ.

In order to decouple c and β as well as measure the variation of the lattice parameter a with pressure, the second crystal (b axis longest) was used. It was aligned following the procedure outlined before. Determination of the positions of the (200) and (001) peaks were then performed in the pressure range 0 to 5.5 kilobars. These measurements gave the pressure variations of asinβ, csinβ and β. The angle (π - β) is the difference of two angles obtained from 1st-and 3rd-axes measurements at the position of each peak.

The data obtained from both crystals are shown in figs. 2.8 , 2.9 , 2.10 and 2.11 ; these give the variation with pressure of the lattice parameters a, b, c and β , respectively. The error bars were determined from the limit of accuracy of 0.02° in measuring the Bragg angles. The straight lines were obtained from a least squares fitting computer program. The equations of the best lines are[a]:

$$a = 8.251 \ (1 - 0.056P) \qquad (2.29a)$$

$$b = 5.975 \ (1 - 0.032P) \qquad (2.29b)$$

$$c = 8.670 \ (1 - 0.026P) \qquad (2.29c)$$

$$\beta = 122.77 \ (1 + 0.014P) \qquad (2.29d)$$

where P is in 10^{10} dynes/cm^2 ($\sim$ 10 kilobars).

Figure 2.12 shows the volume compressibility ($\Delta V/V_o$) as a function of pressure; for a monoclinic crystal, this can be written as:

[a] a,b,c are in angstroms, and β is in degrees.
While it is conceivable that parabolas would seem to represent a better

$$\Delta V/V_o = \Delta a/a_o + \Delta b/b_o + \Delta c/c_o + \cot\beta_o \Delta\beta \qquad (2.30)$$

All terms on the right-hand side of eq.(2.30) were calculated from the experimental points; a_o , b_o , c_o and β_o are the lattice parameters at atmospheric pressure.

Figure 2.13 shows almost equal compressibilities in the b and c directions, while the compressibility in the a direction is about twice that of b or c. These results are summarized in table 2.2 , which also gives the standard deviations of the compressibilities.

The compressibilities in the a and b directions are found to be in good agreement with the ones obtained from the general linear compressibility curves for monoclinic crystals suggested by Rice and Jortner[23] (see table 2.3). On the other hand, the compressibility in the c direction is larger, by about 30% , than the value 0.020 given by Rice et al. However, since the linear polyphenyls, upon which they based their model, differ in their linear compressibilities in the c direction, therefore it can be concluded that the available data justify speaking of general linear compressibilities for a monoclinic crystal in the a and b directions, but not in the c direction.

In table 2.4 , the volume compressibility at 5 kilobars obtained from the neutron data is compared with the values found by other investigators. It can be seen that the various data agree reasonably well.

Finally, figs. 2.14 and 2.15 show the integrated intensities of the two peaks (002) and (020), at atmospheric pressure and at 5.5 kilobars.

6. Fitting the Compressibility Data to a Set of Elastic Constants

In addition to the experimental determination of the linear compressibilities, a priori calculations can be carried out to evaluate them. The method, as outlined in section 2 of this chapter, involves using the elastic constants matrix C, getting its inverse S (the compliance matrix) and then deducing the strains corresponding to unit hydrostatic pressure.

A few sets of elastic constants for naphthalene are available[24-27]. These were obtained from ultrasonic velocity measurements by the method of Aleksandrov[28]. Another set of elastic constants is also given by Pawley[29]; however, this set is only an improvement over Aleksandrov's[28] through a

fit to the data, it was found that the uncertainties of the measurements (i.e. the error bars) make it unwise at this stage to use anything but straight lines.

Table 2.2 - Linear compressibilities of naphthalene and their standard deviations.

Symbol	Value	Standard deviation
α	0.0560	0.0035
$\varkappa$	0.0320	0.0020
γ	0.0262	0.0035
δ	0.0144	0.0010

Table 2.3 - Comparison between the linear compressibilities for a model monoclinic crystal and the neutron diffraction data.

Compressibility	Sources	
	Rice et al[23]	This work
$\Delta a/a_o$	0.054	0.056
$\Delta b/b_o$	0.030	0.032
$\Delta c/c_o$	0.020	0.026

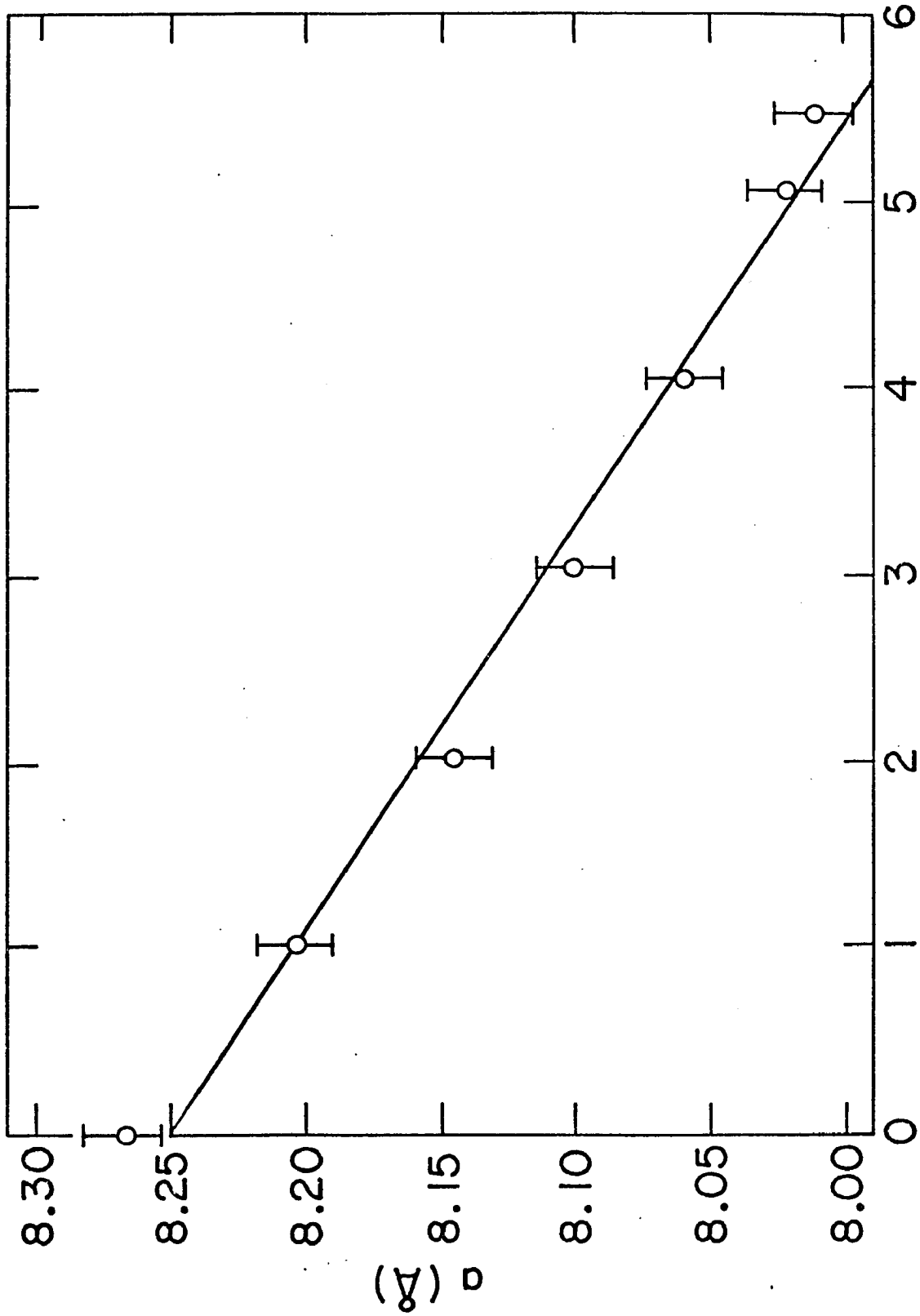

FIG. 2.8

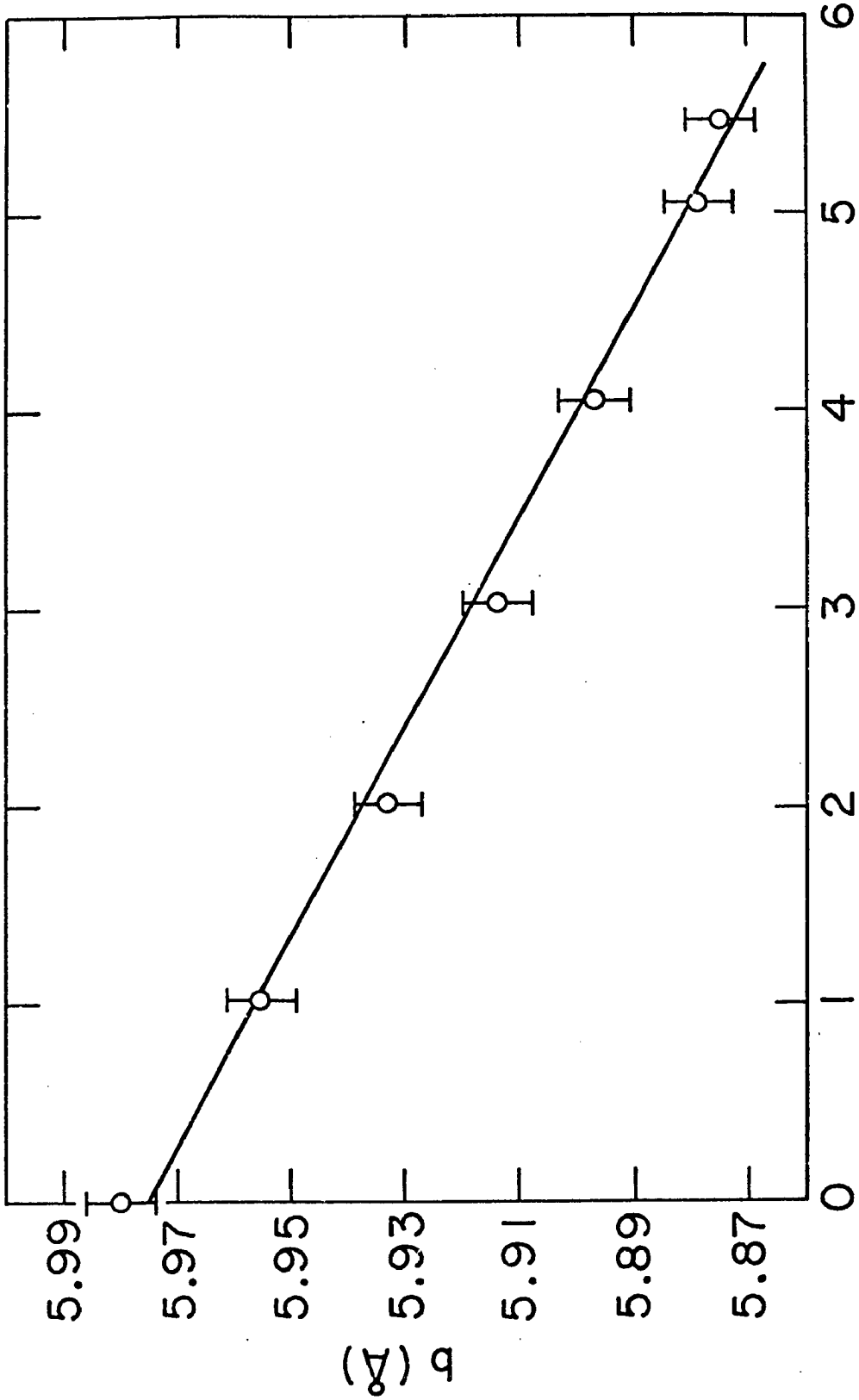

FIG. 2.9

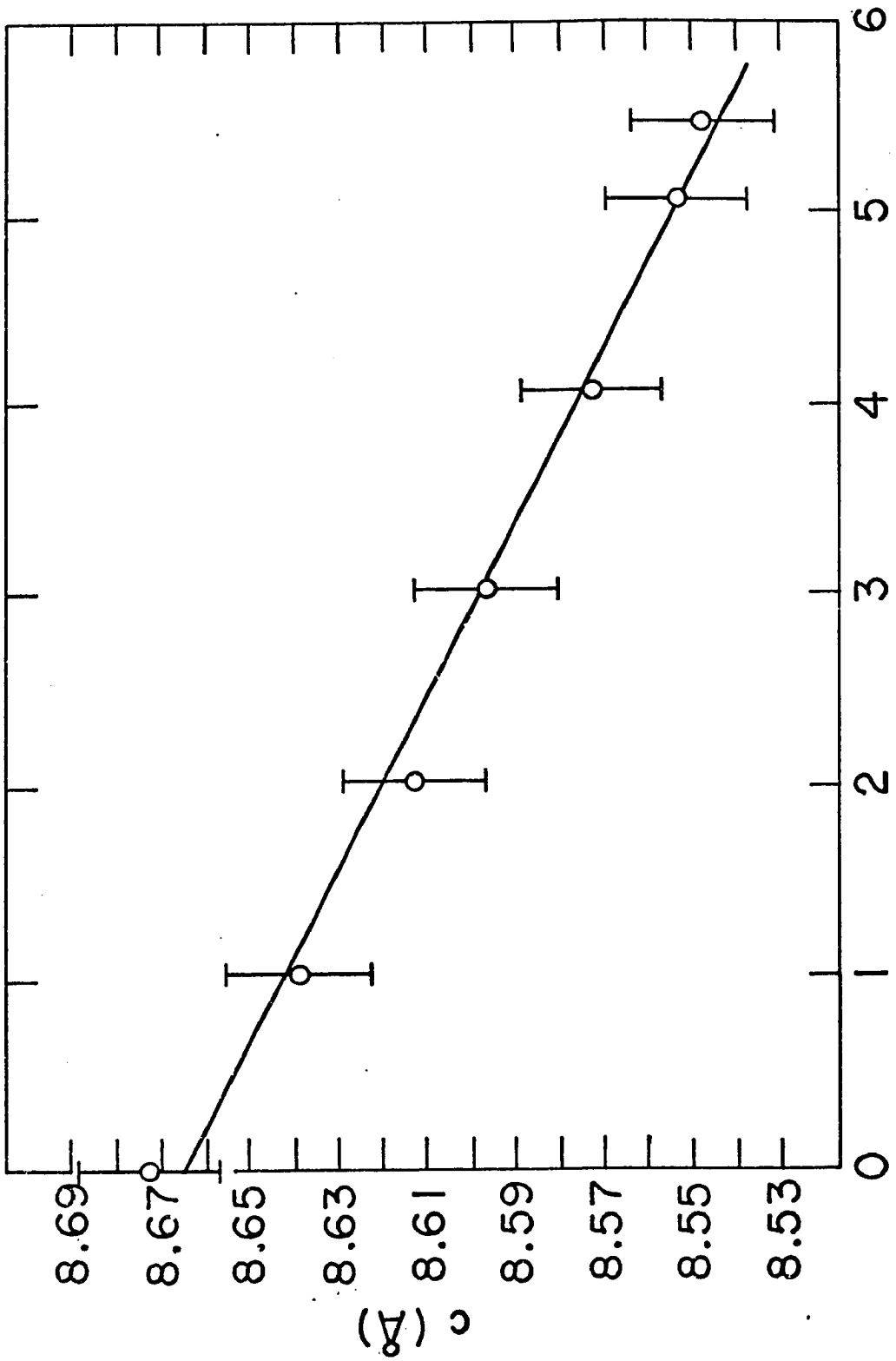

FIG. 2.10

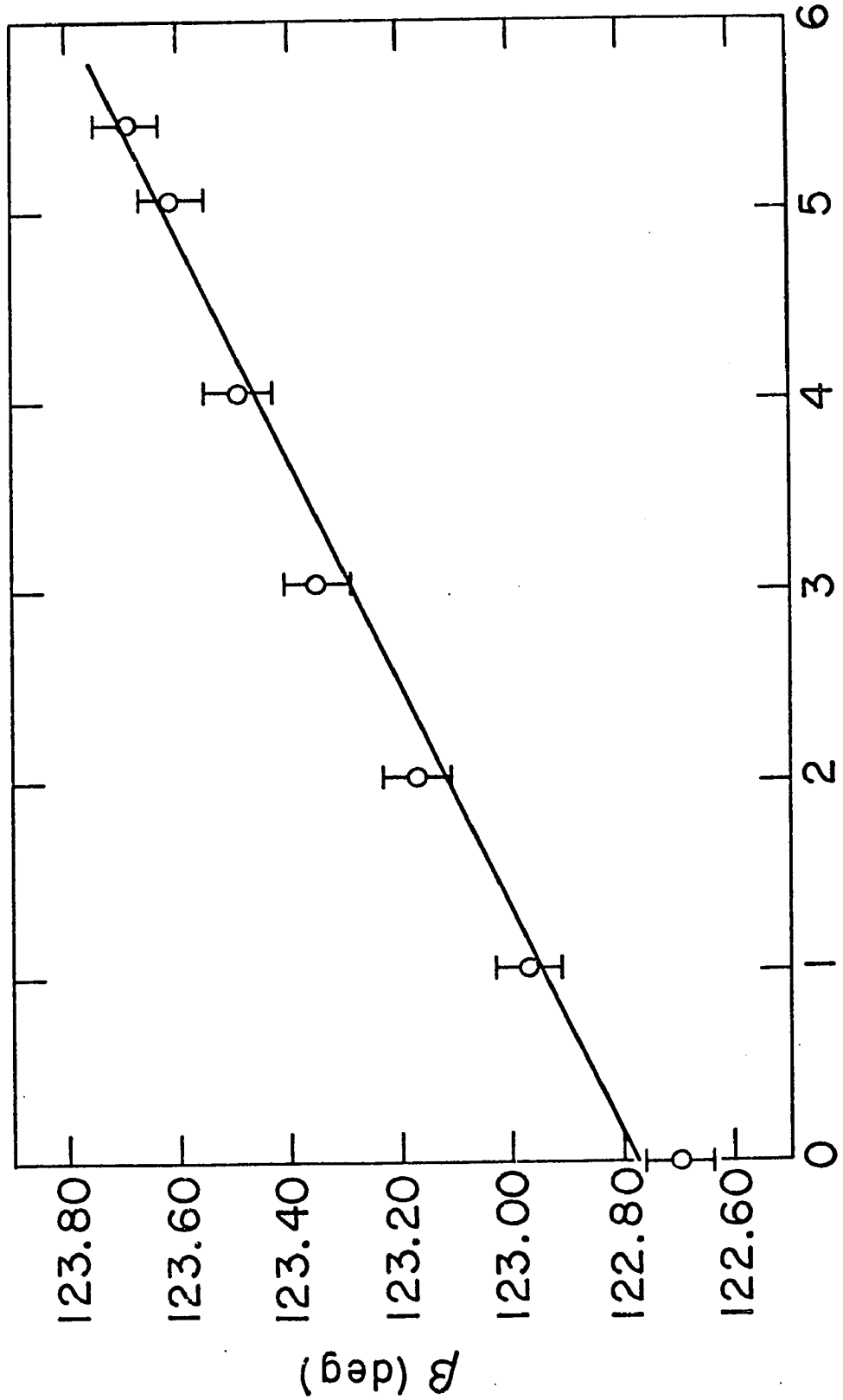

FIG. 2.11

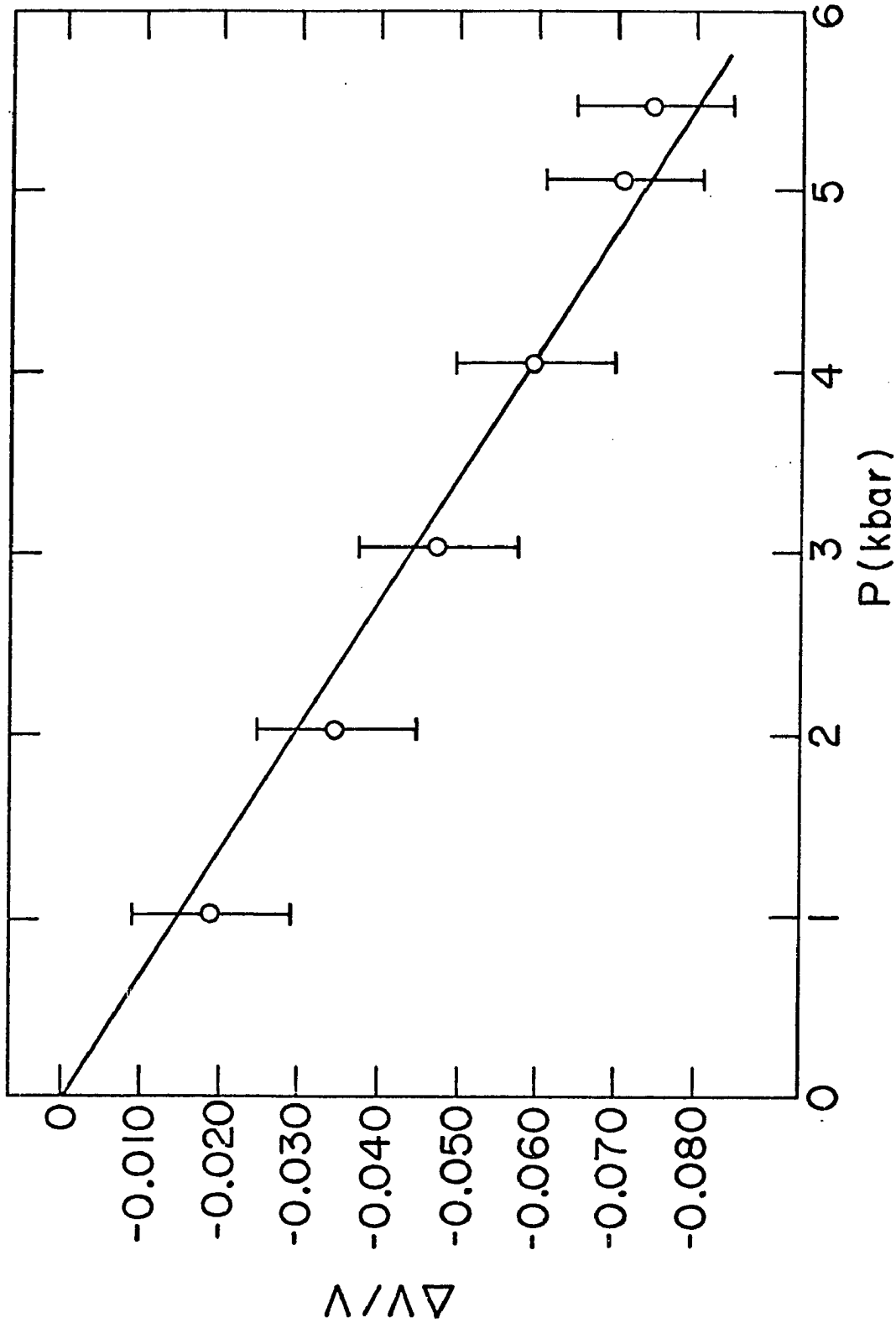

FIG. 2.12

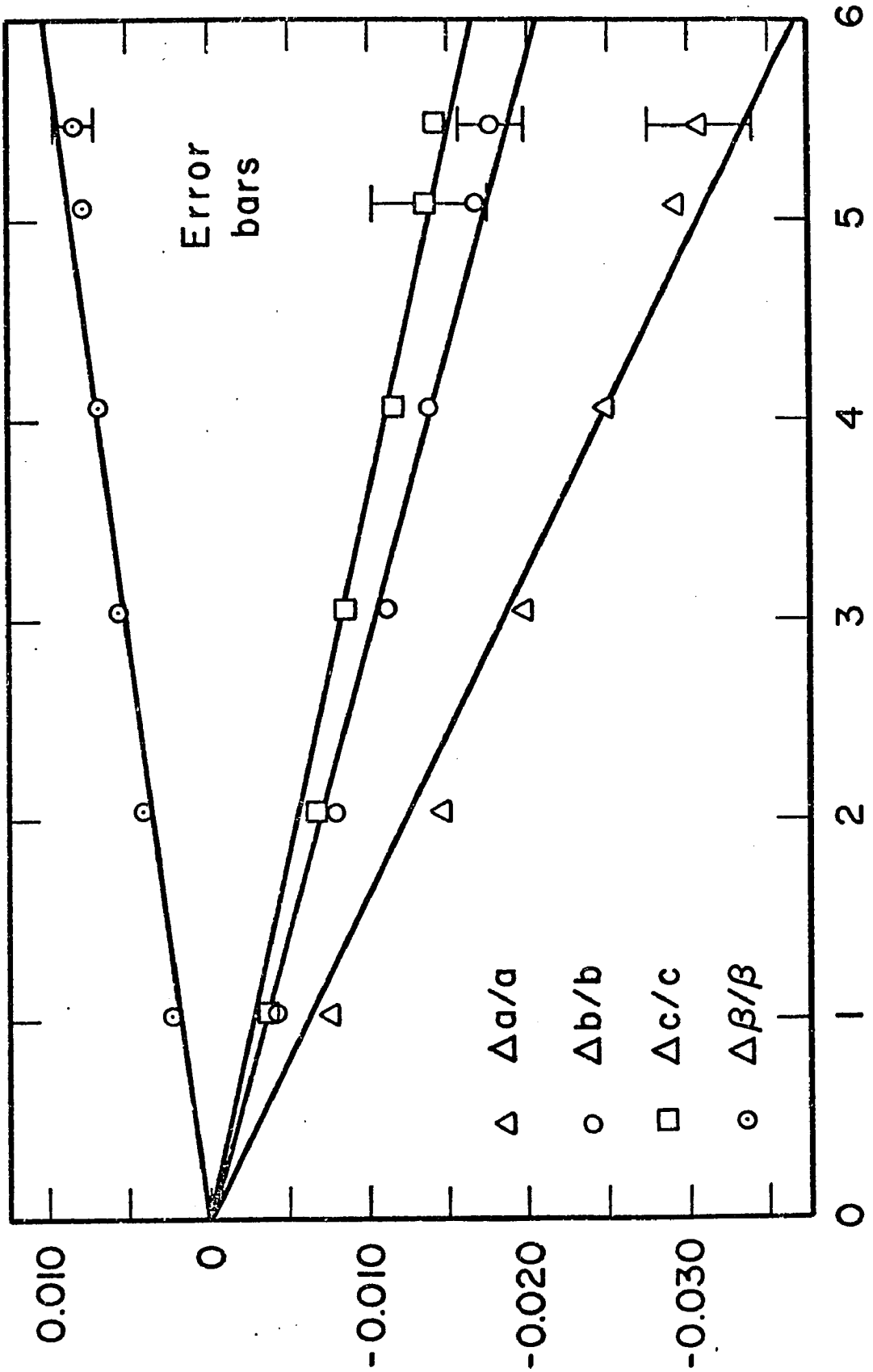

FIG. 2.13

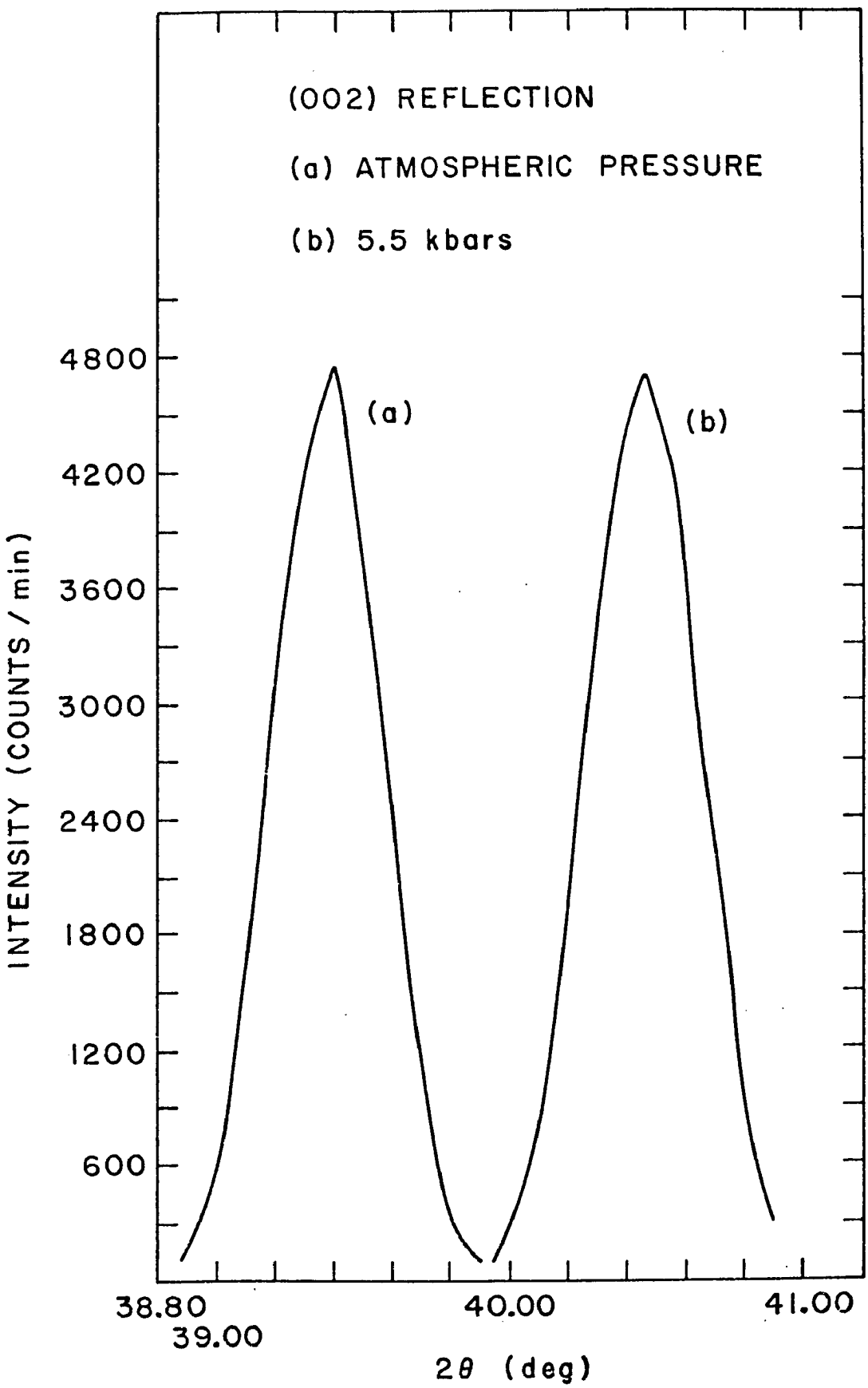

FIG. 2.14

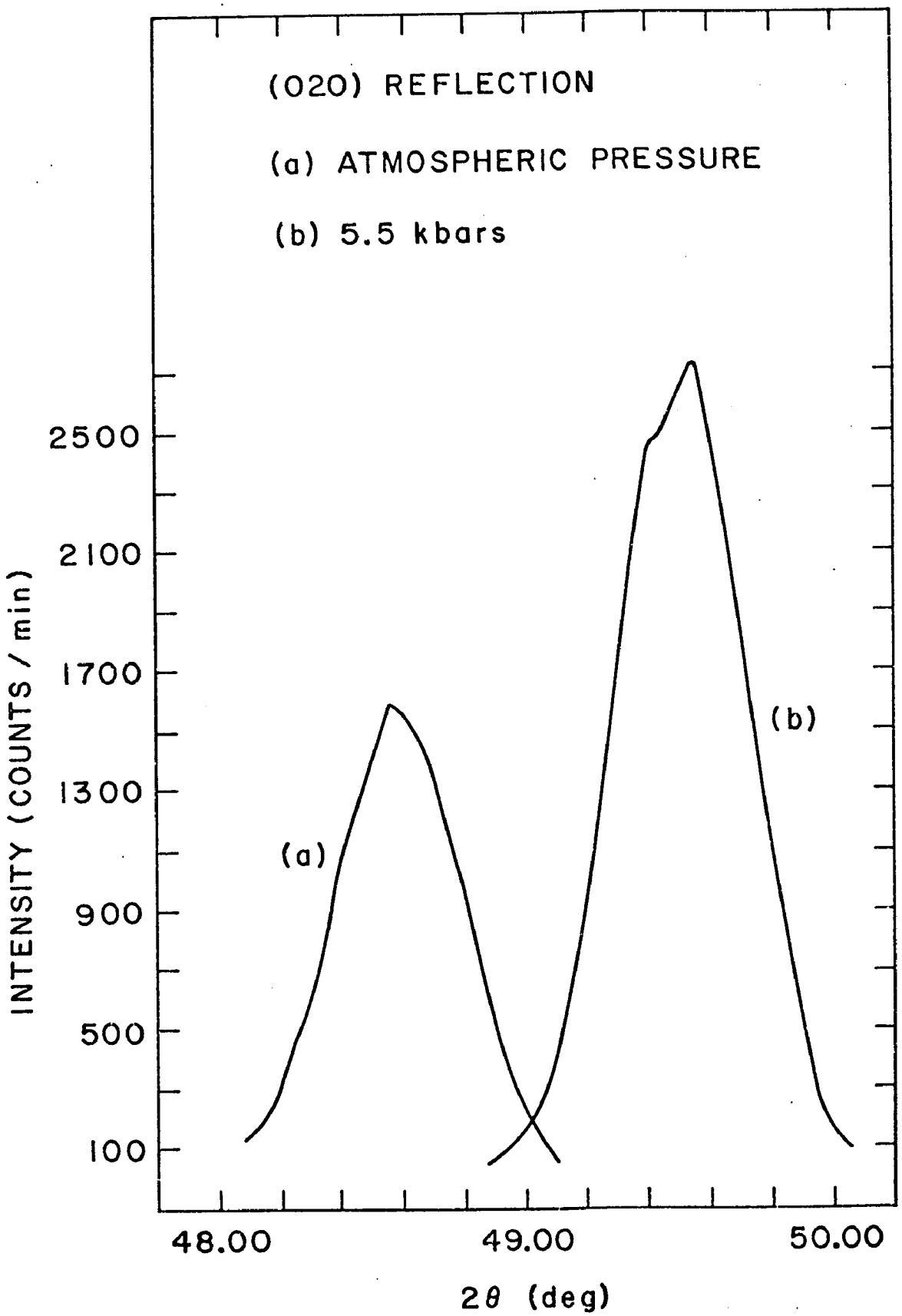

FIG. 2.15

Table 2.4 - Comparison of $\Delta V/V_o$ at 5 kilobars, obtained in this work, to the values reported by Bridgman[2] and Vaidya et al[5].

Bridgman	Vaidya et al	This work
0.063	0.062	0.070

Table 2.5 - Linear compressibilities obtained from the various sets of elastic constants of naphthalene.

Compress. \ Source	Aleksandrov et al[24]	Teslenko[25]	Afanas'eva[26]	Krupnyi et al[27]	Pawley[29]
α	0.077	0.086	0.081	0.100	0.085
κ	0.110	0.160	0.020	0.038	0.022
γ	-0.050	-0.158	0.044	0.069	0.111
δ	0.037	0.074	0.030	-0.005	-0.019

better non-linear least squares fitting of the velocities. The linear compressibilities obtained from the various sets are given in table 2.5 .

The problem that arises in finding the elastic constants matrix is that of calculating 13 components from the 18 Christoffel equations obtained from the six secular determinants corresponding to the various modes of wave propagation in the crystal[29,30]. Of these 13 components, only three, C_{22}, C_{44} and C_{66}, are given directly as ρv_k^2 (ρ is the crystal density and v_k is the velocity of a purely transverse or purely longitudinal wave)[28]. The remaining ten components are then calculated in terms of definite combinations of constants and velocities. If all the velocities of the elastic waves had been measured precisely, then all 18 equations would have been strictly satisfied. Since the velocities are measured with a certain error, however, not all these equations will be satisfied, and it becomes difficult to bring the calculated C_{ij} into maximum compatibility with all the measured v_k ; as a result, the error in the calculation of certain components can be as high as 30-40% , even though the velocities were measured to within 1-2%[24]. This can then explain the discrepancies between the linear compressibilities obtained from the neutron diffraction experiment and those calculated from the various published sets of elastic constants (see table 2.5).

However, the linear compressibilities obtained from Afanas'eva's set[26] were, in general, much closer to the corresponding experimental values than the compressibilities calculated from any of the other sets. But still, the predicted values of 0.081, 0.020, 0.044 and 0.030 for the compressibilities along a, b, c and β respectively, were out of the range of the experimental errors. An attempt was therefore made to determine a set of elastic constants for naphthalene that would correspond to the experimental results.

The starting point for this attempt was Afanas'eva's set, which has the additional advantage of associating error limits to each component of the elastic tensor (due to possible errors in the ultrasonic velocities). The various errors are given in table 2.6 .

First, the elastic constants were allowed to vary within the limits of Afanas'eva's errors. The interval for each component is shown in the last column of table 2.6 . The sizes of the increments given to each elastic constant were the result of a compromise between two factors;

Table 2.6 - Afanas'eva's[26] set of elastic constants and the errors associated with each component.

C_{ij}	Lower limit	Afanas'eva's set		Upper limit	Intervals
C_{11}	7.78	8.19	5%	8.60	7.78 - 8.60
C_{22}	9.72	10.02	2-3%	10.32	9.72 - 10.32
C_{33}	11.81	12.43	5%	13.05	11.81 - 13.05
C_{44}	3.34	3.44	2-3%	3.54	3.34 - 3.54
C_{55}	2.23	2.34	5%	2.45	2.23 - 2.45
C_{66}	4.30	4.43	2-3%	4.56	4.30 - 4.56
C_{12}	4.73	5.56	10-15%	6.39	4.73 - 6.39
C_{13}	3.06	3.22	5%	3.38	3.06 - 3.38
C_{23}	2.96	3.48	10-15%	4.00	2.96 - 4.00
C_{15}	0.10	0.20	30-50%	0.30	0.10 - 0.30
C_{25}	0.95	1.90	30-50%	2.85	0.95 - 2.85
C_{35}	-4.35	-2.90	30-50%	-1.45	-4.35 - -1.45
C_{46}	0.35	0.70	30-50%	1.05	0.35 - 1.05

the first one was to have reasonably small variations of the compressibilities with those increments, while the second one was to have manageable computation times on the computer. To satisfy these requirements, the partial derivatives of the compressibilities with respect to the elastic constants were calculated. The results are given in table 2.7 .

In a preliminary run, 10^6 different sets of elastic constants were scanned by the computer; as a result, one set was picked that gave the compressibilities α, κ, γ and δ within 16%, 15%, 40% and 65% respectively, from the corresponding neutron diffraction values. In a second run, the components of this particular set were allowed to vary around their values with much smaller increments, the purpose being to refine the results of the first scan. The set of elastic constants resulting from this last run is given in table 2.8 .

The linear compressibilities obtained from this set (see table 2.9) still differed, on the average, by about 32% from the corresponding neutron diffraction data. And since the standard deviations of the experimental compressibilities did not exceed 10% , another scan was performed to get a new set of elastic constants that would exactly match the neutron data. No attempt was made to keep the components of the elastic constants matrix within the ranges specified by Afanas'eva.

A procedure similar to the previous one was followed, except that the compliance matrix components, rather than the elastic matrix components, were varied. This allowed a more direct convergence to the required set of elastic constants. In this scan, the elements of the compliance matrix corresponding to the set given in table 2.8 were varied. As a result, the set of elastic constants predicting linear compressibilities equal to the experimental values (table 2.2) is given in table 2.10 . Table 2.11 gives the corresponding compressibilities, along with the experimental values.

Several checking routines were performed on this set. The first check was on the uniqueness of the values of the elastic constants predicting the experimental compressibilities. For this purpose, a scan on the values of the components of the elastic constants matrix was performed, starting with the set given in table 2.10 and running through the values published by Afanas'eva (table 2.6). In this particular scan, all sets predicting the experimental compressibilities were found to differ by less than 2%

Table 2.7 - Partial derivatives of the compressibilities with respect to Afanas'eva's[26] set of elastic constants of naphthalene.

ij	$\frac{\partial \alpha}{\partial C_{ij}}$	$\frac{\partial \kappa}{\partial C_{ij}}$	$\frac{\partial \gamma}{\partial C_{ij}}$	$\frac{\partial \delta}{\partial C_{ij}}$
11	0.0169	-0.0114	0.0015	0.0005
12	-0.0072	0.0222	0.0041	0.0116
13	0.0154	-0.0218	-0.0004	-0.0130
15	0.0220	-0.0430	-0.0197	-0.0368
22	-0.0028	0.0061	0.0009	0.0028
23	-0.0096	0.0185	0.0028	0.0066
25	-0.0067	0.0111	-0.0022	-0.0002
33	0.0007	-0.0103	-0.0015	-0.0115
35	0.0083	-0.0387	-0.0192	-0.0423
44	0.0000	0.0000	0.0000	0.0000
46	0.0000	0.0000	0.0000	0.0000
55	0.0069	-0.0266	-0.0162	-0.0290
66	0.0000	0.0000	0.0000	0.0000

Table 2.8 - Set of elastic constants obtained in the preliminary scan.

ij	C_{ij}
11	8.60
22	9.70
33	12.90
44	3.35
55	2.40
66	4.22
12	5.50
13	3.40
23	3.40
15	0.20
25	0.90
35	-3.10
46	0.70

Table 2.9 - Linear compressibilities obtained from the set of elastic constants given in table 2.8 .

α	κ	γ	δ
0.0648	0.0366	0.0357	0.0227

Table 2.10 - Set of elastic constants giving linear compressibilities equal to the experimental values.

ij	C_{ij}
11	9.837
22	10.879
33	16.273
44	3.350
55	2.517
66	4.220
12	6.769
13	4.794
23	4.800
15	0.175
25	0.966
35	-3.593
46	0.700

Table 2.11 - Comparison of the compressibilities obtained from the set of C_{ij}'s given in table 2.10 with the corresponding experimental values.

	α	$\varkappa$	γ	δ
Calculations	0.0560	0.0320	0.0265	0.0147
Experimental	0.0560	0.0320	0.0262	0.0144

Table 2.12 - Range of the C_{ij}'s for 10% deviations in the linear compressibilities.

ij	Range of C_{ij}
11	9.30 - 10.20
22	10.60 - 11.00
33	15.25 - 17.00
44	3.35
55	2.35 - 2.60
66	4.22
12	5.80 - 7.20
13	3.80 - 5.20
23	4.00 - 5.20
15	0.17 - 0.23
25	0.85 - 1.30
35	-3.30 - -3.80
46	0.70

Table 2.13 - Comparison of the set of elastic constants obtained in this work with the one given by Pawley[29].

ij	C_{ij} (Pawley)	C_{ij} (this work)
11	6.8	9.837
22	11.3	10.879
33	17.4	16.273
44	4.7	3.350
55	3.1	2.517
66	2.7	4.220
12	5.8	6.769
13	4.8	4.794
23	4.7	4.800
15	-0.1	0.175
25	1.3	0.966
35	-4.2	-3.593
46	0.3	0.700

from the one given in table 2.10 . Since the experimental compressibilities had, on the average, a standard deviation of 10% (see table 2.2), another scan was performed to get a rough determination of the ranges in which each C_{ij} would be allowed to vary such that the resulting compressibilities would not differ by more than 10% from the experimental data. Table 2.12 gives the results of this scan, and it is seen that the ranges of the C_{ij}'s bracket the corresponding values shown in table 2.10 .

A last check was performed on the stability of a crystal having such a set of elastic constants. The stability criterion[31] is that the sum of the second-degree terms in the strain energy $\frac{1}{2} C_{ij}\epsilon_i\epsilon_j$ must be positive for any arbitrary values of the strains. This in turn is guaranteed if all the diagonal determinants of the elastic constants matrix are positive. This was found to be the case for the set given in table 2.10 .

Finally, a word of caution. The claim is not made that the correct elastic constants matrix for naphthalene is the one determined here. All that was meant from this research was to find a possible set of elastic constants that would correspond to the linear compressibilities obtained from the neutron diffraction data. This set is not much different from the one calculated by Pawley[29] from intermolecular potentials (see table 2.13). However, since the set presented in this work was based on experimental results of the elastic constants and the linear compressibilities, it is more reliable than Pawley's.

References - Chapter 2

1. A.I. Kitaigorodski, J. Chim. Phys., 63, 6 (1966).

2. P.W. Bridgman, Proc. Am. Acad. Arts Sci., 76, 9 (1945); 76, 71 (1948); 77, 129 (1949).

3. P.W. Bridgman, The Physics of High Pressure, p 155, Dover Publications, Inc., New York, 1970.

4. S.S. Kabalinka, Fiz. Tver. Tela., 4, 3124 (1962), (Sov. Phys. Solid State, 4, 2288 (1964)).

5. S.N. Vaidya and G.C. Kennedy, J. Chem. Phys., 55, 987 (1971).

6. J.F. Nye, Physical Properties of Crystals, chapter 8, Oxford University Press, New York, 1972.

7. O.H. Leblanc, Jr., Physics and Chemistry of the Organic Solid State, vol 3, (Eds. D. Fox, M.M. Labes and A. Weissberger), Interscience, New York, 1967.

8. M. Campos, G. Leal Ferreira and S. Mascarenhas, J. Electrochem. Soc., 115, 388 (1968).

9. M. Campos, Molec. Cryst. Liq. Cryst., 18, 105 (1972).

10. Y. Okamoto, F.T. Huang, A. Gordon, W. Brenner and B. Rubin, Organic Semiconductors, Proceedings of an Inter-Industry Conference, Chicago, april 1961, (Eds. J.J. Brophy and J.W. Buttrey), The MacMillan Co., New York, 1962.

11. F.R. Lipsett, Can. J. Phys., 35, 284 (1957).

12. D.M. Hanson and G.W. Robinson, J. Chem. Phys., 43, 4174 (1965).

13. G.J. Sloan, Physics and Chemistry of the Organic Solid State, vol 1, (Eds. D. Fox, M.M. Labes and A. Weissberger), Interscience, New York, 1967.

14. J.N. Sherwood, Methods and Techniques of Fractional Solidification, (Eds. M. Dekker and M. Zeif), New York, 1969.

15. G.J. Sloan, Private Communication.

16. F. Gutmann and L.E. Lyons, Organic Semiconductors, p 130, Wiley, Inc., New York, 1967.

17. J.N. Sherwood and S.J. Thomson, J. Sci. Inst., 37, 242 (1960).

18. R.C. Jarnagin, J. Gilliland, Jr., J.S. Kim and M. Silver, J. Chem. Phys., 39, 573 (1962).

19. I. Nakada, J. Phys. Soc. Japan, 17, 113 (1962).

20. G.E. Bacon, Neutron Diffraction, Oxford University Press, New York, 1962.

21. B.C. Loopstra, Nucl. Instr. Methods, 44, 181 (1966).

22. G. Shirane and V.J. Minkiewicz, Nucl. Instr. Methods, 89, 109 (1970).

23. S.A. Rice and J. Jortner, Physics of Solids at High Pressures, p 139, (Eds. C.T. Tomizuka and R.M. Emrick), Academic Press, New York, London, 1965.

24. K.S. Aleksandrov, G.S. Belikova, A.P. Ryzhenkov, V.F. Teslenko and A.I. Kitaigorodski, Kristallografiya, 8, 221 (1963), (Sov. Phys.- Crystallogr., 8, 164 (1963)).

25. V.F. Teslenko, Kristallografiya, 12, 1082 (1967), (Sov. Phys.- Crystallogr., 12, 946 (1968)).

26. G.K. Afanas'eva, Kristallografiya, 13, 1024 (1968), (Sov. Phys.- Crystallogr., 13, 892 (1969)).

27. A.I. Krupnyi, V.V. Al'chikov and K.S. Aleksandrov, Kristallografiya, 16, 801 (1971), (Sov. Phys.- Crystallogr.,16, 692 (1972)).

28. K.S. Aleksandrov, Kristallografiya, 3, 623 (1958), (Sov. Phys.- Crystallogr., 3, 630 (1959)).

29. G.S. Pawley, Phys. Stat. Sol., 20, 347 (1967).

30. J. De Launay, Solid State Phys., 2, 219 (Eds. F. Seitz and D. Turnbull), Academic Press, New York, 1956.

31. L. Brillouin, Tensors in Mechanics and Elasticity, Academic Press, New York, 1964.

Chapter Three

Pressure Dependence of the Band Structure of Naphthalene

1. Introduction

Mobility measurements in molecular crystals involve the injection of excess holes or electrons in extremely small concentrations (for e.g. 10^{10} cm^{-3} or smaller in naphthalene[1]). At this dilution, the interaction between the excess carriers is negligible so that a one-particle treatment may be used. And because the interactions between molecules ($\sim 10^{-2}$ ev) are small compared to the intramolecular excitation energies (>1 ev), the tight binding approximation[2] may be employed to calculate the carrier band structure. As a result, for a monoclinic crystal such as naphthalene having two distinguishable molecules (by virtue of orientation) per unit cell (see fig.1.1), the electronic bands will be expected to have two branches corresponding to the symmetric and antisymmetric combinations of the basic molecular wavefunctions within the unit cell.

The tight binding approximation was used by a number of investigators[3-8] to calculate increasingly more reliable carrier band structures. It consists in constructing one-electron crystal wavefunctions from linear combinations of one-electron molecular wavefunctions $\phi(\vec{r})$. As shown by Katz et al[5], the possible linear combinations adapted for the translational symmetry of the crystal are:

$$\Psi_{\pm}(\vec{k}) = \sum_{l=0}^{2N-1} (\pm 1)^{l} \exp\left(i \vec{k} \cdot \vec{r}_l\right) \phi\left(\vec{r} - \vec{r}_l\right) \qquad (3.1)$$

where N is the number of unit cells in the crystal, and the index l labels the molecules so that the molecule at the corner of each cell has an even index, while the one at the center of the cell has an odd index. $\vec{r}_l$ is the vector to the center of each molecule and $\phi(\vec{r} - \vec{r}_l)$ has a different orientation in space depending on whether l is even or odd. In order to constitute an appropriate basis for the construction of crystal wavefunctions $\Psi_{\pm}(\vec{k})$, the molecular wavefunctions $\phi(\vec{r} - \vec{r}_l)$ should form an orthonormal set, i.e.

$$\int \phi(\vec{r} - \vec{r}_n)\, \phi(\vec{r} - \vec{r}_m)\, d\tau = \delta_{nm} \qquad (3.2)$$

The values of these integrals (overlap integrals) are not zero, but are

still practically negligible ($\ll 5\times10^{-3}$ for nearest neighbor molecules[5]). Devaux[9] took their effect into consideration in an attempt to improve the calculations of the charge transfer integrals (TIs) in naphthalene crystals: the resulting TIs had essentially the same values as those previously calculated without overlap[5,6], so that the effect of the overlap integrals will be neglected in the present work.

2. Crystal Wavefunction for an Excess Electron (or Hole)

2a. Molecular Wavefunction for an Isolated Molecular Ion

The first step in calculating the band structure of naphthalene is the selection of a suitable molecular wavefunction for the molecular ion. Balk et al[10] and then Katz et al[5] have shown that the properties of isolated aromatic ions can be understood if the excess electron is described by the wavefunction corresponding to the first unoccupied molecular orbital of the neutral molecule (for an excess hole: the highest occupied orbital), assuming that the interaction between electron (or hole) and molecule caused no change in the orbital in question.

To obtain the molecular orbitals of the neutral molecule the π-electron approximation was used: the σ-electrons are ignored and only the π-electrons are considered, assuming that their motion is governed by an effective Hamiltonian that incorporates the average effect of the σ-electrons. The molecular orbitals of a positive or negative ion are then approximated by Huckel[11] linear combinations of Slater type $2p_z$ orbitals u_i[12]:

$$\phi_n = \sum_i C_{n,i}\, u_i \qquad (3.3)$$

using for the electron and hole band, respectively, the Huckel coefficients $C_{n,i}$ for the lowest antibonding and highest bonding π orbitals.

Other coefficients $C_{n,i}$ were calculated by Hoyland and Goodman[13] by taking into consideration the deformation of orbitals resulting from the excess charge. Since they were able to predict more reliable ionization spectra for the hydrocarbons, the Hoyland and Goodman coefficients $C_{n,i}$ for naphthalene were used in this work: they are given in table 3.1 and the resulting symmetry of the molecular orbitals shown in fig. 3.1

2b. Molecular Wavefunction of a Molecular Ion in a Crystal

The wavefunction of the molecular ion will be modified by the crys-

Table 3.1 - Hoyland and Goodman coefficients for naphthalene[13].

Atom # \ Carrier	Hole	Electron
1	0.43133	0.43072
2	0.25290	-0.25393
3	-0.25290	-0.25393
4	-0.43133	0.43072
5	0.43133	-0.43072
6	0.25290	0.25393
7	-0.25290	0.25393
8	-0.43133	-0.43072
9	0	0
10	0	0

Table 3.2 - Orbital exponents[b] and expansion coefficients of the carbon atom wavefunctions[14].

α_i	a_i
6.3438	0.01090
2.5873	0.23563
1.4209	0.57773
0.9554	0.24756

[b] All orbital exponents α_i are in atomic units.

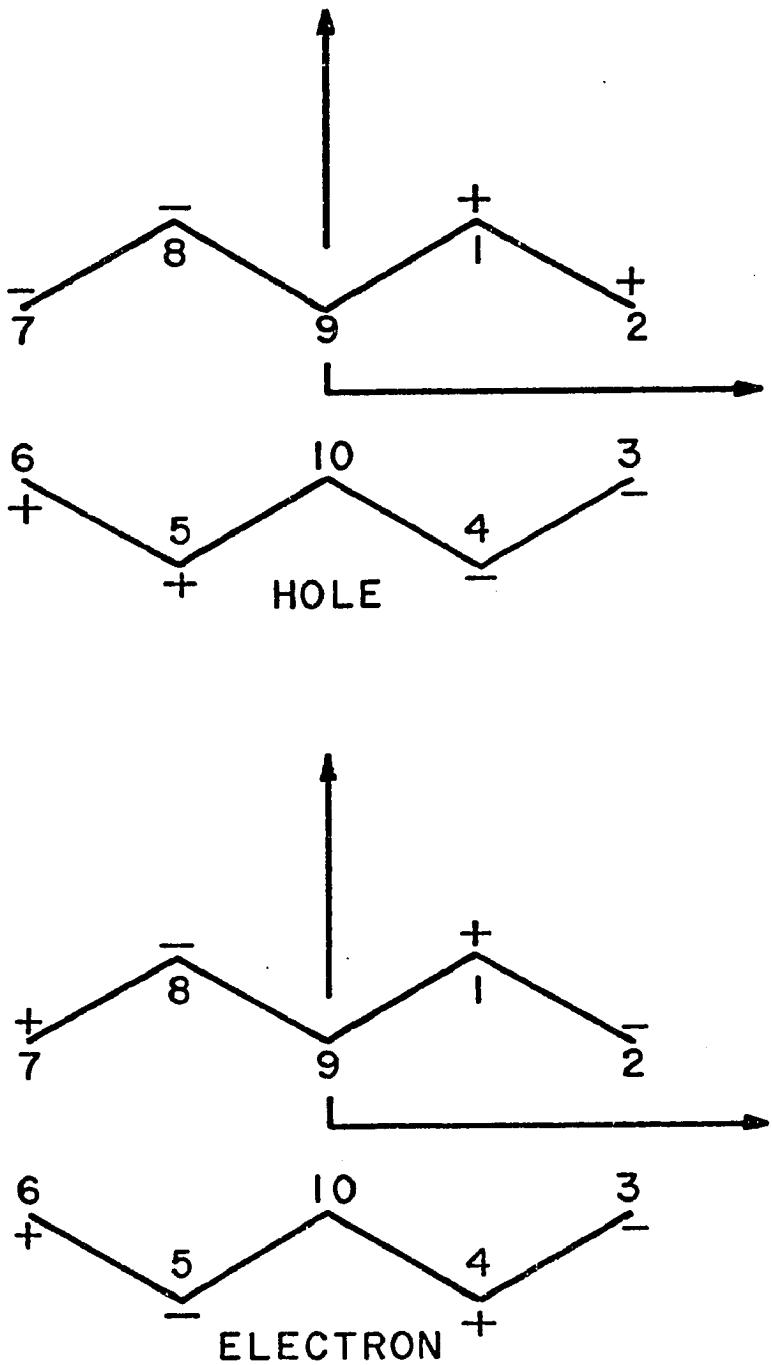

FIG. 3.1

talline environment to take into consideration polarization and exchange effects, as well as vibrational overlaps.

(i) Exchange[6] and Polarization Effects[7]:

The indistinguishability of the electrons requires the use of a wavefunction that is antisymmetric with respect to the exchange of the electrons of all molecules. The crystal wavefunction will thus be formed from an antisymmetrized product of molecular wavefunctions, in which one molecule is either a negative or a positive ion and the remainder are perturbed (polarized) by the ionic molecule. Symbolically, the wavefunction $\phi(\vec{r}-\vec{r}_i)$ corresponding to the electron or hole being on molecule i is now written as $\phi_i(\vec{r}-\vec{r}_i)$:

$$\Phi_i = \mathcal{A}\, \psi_i(2a \pm 1) \prod_{j \neq i} \psi_j^{(i)}(2a) \qquad (3.4)$$

$\mathcal{A}$ being the antisymmetrization operator (Slater determinant); "a" is the number of filled orbitals in the neutral molecule, $\psi_i(2a\pm1)$ denotes the wavefunction of the appropriate molecular ion i, and $\psi_j^{(i)}$ the wavefunction of molecule j in the field of this molecular ion.

(ii) Vibrational Wavefunction of the Molecule[6]:

The effect of molecular vibrations is included by taking the molecular wavefunctions as the product of an electronic part and a vibrational part. This representation corresponds to the weak-coupling limit of vibronic interaction. Using such an approximation, the symmetrized wavefunctions of the crystal with an excess or deficiency of one electron may be written in the form[6]:

$$\Psi_{\pm}(\vec{K}) = \sum_{\ell=0}^{2N-1} (\pm 1)^{\ell} \exp(i\vec{K}\cdot\vec{\ell})\, \mathcal{A}\, \phi_{\ell}^{k}(1) \times \prod_{i=0}^{2N-1} \left(\phi_i^{1}(i,1) \cdots\cdots \bar{\phi}_i^{a}(i,2a)\chi_i \right) \qquad (3.5)$$

where ϕ^k is the lowest unoccupied molecular orbital of a molecule for electrons and the highest occupied orbital for holes, the ϕ_i are the "a" occupied molecular orbitals of molecule i, the bar over ϕ_i^a means that the electron in that molecular orbital has β spin, and χ_i is the ground state vibrational wavefunction of the i^{th} molecule. It is assumed that all the vibrational wavefunctions are the same except for that of the molecule with an excess electron (or hole).

2c. Atomic Wavefunctions

The transfer integrals of molecular crystals are very sensitive to the detailed form of the molecular wavefunctions, and in particular to their behavior at large distances. The use of single Slater orbitals (u_i in eq.(3.3)) characterized by a single exponent was found to be inappropriate, because it underestimated the magnitude of the tails of the wavefunctions[5].

The best available fit to the SCF functions was obtained by using a carbon atom wavefunction represented in the form of a linear combination of four Slater wavefunctions[14]

$$u_i(\vec{r}) = (\hat{n}_i \cdot \vec{r}) \sum_{i=1}^{4} a_i (\alpha_i^5/\pi)^{1/2} \exp(-\alpha_i r) \qquad (3.6)$$

where $\hat{n}_i$ is the unit vector defining the direction of the $2p_z$ orbital. The coefficients a_i and orbital exponents α_i were obtained by Clementi et al[14] and are given in table 3.2 .

3. Method of Calculation of the Energy Band Structure

Following the treatment outlined by Katz et al[5], the energy of the excess electron or hole is given by

$$E_{\pm}(\vec{K}) = \frac{\langle \Psi_{\pm}(\vec{K}) | H | \Psi_{\pm}(\vec{K}) \rangle}{\langle \Psi_{\pm}(\vec{K}) | \Psi_{\pm}(\vec{K}) \rangle} \qquad (3.7)$$

where the Hamiltonian H appropriate to an excess electron or hole has the form

$$H = -\left(\frac{\hbar^2}{2m}\right) \nabla^2 + V(\vec{r}) \qquad (3.8)$$

with

$$V(\vec{r}) = \sum_n V_n(\vec{r} - \vec{r}_n) \qquad (3.9)$$

where V_n is the Hartree potential of an isolated neutral molecule.

To obtain $E(\vec{K})$, eqs.(3.8) and (3.9) are substituted into eq.(3.7). This gives:

$$E_{\pm}(\vec{K}) = e_0 + \sum_n{}' e_n + \sum_{\ell} (\pm 1)^{\ell} \cos(\vec{K} \cdot \vec{r}_{\ell})\, e_{\ell} \qquad (3.10)$$

where

$$e_0 = \int \phi^*(\vec{r}) \left[-\frac{\hbar^2}{2m} \nabla^2 + V_0(\vec{r}) \right] \phi(\vec{r})\, d\tau \qquad (3.11)$$

$$e_n = \int \phi^*(\vec{r})\, V_n(\vec{r} - \vec{r}_n)\, \phi(\vec{r})\, d\tau \qquad (3.12)$$

$$e_\ell = \int \phi^*(\vec{r}-\vec{r}_\ell)\, V_\ell\,(\vec{r}-\vec{r}_\ell)\,\phi(\vec{r})\,d\tau \qquad (3.13)$$

All three-center integrals whose centers lie on three different molecules, as well as all overlap integrals multiplied by e_n or e_ℓ, were neglected in eq.(3.10). In order to get the $\vec{K}$ variation of the energy bands, it is only necessary to examine the last term in eq.(3.10)

$$E'_\pm(\vec{K}) \equiv E_\pm(\vec{K}) - e_o - \sum_n{}' e_n = \sum_\ell (\pm 1)^\ell \cos(\vec{K}\cdot\vec{r}_\ell)\, e_\ell \qquad (3.14)$$

and by taking into consideration only nearest neighbor interactions with molecule 1 whose center is located at the origin (see fig.3.2), the energy dependence on $\vec{K}$ becomes

$$\begin{aligned}
E'_\pm(\vec{K}) = {} & 2E_2\cos(\vec{K}\cdot\vec{c}) + 2E_3\cos(\vec{K}\cdot\vec{b}) \\
& + 2E_4\left[\cos\vec{K}\cdot(\vec{b}+\vec{c}) + \cos\vec{K}\cdot(\vec{b}-\vec{c})\right] \\
& + 2E_5\cos(\vec{K}\cdot\vec{a}) + 2E_6\cos\vec{K}\cdot(\vec{c}+\vec{a}) \\
& + 2E_7\left[\cos\vec{K}\cdot(\vec{a}+\vec{b}) + \cos\vec{K}\cdot(\vec{a}-\vec{b})\right] \\
& + 2E_8\left[\cos\vec{K}\cdot(\vec{a}+\vec{b}+\vec{c}) + \cos\vec{K}\cdot(\vec{a}-\vec{b}+\vec{c})\right] \\
& \pm 2E_9\left[\cos\vec{K}\cdot\tfrac{1}{2}(\vec{a}+\vec{b}) + \cos\vec{K}\cdot\tfrac{1}{2}(\vec{a}-\vec{b})\right] \\
& \pm 2E_{10}\left\{\cos\vec{K}\cdot\left[\tfrac{1}{2}(\vec{a}+\vec{b})+\vec{c}\right] + \cos\vec{K}\cdot\left[\tfrac{1}{2}(\vec{a}-\vec{b})+\vec{c}\right]\right\} \\
& \pm 2E_{11}\left\{\cos\vec{K}\cdot\left[\tfrac{1}{2}(\vec{b}-\vec{a})+\vec{c}\right] + \cos\vec{K}\cdot\left[\vec{c}-\tfrac{1}{2}(\vec{a}+\vec{b})\right]\right\} \\
& + 2E_{12}\left[\cos\vec{K}\cdot(\vec{c}-\vec{a})\right] \\
& + 2E_{13}\left[\cos\vec{K}\cdot(\vec{b}-\vec{a}+\vec{c}) + \cos\vec{K}\cdot(\vec{c}-\vec{a}-\vec{b})\right] \\
& \pm 2E_{14}\left[\cos\vec{K}\cdot\tfrac{1}{2}(\vec{a}+3\vec{b}) + \cos\vec{K}\cdot\tfrac{1}{2}(\vec{a}-3\vec{b})\right]
\end{aligned} \qquad (3.15)$$

where the 13 E_i are the transfer integrals between molecules 1 and i such as given by e_ℓ in eq.(3.13). The molecular structure of naphthalene used in this work was the one published by Cruickshank[15], while the pressure dependence of the lattice parameters was taken from the previous chapter.

3a. Intermolecular Resonance Integrals

The potential $V_n(\vec{r}-\vec{r}_n)$ of a neutral molecule is taken to be the sum of the potentials of its neutral atoms

$$V_n = \sum_C V_C + \sum_H V_H \qquad (3.16)$$

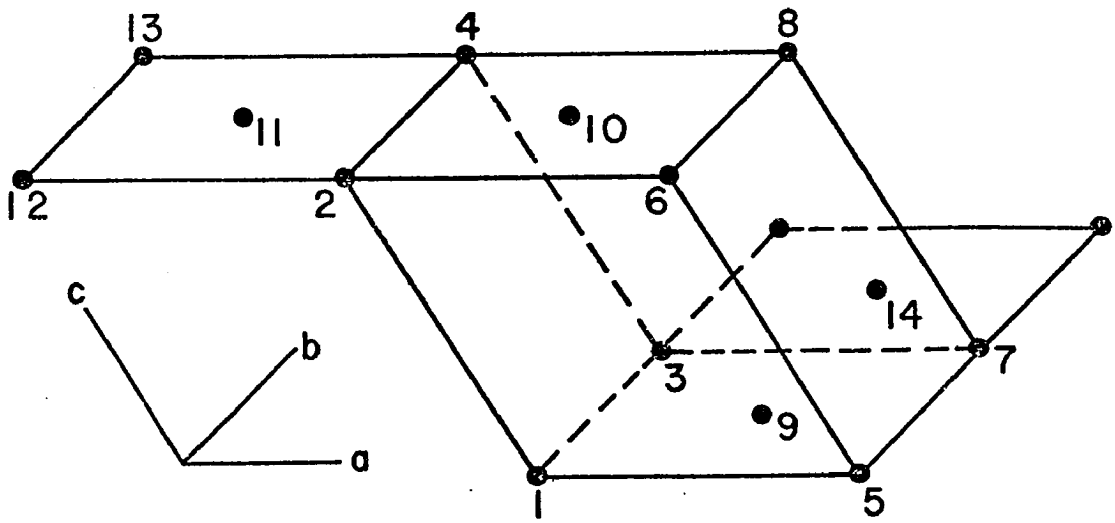

FIG. 3.2

However, corrections to the ε_ℓ's due to the introduction of V_H were shown by Tanaka and Niira[8] not to exceed 10^{-3}ev, while values for ε_ℓ could reach 10^{-2}ev. Therefore, the contribution of the hydrogen atoms will be neglected, and eq.(3.16) becomes:

$$V_n = \sum_C V_C \tag{3.17}$$

This same result can be obtained from the Hartree potential of the neutral molecule. The potential V_n of the neutral molecule can be written as[6]:

$$V_n = \sum_C V^{core} + 2 \sum_{i=o}^{a} J_n^i \tag{3.18}$$

where $\sum_C V^{core}$ is due to the ensemble core plus σ-electrons and J_n^i is the Coulomb potential of the i^{th} molecular orbital of the n^{th} molecule. It is given by[16]:

$$J_n^i \phi_m^j(1) = e^2 \int \frac{\phi_n^i(2)\,\phi_n^i(2)}{r_{12}}\, d\tau_2\, \phi_m^j(1) \tag{3.19}$$

The potential V_C of a neutral carbon atom can be written as:

$$V_C = V^{core} + V_{2p_z} \tag{3.20}$$

Substituting into eq.(3.18) gives:

$$V_n = \sum_C \left(V_C - V_{2p_z} \right) + 2 \sum_{i=o}^{a} J_n^i \tag{3.21}$$

But the π-electrons are uniformly distributed in the neutral molecule[17]. Thus:

$$\sum_C V_{2p_z} = 2 \sum_{i=o}^{a} J_n^i \tag{3.22}$$

which leads to

$$V_n = \sum_C V_C \tag{3.17}$$

The potential V_C was calculated by Goeppert-Mayer and Sklar[18] to be:

$$V_C = -\frac{e^2}{r_c} \left(\sum_{k,\ell} \frac{a_\ell \alpha_\ell^{5/2} a_k \alpha_k^{5/2}}{\beta_{k\ell}^5} \right)^{-1} \sum_{k,\ell} \exp\left(-2\beta_{k\ell} r_c\right) \times$$

$$\frac{a_k \alpha_k^{5/2} a_\ell \alpha_\ell^{5/2}}{\beta_{k\ell}^5} \left[\frac{4}{3} \left(\beta_{k\ell} r_c\right)^3 + 4\left(\beta_{k\ell} r_c\right)^2 + 6\left(\beta_{k\ell} r_c\right) + 4 \right] \tag{3.23}$$

where $\beta_{kl} = 1/2(\alpha_k + \alpha_l)$; $\sum V_C$ will be referred to from now on as V_{GMS}.

The intermolecular resonance integrals are then obtained by using eqs.(3.3),(3.6),(3.17) and (3.23) in eq.(3.13)

$$e_\ell = \int \phi(\vec{r})\, V(\vec{r})\, \phi(\vec{r} - \vec{r}_\ell)\, d\tau$$

$$= \sum_{i,j,m} C_{\alpha,i}\, C_{\beta,j} \int u_i(\vec{r} - \vec{r}_i)\, V_m(\vec{r} - \vec{r}_m)\, u_j(\vec{r} - \vec{r}_\ell - \vec{r}_j)\, d\tau \qquad (3.24)$$

where the two-center resonance integral is the sum of all terms for which i=m (100 terms), while the sum of the remaining terms (900 terms) gives the three-center contribution of the resonance integral.

3b.Exchange Integrals and Vibrational Overlap

When exchange interactions are taken into consideration[6], the potential $V_n(\vec{r} - \vec{r}_n)$ of the neutral molecule becomes:

$$V_n(\vec{r} - \vec{r}_n) = \sum_C V^{core} + \sum_{i=0}^{a} (2J_n^i - K_n^i)$$

$$= V_{GMS} - \sum_{i=0}^{a} K_n^i \qquad (3.25)$$

where K_n^i is the exchange potential of the i^{th} molecular orbital on the n^{th} molecule. It is defined by[16]:

$$K_n^i\, \phi_m^r(1) = e^2 \int \frac{\phi_n^i(2)\, \phi_m^r(2)}{r_{12}}\, d\tau_2\, \phi_n^i(1) \qquad (3.26)$$

To calculate the transfer integrals in the weak-coupling limit of vibronic interaction, eqs.(3.5) and (3.25) are used in eq.(3.13). This gives:

$$e_\ell = \langle \phi_0^k(\vec{r}) \left| V_\ell(\vec{r} - \vec{r}_\ell) \right| \phi_\ell^k(\vec{r} - \vec{r}_\ell) \rangle \left| \langle \chi' | \chi^\circ \rangle \right|^2 \qquad (3.27)$$

where χ' represents the vibrational wavefunction of the positive or negative ion, and χ° that of the neutral molecule. Substituting from eq.(3.25) into eq.(3.27) gives:

$$e_\ell = \left| \langle \chi' | \chi^\circ \rangle \right|^2 \langle \phi^k(\vec{r} - \vec{r}_\ell) \left| \left(V_{GMS} - \sum_{i=0}^{a} K_\ell^i \right) \right| \phi^k(\vec{r}) \rangle$$

$$= \left|\langle \chi' | \chi^{\circ} \rangle\right|^2 \left\{ \langle \phi^k(\vec{r} - \vec{r}_\ell) \left| V_{GMS} \right| \phi^k(\vec{r}) \rangle - \sum_{i=0}^{a} \langle \phi^k(\vec{r} - \vec{r}_\ell) \left| K_\ell^i \right| \phi^k(\vec{r}) \rangle \right\} \qquad (3.28)$$

The first term in brackets is the intermolecular resonance integral, while the second term represents the exchange interaction. Writting it in terms of hybrid integrals gives:

$$\sum_{i=0}^{a} \langle \phi^k(\vec{r} - \vec{r}_\ell) \left| K_\ell^i \right| \phi^k(\vec{r}) \rangle =$$

$$\sum_{i=0}^{a} \sum_{\alpha,\beta,\gamma,\delta} C_{\ell,\alpha}^{k} \, C_{0,\beta}^{k} \, C_{\ell,\gamma}^{i} \, C_{\ell,\delta}^{i} \langle u_\alpha^\ell(1) \, u_\gamma^\ell(2) \left| \frac{1}{r_{12}} \right| u_\delta^\ell(1) \, u_\beta^{\circ}(2) \rangle \qquad (3.29)$$

where α, γ, δ number the atoms of molecule ℓ and β the atoms of the reference molecule 0.

4. Numerical Calculations of the Transfer Integrals

The transfer integrals given by eq.(3.28) can be symbolically written as:

$$e_\ell = \left(I.R.S. - I.E. \right) . F \qquad (3.30)$$

where $F = \left|\langle \chi' | \chi^{\circ} \rangle\right|^2$ is the vibrational overlap factor.

$I.R.S. = \langle \phi^k(\vec{r} - \vec{r}_\ell) \left| V_{GMS} \right| \phi^k(\vec{r}) \rangle$ is the resonance integral,

and $I.E. = \sum_{i=0}^{a} \langle \phi^k(\vec{r} - \vec{r}_\ell) \left| K_\ell^i \right| \phi^k(\vec{r}) \rangle$ is the exchange integral

4a. Evaluation of the Resonance Integrals

The two-center integrals of eq.(3.24) were expanded as follows[5]:

$$\int u_i(\vec{r}_i) \, V_i(\vec{r}_i) \, u_j(\vec{r}_j) =$$

$$-\frac{1}{\pi} \frac{(\hat{n}_i \cdot \vec{R}_{ij})(\hat{n}_j \cdot \vec{R}_{ij})}{R_{ij}^2} S_{ij} + \frac{1}{2\pi} \left[(\hat{n}_i \cdot \hat{n}_j) - \frac{(\hat{n}_i \cdot \vec{R}_{ij})(\hat{n}_j \cdot \vec{R}_{ij})}{R_{ij}^2} \right] C_{ij} \qquad (3.31)$$

where $\hat{n}_i$ and $\hat{n}_j$ are the unit vectors defining the direction of orbitals u_i and u_j, $\vec{R}_{ij}$ is the vector from atom i to atom j, and

$$S_{ij} = \int r_i r_j \cos\gamma_i \cos\gamma_j V_i \left[\sum_\ell a_\ell \alpha_\ell^{5/2} \exp(-\alpha_\ell r_i)\right] \times \left[\sum_m a_m \alpha_m^{5/2} \exp(-\alpha_m r_j)\right] d\tau$$

$$C_{ij} = \int r_i r_j \sin\gamma_i \sin\gamma_j V_i \left[\sum_\ell a_\ell \alpha_\ell^{5/2} \exp(-\alpha_\ell r_i)\right] \times \left[\sum_m a_m \alpha_m^{5/2} \exp(-\alpha_m r_j)\right] d\tau \qquad (3.32)$$

where γ_i and γ_j are the angles $\vec{r}_i$ and $\vec{r}_j$ make with $\vec{R}_{ij}$.

Analytical expressions for S_{ij} and C_{ij} were obtained by Delacote[19] and used in this work. All integrals involving coordinates of atoms closer than 10 Å were included in the calculation of the two-center integrals. The results at various pressures are given in table 3.3 for both the electron and hole bands.

None of the above simplifications were possible with the three-center integrals. A computer program was developped to calculate them with a three-dimensional Gaussian integration[20,21] routine using 8000 points distributed over the volume of a sphere of radius $2R_{ij}$. The coefficients of the Gaussian expansion were obtained from Stroud and Secrest[21]. Because of the large number of computations involved, only those integrals in which the potential and wavefunction on the same molecule were on near-neighbor atoms were performed, and of them, only those where the distance between the two wavefunctions was less than 6.5 Å.

The intermolecular resonance integrals were then obtained by adding the two-and three-center contributions. The results for both bands and at various pressures are given in table 3.4. By comparing tables 3.3 and 3.4, it can be seen that the inclusion of the three-center integrals increases the resonance integrals by approximately 15-25%.

4b. Evaluation of the Exchange Integrals

Silbey et al[6] obtained an expression for the two-center exchange integrals by letting $\alpha = \gamma = \delta$ in eq.(3.29)

$$I.E. = \sum_{i=0}^{a} \sum_{\alpha,\beta} C_{\ell,\alpha}^{k} \left(C_{\ell,\alpha}^{i}\right)^2 C_{o,\beta}^{k} \left\langle u_\alpha^\ell(1)\, u_\alpha^\ell(2) \left| \frac{1}{r_{12}} \right| u_\alpha^\ell(1)\, u_\beta^o(2) \right\rangle$$

$$= \frac{1}{2} \sum_{\alpha,\beta} C^{k}_{l,\alpha} C^{k}_{o,\beta} \langle u^{l}_{\alpha}(1) u^{l}_{\alpha}(2) \mid u^{l}_{\alpha}(1) u^{o}_{\beta}(2) \rangle \qquad (3.33)$$

Tiberghien and Delacote[22] have expanded the hybrid integrals of eq.(3.33) in terms of atomic hybrid integrals:

$$\begin{aligned} \langle u_\alpha(1)u_\alpha(2) \mid u_\alpha(1)u_\beta(2) \rangle &= A^3D(\langle P_+P_+|P_+P_+\rangle + 1/2\langle P_+P_-|P_+P_-\rangle) \\ &+ AC^2D(\langle P_zP_z|P_+P_+\rangle + 2\langle P_zP_+|P_zP_+\rangle) \\ &+ A^2CF(\langle P_+P_+|P_zP_z\rangle + 2\langle P_zP_+|P_-P_z\rangle) \\ &+ C^3F\langle P_zP_z|P_zP_z\rangle \end{aligned} \qquad (3.34)$$

with the convention $\langle P_1 P_2 | P_3 P_4 \rangle = \int P^{1}_{\alpha}(1)\, P^{2*}_{\alpha}(1)\, \frac{1}{r_{12}}\, P^{3*}_{\alpha}(2)\, P^{4}_{\beta}(2)$

A,C,D,E and F are coefficients depending upon the relative positions of atoms α and β, as well as the relative orientations of their respective molecules.

The various atomic hybrid integrals given in eq.(3.34) have already been calculated by Silbey[23]. In the present work it was found that their values could be closely fitted to an exponential function of the distance between atoms α and β.

The exchange integrals were then calculated at various pressures and for both electron and hole bands. The results are given in table 3.5 . By comparing tables 3.4 and 3.5, it can be seen that the inclusion of the exchange effects,drastically changes (approximately 2 to 3 times) the values of the transfer integrals.

4c.Evaluation of the Vibrational Overlap Integral

The method used is the one given by McCoy and Ross[24] who were able to estimate the vibrational overlaps between the various electronic states of the aromatic hydrocarbons, from the spectra accompagnying such electronic transitions. Choi et al[25] showed that the application of the McCoy-Ross procedure to the computation of the vibrational overlap between states of the neutral molecule and the corresponding ions gives:

$$\langle \chi^{oo}_{i} | \chi^{\pm n}_{j} \rangle = \frac{1}{(n!)^{1/2}} \left(\delta_{\omega\epsilon} / \sqrt{2} \right)^{n} \exp\left(- \delta^{2}_{\omega\epsilon} / 4 \right) \qquad (3.35)$$

Table 3.3 - Two-center intermolecular resonance integrals in units of 10^{-4} ev.

Pressure (Kbars) / Molecule #	Atm.	1.0	2.0	3.0	4.0	5.0	6.0
			Hole				
2	-0.19	-0.33	-0.48	-0.64	-0.83	-1.04	-1.27
3	-102.57	-106.67	-110.94	-115.37	-119.98	-124.78	-129.77
4	0.41	0.44	0.46	0.49	0.51	0.54	0.56
5	0.29	0.29	0.29	0.30	0.30	0.31	0.33
6	7.65	8.50	9.45	10.49	11.64	12.92	14.33
7	0.31	0.34	0.36	0.39	0.43	0.46	0.50
8	0.06	0.06	0.06	0.06	0.07	0.08	0.08
9	26.60	29.07	31.71	34.54	37.57	40.80	44.26
10	-31.10	-33.37	-35.76	-38.28	-40.93	-43.72	-46.65
11	-0.03	-0.03	-0.03	-0.03	-0.03	-0.03	-0.03
12	0.00	0.00	0.00	0.00	0.00	0.00	0.00
13	0.00	0.00	0.00	0.00	0.00	0.00	0.00
14	0.04	0.04	0.04	0.05	0.05	0.06	0.06
			Electron				
2	-4.48	-5.06	-5.68	-6.35	-7.05	-7.79	-8.59
3	25.67	26.96	28.30	29.71	31.19	32.74	34.36
4	0.07	0.07	0.07	0.07	0.08	0.08	0.09
5	-0.05	-0.05	-0.04	-0.06	-0.08	-0.10	-0.12
6	1.63	1.87	2.15	2.46	2.81	3.21	3.67
7	-0.07	-0.08	-0.08	-0.09	-0.09	-0.09	-0.10
8	-0.03	-0.04	-0.04	-0.04	-0.04	-0.04	-0.04
9	-55.50	-57.25	-59.03	-60.84	-62.66	-64.51	-66.37
10	-2.52	-3.05	-3.63	-4.27	-4.97	-5.73	-6.57
11	-0.03	-0.03	-0.03	-0.03	-0.04	-0.04	-0.04
12	0.00	0.00	0.00	0.00	0.00	0.00	0.00
13	0.00	0.00	0.00	0.00	0.00	0.00	0.00
14	0.01	0.02	0.02	0.02	0.02	0.02	0.02

Table 3.4 - Intermolecular resonance integrals (two-and three-center) in units of 10^{-4} ev.

Pressure (Kbars) / Molecule #	Atm.	1.0	2.0	3.0	4.0	5.0	6.0
			Hole				
2	-0.33	-0.46	-0.59	-0.73	-0.89	-1.07	-1.29
3	-127.01	-132.03	-137.25	-142.68	-148.33	-154.21	-160.31
4	0.41	0.44	0.46	0.49	0.51	0.54	0.56
5	0.29	0.29	0.29	0.30	0.30	0.31	0.33
6	10.54	11.71	12.33	13.70	15.20	16.60	18.41
7	0.31	0.34	0.36	0.39	0.43	0.46	0.50
8	0.06	0.06	0.06	0.06	0.07	0.08	0.08
9	31.85	34.95	38.24	41.77	45.55	49.60	53.95
10	-39.25	-42.24	-45.38	-48.63	-51.98	-55.43	-59.07
11	-0.03	-0.03	-0.03	-0.03	-0.03	-0.03	-0.03
12	0.00	0.00	0.00	0.00	0.00	0.00	0.00
13	0.00	0.00	0.00	0.00	0.00	0.00	0.00
14	0.04	0.04	0.04	0.05	0.05	0.06	0.06
			Electron				
2	-4.97	-5.63	-6.34	-7.10	-7.91	-8.78	-9.69
3	28.33	29.72	31.16	32.67	34.25	35.91	37.67
4	0.07	0.07	0.07	0.07	0.08	0.08	0.09
5	-0.05	-0.05	-0.04	-0.06	-0.08	-0.10	-0.12
6	1.62	1.87	2.01	2.33	2.68	3.21	3.68
7	-0.07	-0.08	-0.08	-0.09	-0.09	-0.09	-0.10
8	-0.03	-0.04	-0.04	-0.04	-0.04	-0.04	-0.04
9	-56.91	-58.77	-60.63	-62.51	-64.41	-66.34	-68.28
10	-2.43	-3.16	-3.93	-4.71	-5.49	-6.35	-7.22
11	-0.03	-0.03	-0.03	-0.03	-0.04	-0.04	-0.04
12	0.00	0.00	0.00	0.00	0.00	0.00	0.00
13	0.00	0.00	0.00	0.00	0.00	0.00	0.00
14	0.01	0.02	0.02	0.02	0.02	0.02	0.02

Table 3.5 - Intermolecular exchange integrals in units of 10^{-4} ev.

Pressure (Kbars) / Molecule #	Atm.	1.0	2.0	3.0	4.0	5.0	6.0
			Hole				
2	-0.41	-0.00	0.45	0.96	1.52	2.15	2.83
3	308.95	318.83	329.01	339.50	350.31	361.45	372.93
4	-2.17	-2.28	-2.40	-2.52	-2.65	-2.79	-2.93
5	-1.39	-1.46	-1.52	-1.59	-1.67	-1.74	-1.82
6	-36.20	-39.85	-43.83	-48.18	-52.92	-58.09	-63.73
7	-1.69	-1.82	-1.96	-2.11	-2.28	-2.45	-2.64
8	-0.28	-0.30	-0.31	-0.32	-0.34	-0.35	-0.36
9	-118.94	-127.15	-135.81	-144.92	-154.52	-164.62	-175.26
10	108.27	114.49	120.93	127.56	134.39	141.41	148.59
11	0.12	0.13	0.14	0.15	0.15	0.16	0.17
12	0.00	0.00	0.00	0.00	0.00	0.00	0.00
13	0.00	0.00	0.00	0.00	0.00	0.00	0.00
14	-0.23	-0.24	-0.25	-0.27	-0.28	-0.30	-0.31
			Electron				
2	8.74	10.28	11.91	13.64	15.46	17.38	19.41
3	-64.12	-66.72	-69.41	-72.20	-75.10	-78.11	-81.22
4	-0.36	-0.38	-0.40	-0.42	-0.45	-0.47	-0.50
5	0.29	0.33	0.38	0.44	0.50	0.57	0.65
6	-7.43	-8.42	-9.52	-10.76	-12.15	-13.71	-15.46
7	0.32	0.35	0.39	0.42	0.46	0.50	0.55
8	0.16	0.17	0.18	0.18	0.19	0.20	0.21
9	132.17	134.64	137.06	139.42	141.72	143.94	146.08
10	7.26	8.66	10.17	11.80	13.54	15.41	17.41
11	0.17	0.17	0.18	0.19	0.20	0.21	0.22
12	0.00	0.00	0.00	0.00	0.00	0.00	0.00
13	0.00	0.00	0.00	0.00	0.00	0.00	0.00
14	-0.07	-0.07	-0.07	-0.08	-0.08	-0.09	-0.10

where χ^{oo} represents the zeroth vibrational state of the ground state of the neutral molecule, n the vibrational quantum number of the ion, and χ^{+n} its vibrational state. The parameter δ_{we} is given by:

$$\delta_{we} = 158.9 \sqrt{2} (k/\nu)^{\frac{1}{2}} Z \qquad (3.36)$$

where k is the force constant corresponding to the vibrational states, and ν their frequency. Z is a factor that characterizes the change in molecular shape; it was given by McCoy and Ross to be 0.069 Å for naphthalene. They also gave $k = 7.5$ mdyn/Å , and $\nu = 1400$ cm^{-1}. The vibrational overlap integrals were then calculated by substituting these values into equation (3.35). The results are given in table 3.6 .

As a result of the vibrational overlap, every electronic band now becomes a series of vibronic bands, each characterized by a vibrational wavefunction. However, since the electronic bandwidths (see section 4d) are much smaller than the vibrational quantum of energy (~ 0.2 ev), and since the energy spacing to the first vibrationally excited band is much greater than kT, only the lowest vibrational band need be considered. The calculated transfer integrals will then include the overlap between the ground state vibrational wavefunctions of the ion and the neutral molecule. This corresponds to $n = 0$, in table 3.6, and it can be seen that the value of the vibrational overlap factor is 0.525 . This value is larger than the value of 0.333 for the Franck-Condon factor of naphthalene, obtained by Siebrand[26]. The TIs obtained by combining all the factors of eq.(3.30) are displayed in table 3.7 .

4d.Pressure Dependence of the Band Structure

Finally, the pressure dependence of the band structure was calculated from eq.(3.15). The excess electron and hole bandwidths were determined by using four different sets of values for the transfer integrals. Tables 3.8 and 3.9 give the values obtained when only the resonance integrals are involved, while table 3.10 corresponds to the inclusion of the exchange integrals. Table 3.11 gives the bandwidth when the transfer integrals given by eq.(3.30) are used.

It can be seen that when exchange interactions are taken into consideration, all bands are broadened, while the effect of the vibrational overlap integral is to make them narrower. Plots of the various results

obtained in tables 3.8 , 3.9 , 3.10 and 3.11 are shown in figs. 3.3(a,b) , 3.4(a,b) and 3.5(a,b) , where a refers to holes and b to electrons. It is interesting to note that all bands increase in width with pressure.

Table 3.6 - Vibrational overlap integrals of naphthalene.

n	$\langle \chi^{oo} \mid \chi^{+n} \rangle$	$\lvert \langle \chi^{oo} \mid \chi^{+n} \rangle \rvert^2$
0	0.7247	0.52519
1	-0.5816	0.33822
2	0.3300	0.10894
3	-0.1529	0.02338
4	0.0614	0.00376
5	-0.0220	0.00048

Table 3.7 - Intermolecular transfer integrals, (IRS - IE).F , in units of 10^{-4} ev.

Pressure (Kbars) / Molecule #	Atm.	1.0	2.0	3.0	4.0	5.0	6.0
			Hole				
2	0.04	-0.24	-0.55	-0.89	-1.27	-1.69	-2.16
3	-228.96	-236.79	-244.88	-253.24	-261.88	-270.82	-280.05
4	1.36	1.43	1.50	1.58	1.66	1.75	1.83
5	0.88	0.92	0.95	0.99	1.03	1.08	1.12
6	24.55	27.08	29.50	32.50	35.78	39.23	43.14
7	1.05	1.13	1.22	1.32	1.42	1.53	1.65
8	0.18	0.19	0.19	0.20	0.21	0.22	0.23
9	79.19	85.13	91.41	98.05	105.08	112.51	120.38
10	-77.47	-82.31	-87.35	-92.53	-97.88	-103.38	-109.06
11	-0.08	-0.08	-0.09	-0.09	-0.10	-0.10	-0.11
12	0.00	0.00	0.00	0.00	0.00	0.00	0.00
13	0.00	0.00	0.00	0.00	0.00	0.00	0.00
14	0.14	0.15	0.16	0.17	0.18	0.19	0.20
			Electron				
2	-7.20	-8.36	-9.59	-10.89	-12.28	-13.74	-15.28
3	48.56	50.65	52.82	55.08	57.43	59.88	62.44
4	0.22	0.24	0.25	0.26	0.28	0.29	0.31
5	-0.18	-0.20	-0.22	-0.26	-0.31	-0.35	-0.40
6	4.75	5.40	6.06	6.87	7.79	8.89	10.05
7	-0.21	-0.23	-0.25	-0.27	-0.29	-0.31	-0.34
8	-0.10	-0.11	-0.11	-0.12	-0.12	-0.12	-0.13
9	-99.30	-101.58	-103.82	-106.05	-108.26	-110.44	-112.58
10	-5.09	-6.21	-7.41	-8.67	-10.00	-11.43	-12.93
11	-0.10	-0.11	-0.11	-0.12	-0.12	-0.13	-0.14
12	0.00	0.00	0.00	0.00	0.00	0.00	0.00
13	0.00	0.00	0.00	0.00	0.00	0.00	0.00
14	0.04	0.05	0.05	0.05	0.05	0.06	0.06

Table 3.8 - Bandwidths (in 10^{-4} ev) corresponding to the two-center intermolecular resonance integrals.

Direction \ Pressure (Kbars)	Atm.	1.0	2.0	3.0	4.0	5.0	6.0
				Hole			
$\vec{a}$ lower	19.07	23.10	27.74	33.10	39.24	46.25	54.18
$\vec{a}$ upper	52.65	55.46	58.47	61.68	65.07	68.81	72.71
$\vec{b}$ lower	422.11	437.30	452.66	468.93	484.89	502.18	519.51
$\vec{b}$ upper	386.40	403.20	420.55	439.31	458.31	479.11	500.67
$\vec{c}$ lower	282.62	303.82	326.34	350.26	375.56	402.42	430.79
$\vec{c}$ upper	215.42	230.53	246.26	262.67	279.79	297.59	316.10
				Electron			
$\vec{a}$ lower	226.62	234.84	243.23	251.92	260.67	269.61	278.76
$\vec{a}$ upper	237.65	247.65	258.12	269.04	280.46	292.48	304.92
$\vec{b}$ lower	129.76	133.74	137.87	142.07	146.20	150.42	154.80
$\vec{b}$ upper	334.52	348.74	363.49	378.89	394.93	411.67	428.89
$\vec{c}$ lower	31.49	37.09	43.13	49.66	56.66	64.13	72.16
$\vec{c}$ upper	9.29	12.14	15.40	19.12	23.37	28.21	33.60

Following the notation given by Katz et al[5], "lower" and "upper" correspond to the two energy bands $E_{\pm}(\vec{K})$.

Table 3.9 - Bandwidths (in 10^{-4} ev) corresponding to the intermolecular resonance integrals (two-and three-center).

Pressure (Kbars) / Direction	Atm.	1.0	2.0	3.0	4.0	5.0	6.0
				Hole			
$\vec{a}$-l lower	21.42	26.20	29.15	35.38	42.83	50.58	60.53
$\vec{a}$-l upper	75.80	80.26	82.37	86.96	91.59	95.13	99.95
$\vec{b}$-l lower	531.31	550.46	570.22	590.61	610.77	631.42	652.43
$\vec{b}$-l upper	472.66	492.69	513.62	536.22	559.79	585.22	611.89
$\vec{c}$-l lower	358.83	387.10	414.40	445.51	477.96	510.64	546.40
$\vec{c}$-l upper	269.62	289.17	312.12	333.02	354.19	376.73	399.22
				Electron			
$\vec{a}$-l lower	231.94	241.37	251.40	260.90	270.28	279.39	288.96
$\vec{a}$-l upper	242.85	254.14	265.22	276.97	289.04	302.24	315.22
$\vec{b}$-l lower	124.37	129.21	134.06	138.69	143.06	147.51	151.80
$\vec{b}$-l upper	350.41	366.30	382.56	399.18	416.27	434.11	452.37
$\vec{c}$-l lower	32.76	40.25	48.75	56.75	64.82	72.97	81.75
$\vec{c}$-l upper	6.48	10.70	14.71	19.13	23.58	29.17	34.45

Following the notation given by Katz et al[5], "lower" and "upper" correspond to the two energy bands $E_{\pm}(\vec{K})$.

Table 3.10 - Bandwidths (in 10^{-4} ev) corresponding to the intermolecular transfer integrals, (IRS - IE).

Pressure (Kbars) / Direction	Atm.	1.0	2.0	3.0	4.0	5.0	6.0
				Hole			
$\vec{a}\text{-}\vert_{lower}$	226.07	255.40	284.80	320.76	360.63	403.93	452.43
$\vec{a}\text{-}\vert_{upper}$	198.97	211.74	223.12	237.27	252.34	267.13	284.19
$\vec{b}\text{-}\vert_{lower}$	1690.56	1739.66	1789.41	1839.11	1889.11	1939.77	1990.33
$\vec{b}\text{-}\vert_{upper}$	1717.88	1783.85	1852.05	1924.10	1999.60	2079.73	2162.94
$\vec{c}\text{-}\vert_{lower}$	1391.93	1483.88	1578.07	1678.91	1784.05	1891.79	2006.68
$\vec{c}\text{-}\vert_{upper}$	970.51	1025.85	1085.38	1143.08	1201.28	1260.08	1319.75
				Electron			
$\vec{a}\text{-}\vert_{lower}$	765.42	786.81	808.73	829.67	850.28	870.45	890.39
$\vec{a}\text{-}\vert_{upper}$	825.80	855.89	886.71	918.62	951.82	987.15	1023.03
$\vec{b}\text{-}\vert_{lower}$	427.08	437.09	446.99	456.43	465.49	474.97	483.55
$\vec{b}\text{-}\vert_{upper}$	1164.13	1205.61	1248.46	1291.86	1336.62	1382.62	1429.87
$\vec{c}\text{-}\vert_{lower}$	95.84	116.73	139.35	162.30	185.92	210.49	236.26
$\vec{c}\text{-}\vert_{upper}$	62.28	75.64	89.83	105.46	122.36	141.67	162.05

Following the notation given by Katz et al[5], "lower" and "upper" correspond to the two energy bands $E_{\pm}(\vec{K})$.

Table 3.11 - Bandwidths (in 10^{-4} ev) corresponding to the intermolecular transfer integrals, (IRS - IE).F .

Pressure (Kbars) / Direction	Atm.	1.0	2.0	3.0	4.0	5.0	6.0
				Hole			
$\vec{a}_{lower}$	118.73	134.13	149.57	168.46	189.40	212.14	237.61
$\vec{a}_{upper}$	104.50	111.20	117.18	124.61	132.53	140.29	149.25
$\vec{b}_{lower}$	887.87	913.65	939.78	965.88	992.14	1018.75	1045.30
$\vec{b}_{upper}$	902.21	936.86	972.68	1010.52	1050.17	1092.25	1135.95
$\vec{c}_{lower}$	731.03	779.32	828.79	881.75	936.97	993.55	1053.89
$\vec{c}_{upper}$	509.70	538.77	570.03	600.33	630.90	661.78	693.12
				Electron			
$\vec{a}_{lower}$	401.99	413.22	424.74	435.73	446.56	457.15	467.62
$\vec{a}_{upper}$	433.70	449.50	465.69	482.45	499.89	518.44	537.29
$\vec{b}_{lower}$	224.30	229.56	234.75	239.71	244.47	249.50	253.96
$\vec{b}_{upper}$	611.39	633.17	655.68	678.47	701.98	726.14	750.95
$\vec{c}_{lower}$	50.33	61.31	73.19	85.24	97.64	110.55	124.08
$\vec{c}_{upper}$	32.71	39.73	47.18	55.39	64.26	74.40	85.11

Following the notation given by Katz et al[5], "lower" and "upper" correspond to the two energy bands $E_{\pm}(\vec{K})$.

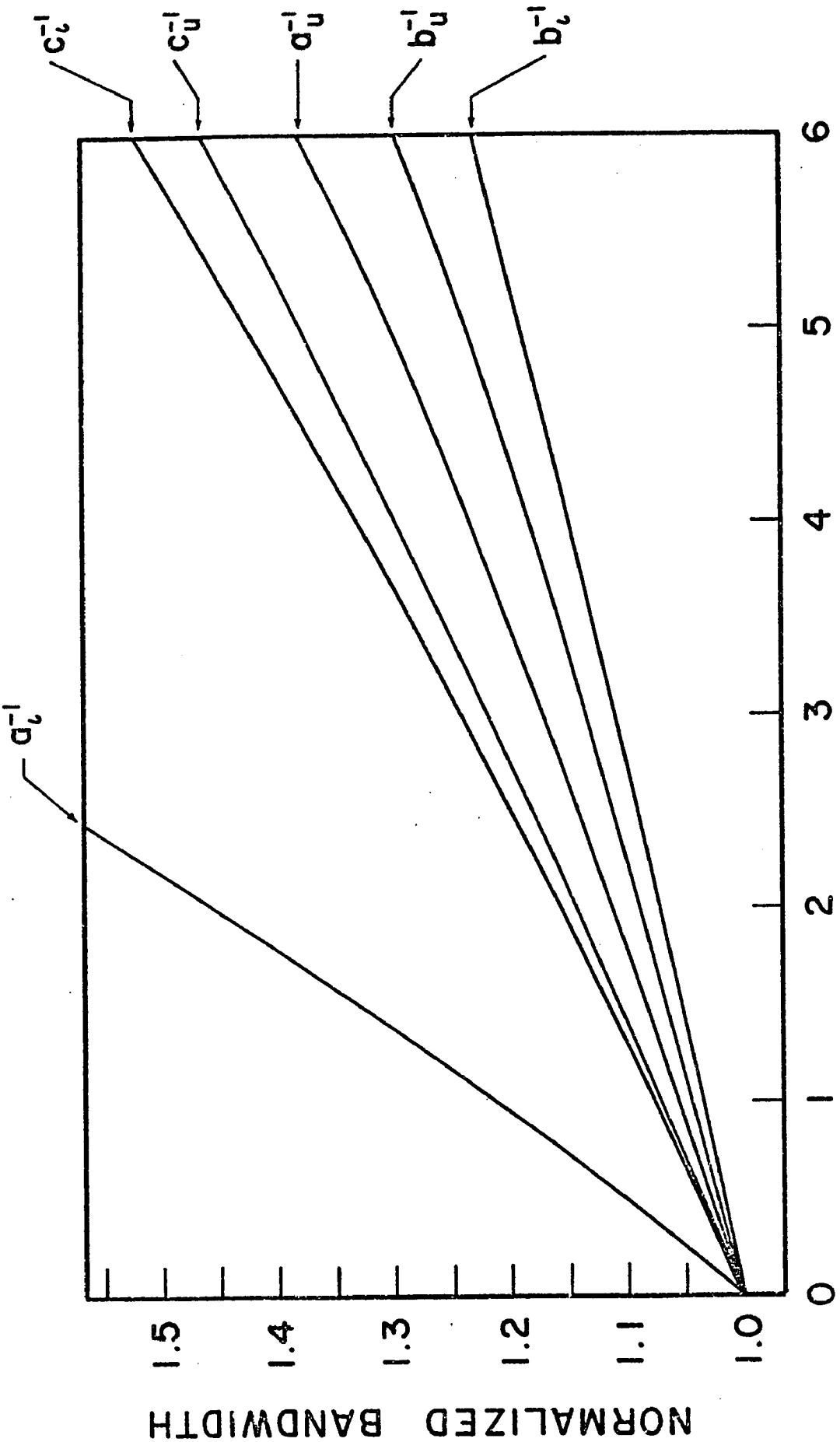

FIG. 3.3a

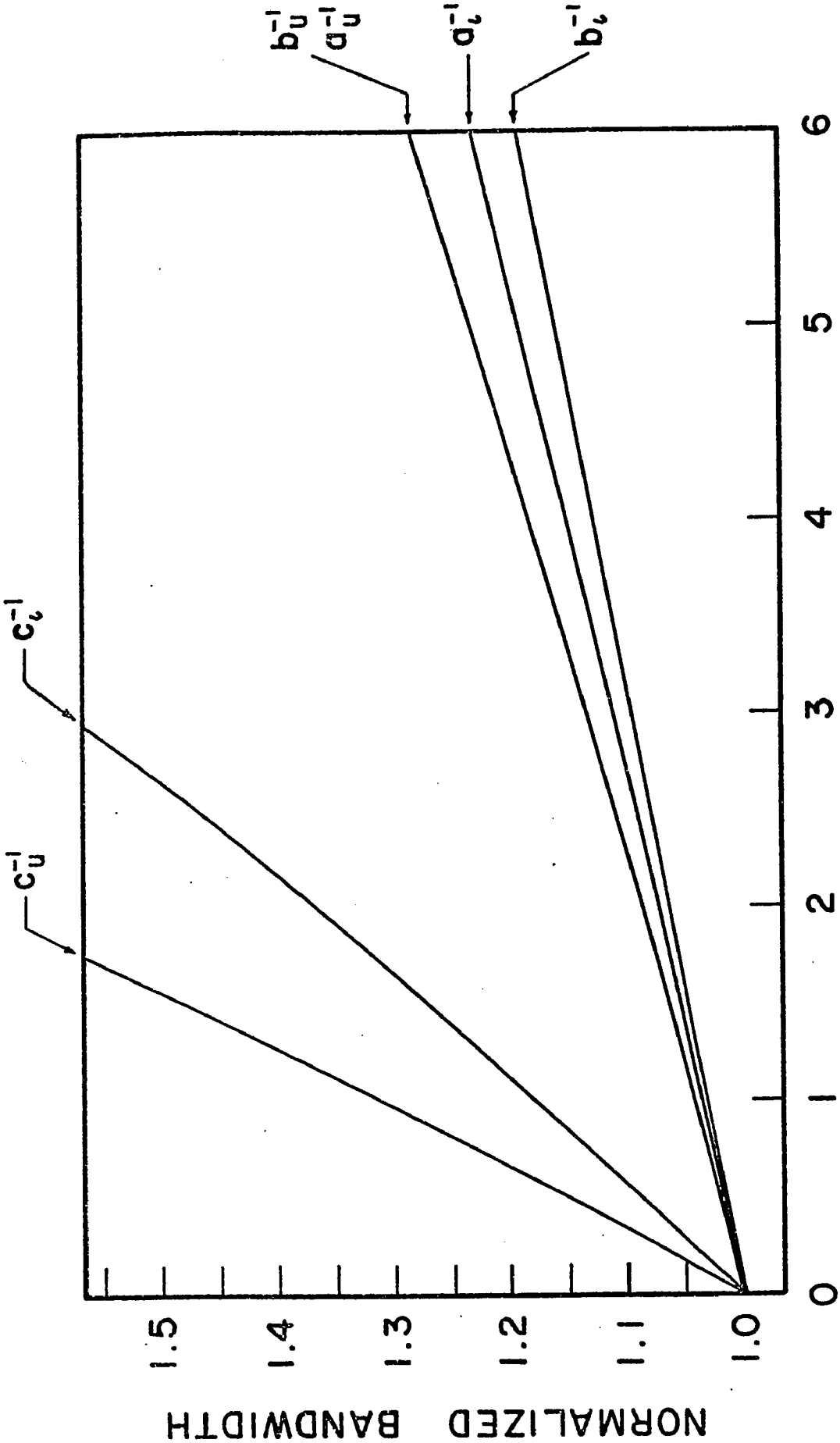

FIG. 3.3b

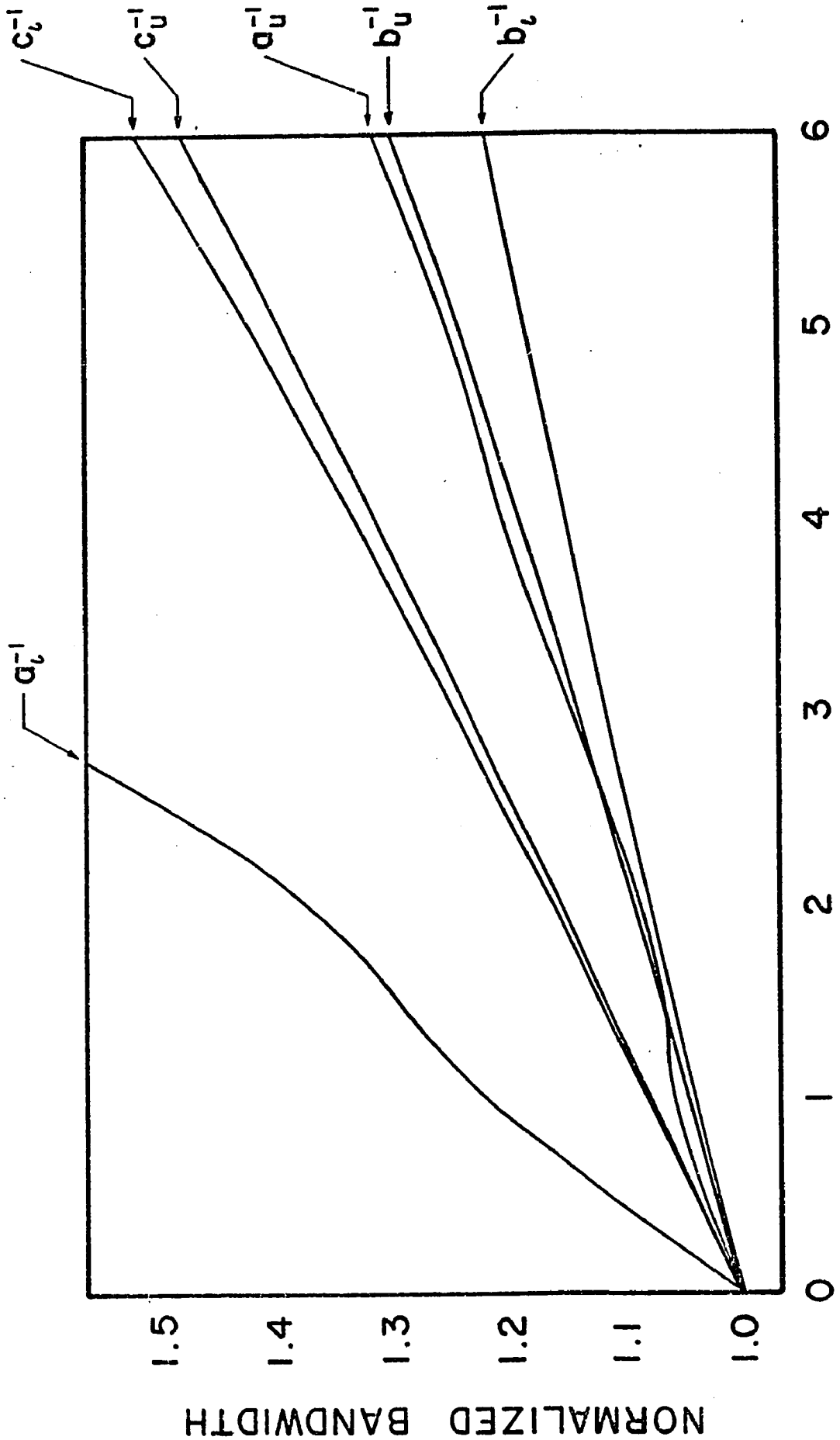

FIG. 3.4a

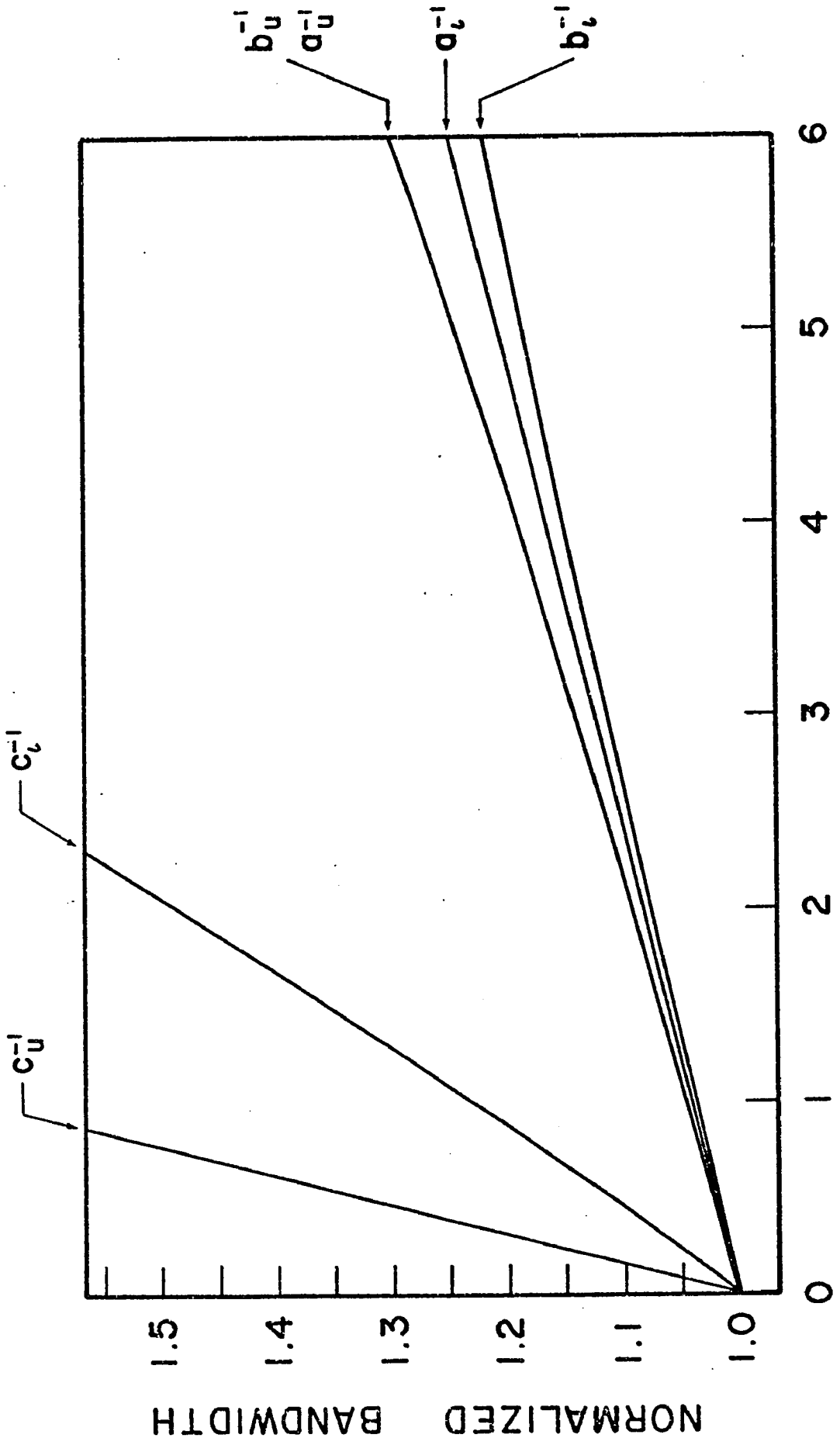

FIG. 3.4b

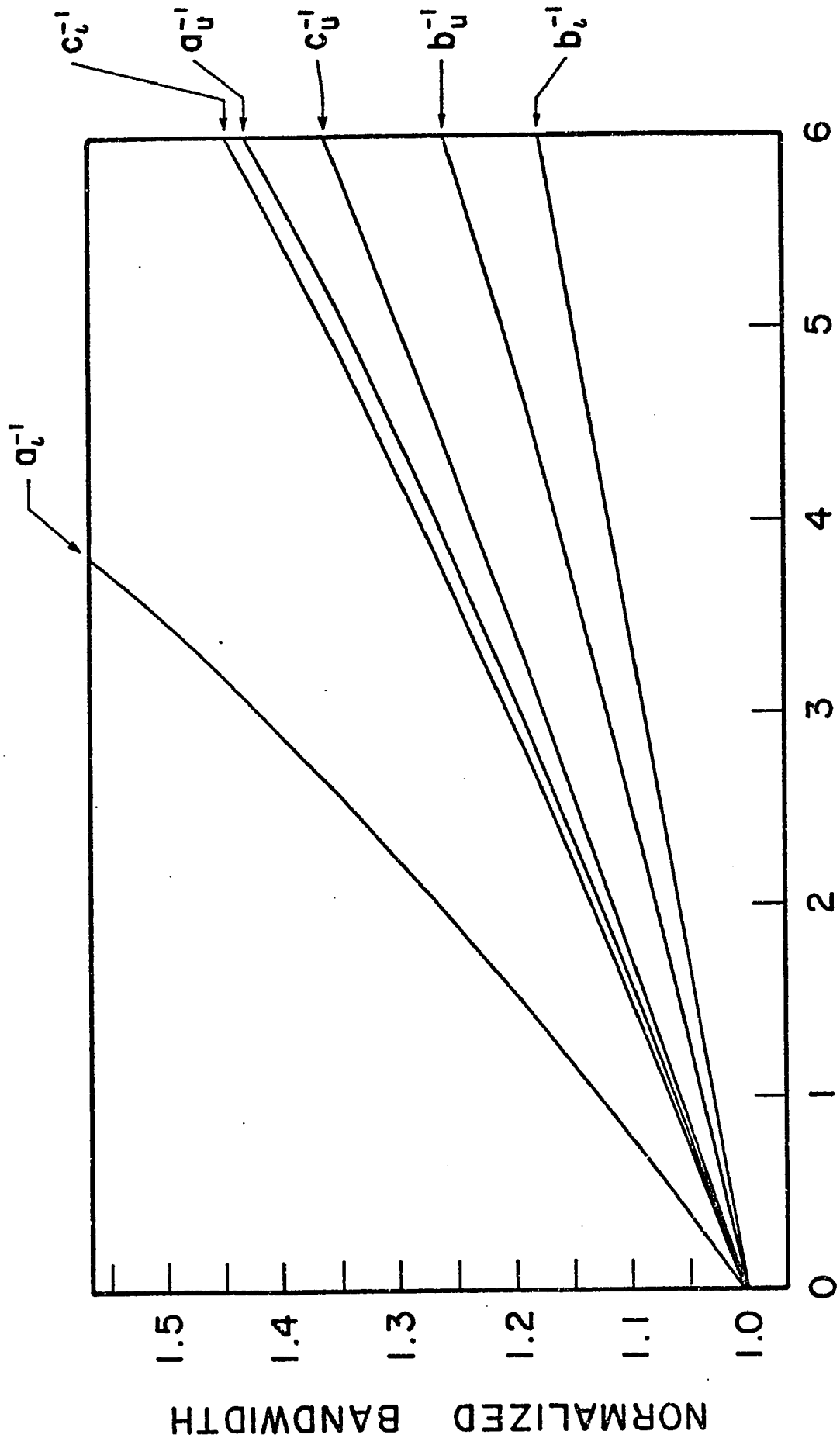

FIG. 3.5a

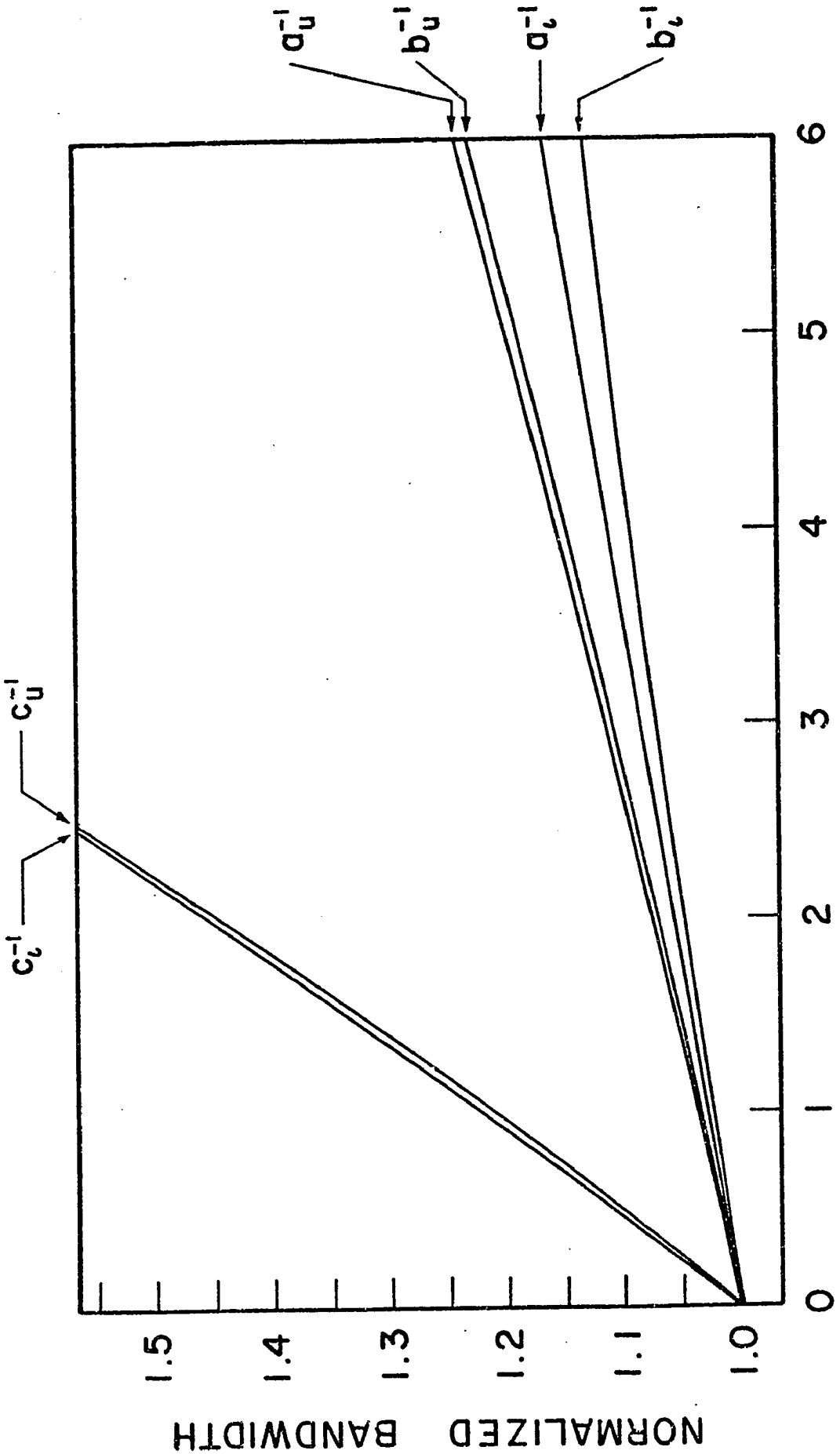

FIG. 3.5b

References - Chapter 3

1. M. Campos, Molec. Cryst. Liq. Cryst., 18, 105 (1972).

2. F. Seitz, Modern Theory of Solids, McGraw-Hill, Inc., New York, 1940.

3. O.H. Leblanc, Jr., J. Chem. Phys., 35, 1275 (1961); 36, 1082 (1962).

4. G.D. Thaxton, R.C. Jarnagin and M. Silver, J. Phys. Chem., 66, 2461 (1962).

5. J.L. Katz, S.A. Rice, S.I. Choi and J. Jortner, J. Chem. Phys., 39, 1683 (1963).

6. R. Silbey, J. Jortner, S.A. Rice and M.T. Vala, Jr., J. Chem. Phys., 42, 733 (1965); 43, 2925 (1965).

7. R.M. Glaeser and R.S. Berry, J. Chem. Phys., 44, 3797 (1966).

8. K. Tanaka and K. Niira, J. Phys. Soc. Japan, 24, 520 (1968).

9. P. Devaux, J. Chem. Phys., 52, 6436 (1970).

10. P. Balk, S. De Bruijn and G.J. Hoijtink, Recueil Trav. Chim. Pays Bas, 76, 860 (1957).

11. E. Huckel, Z. Physik, 76, 628 (1932).

12. J.C. Slater, Phys. Rev., 36, 57 (1930).

13. J.R. Hoyland, Ph.D. Thesis, Pennsylvania State University, 1961 ; J.R. Hoyland and L. Goodman, J. Chem. Phys., 36, 12 (1962).

14. E. Clementi, C.C.J. Roothaan and M. Yoshimine, Phys. Rev., 127, 1618 (1962).

15. D.W.J. Cruickshank, Acta Cryst., 10, 504 (1957).

16. L. Salem, The Molecular Orbital Theory of Conjugated Systems, W.A. Benjamin, Inc., New York, 1966.

17. J.A. Pople, Proc. Phys. Soc. (London), A68, 81 (1955).

18. M. Goeppert-Mayer and A.L. Sklar, J. Chem. Phys., 6, 645 (1938).

19. G. Delacote, Ph.D. Thesis, Universite de Paris, 1968.

20. A.H. Stroud, Mathematical Methods for Digital Computers, vol. 2, (eds. A. Ralston and H.S. Wilf), John Wiley, New York, 1967.

21. A.H. Stroud and D. Secrest, Gaussian Quadrature Formulas, Prentice-

Hall, Inc., Englewood, N.J., 1966.

22. A. Tiberghien and G. Delacote, J. Phys. (Paris), 31, 637 (1970).

23. R.J. Silbey, Ph.D. Thesis, 1965.

24. E.F. McCoy and I.G. Ross, Australian J. Chem., 4, 573 (1962).

25. S.I. Choi, J. Jortner, S.A. Rice and R. Silbey, J. Chem. Phys., 41, 3294 (1964).

26. W. Siebrand, J. Chem. Phys., 41, 3574 (1964).

Chapter Four

Calculation of the Pressure Dependence of the Hall and Drift Mobilities

1. Introduction

The existence of the Hall effect is of great use in the study of conventional semiconductors[1]: it gives the sign of the charge carriers as well as their concentration, when supplemented by conductivity measurements. It also allows an analysis of the various modes of charge transport. Organic semiconductors, however, have narrow bands[2,3,4] (also see previous chapter), and consequently their kinetic coefficients will show important quantitative differences from those appropriate to the usual wide-band case.

Leblanc[5] and Friedman[6] have calculated the expected behavior of (μ_H/μ_D) (μ_H and μ_D are the Hall and drift mobilities, respectively). For large bandwidths ($W \gg kT$), the conventional result $(\mu_H/\mu_D) \approx +1$ was obtained. For narrow bandwidths ($W \lesssim kT$), they found that both the value and the sign of this ratio could change (anomalous Hall effect). The positive sign of (μ_H/μ_D) in conventional semiconductors results from the respective curvatures of the conduction and valence bands near their band edges; where most of the carriers in the wide band lie; under standard sign conventions, this leads to a positive effective mass for both holes and electrons. When the bands are narrow and all states about equally populated, negative effective mass states near the zone boundary contribute to (μ_H/μ_D) as well. If the bands are also anisotropic, contributions associated with positive and negative effective masses can contribute unequally. The overall sign of (μ_H/μ_D) then depends on the detailed bandshape, of which Hall effect measurements should be a sensitive probe.

The calculation of transport coefficients from the details of a scattering mechanism requires that the statistical aspects of charge transport be considered. This was done by solving Boltzmann's equation[7,8]. Such a procedure does not take into consideration the anisotropy of the scattering, and thus yields only mobility ratios with an anisotropy resulting

only from the band structure. However, this will be adequate for the present work since only pressure variations of the mobility components are required in order to test the band model against the experimental results.

2. Elementary Theory of the Hall Effect

A simplified model for the Hall effect is first considered. The assumption is made that the material has no thermal carriers: the carriers are all injected carriers of one sign. Also, the crystal is assumed to be the dielectric of a parallel plate capacitor, where the space charge of the carriers is negligible compared to the charge on the plates of the capacitor. This can be achieved by creating electron-hole pairs very near to one electrode by photo-injection for example. Thus, the creation rate of the electrodes, not the space charge of the carriers, limits the photocurrent. Finally, all charge carriers are assumed to have the same drift velocity.

Fig. 4.1 shows the standard conditions for the Hall effect. Positive charge carriers are deflected in the negative y direction, while negative charge carriers are deflected in the positive y direction by the Lorentz force (v x B), (MKS units will be used throughout). In the case of positive charge carriers, an excess of holes builds up on the face V_2 until an electrostatic field E_H is established which just balances the Lorentz force, giving:

$$E_H = v_x B_z \tag{4.1}$$

where v_x is the average drift velocity of the charge carriers. The current density is given by:

$$J_x = n e v_x \tag{4.2}$$

where n is the density of positive charge carriers, and e is the charge. Thus, eq.(4.1) may be rewritten as:

$$E_H = \left(\frac{1}{n e}\right) J_x B_z \tag{4.3}$$

The Hall coefficient is usually defined by:

$$R_H = \frac{E_H}{J_x B_z} \tag{4.4}$$

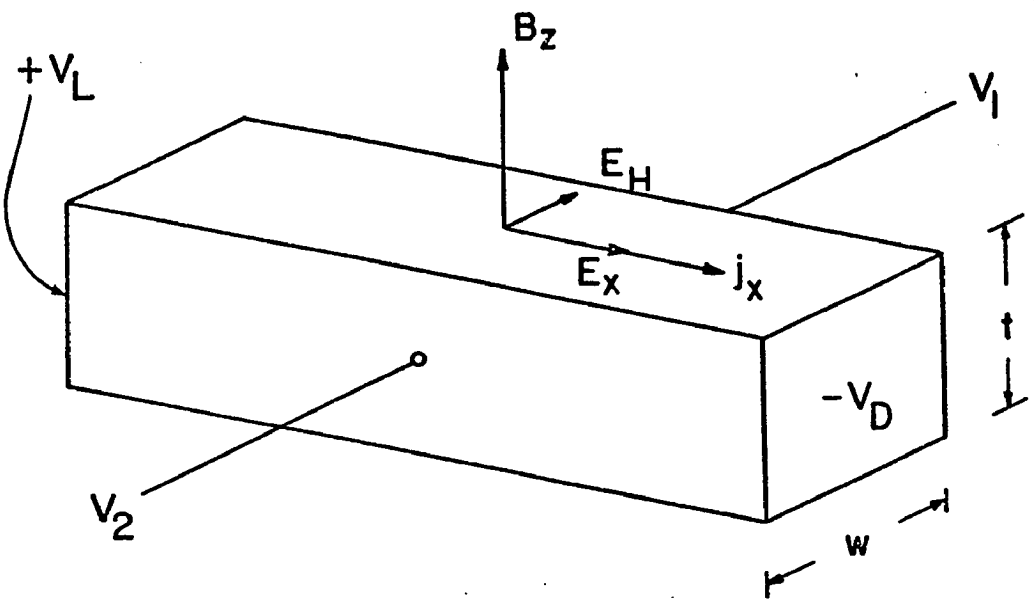

FIG. 4.1

Therefore, for the simple analysis of uniform drift velocity v_x , the Hall coefficient is inversely proportional to the concentration of charge carriers,

$$R_H = \frac{1}{n\,e} \tag{4.5}$$

The Hall mobility is defined by:

$$\mu_H \equiv R_H\,\sigma \tag{4.6}$$

where σ is the electrical conductivity of the material. This in turn is defined as:

$$\sigma \equiv n\,e\,\mu_D \tag{4.7}$$

where μ_D is the drift mobility. Combining eqs.(4.5), (4.6) and (4.7) gives:

$$\frac{\mu_H}{\mu_D} = 1 \tag{4.8}$$

Also $$J_x = \sigma\,E_x \tag{4.9}$$

Therefore, substituting eqs.(4.6) and (4.9) into eq.(4.4) gives:

$$E_H = \mu_H\,E_x\,B_z \tag{4.10}$$

But by definition $$E_H \equiv \frac{V_H}{w} \tag{4.11}$$

where w is the sample width, and V_H is the measured Hall voltage, equal to $(V_2 - V_1)$, V_1 and V_2 being the Hall voltages relative to ground. Combining eqs.(4.10) and (4.11) gives:

$$\mu_H = \frac{V_H}{w\,E_x\,B_z} \tag{4.12}$$

This now defines the Hall mobility.

3. General Transport Theory of the Hall Effect[8,9]

The calculation of transport coefficients from the band model has been formulated in terms of the Boltzmann equation

$$\frac{df}{dt} = \frac{\partial f}{\partial t} + \vec{v}\cdot\nabla_r f + \frac{1}{\hbar}\vec{F}\cdot\nabla_k f \tag{4.13}$$

where $f(\vec{k},\vec{r},t)drdk$ is the number of carriers in the volume element $d\vec{r}$ centered around $\vec{r}$, which, at time t, have wavevectors in the range $\vec{k}$ to $\vec{k}+d\vec{k}$. $\vec{F}$ is an externally applied force on the carriers, and $\vec{v}$ their velocity.

In thermal equilibrium and in the absence of applied fields, $f(\vec{k},\vec{r},t)$ becomes the Fermi-Dirac distribution function f_o

$$f_o = \left[\exp\ (\mathcal{E} - \mathcal{E}_F)/kT \quad + \ 1\right]^{-1} \tag{4.14}$$

no transport takes place, because the probabilities of occupation of the states with wavevectors $\vec{k}$ and $-\vec{k}$ are equal.

In the presence of external fields, and for a homogeneous material at constant temperature, the spatial variation of the distribution function vanishes, i.e.

$$\nabla_r f = 0 \tag{4.15}$$

Also, in the steady state

$$\frac{\partial f}{\partial t} = 0 \tag{4.16}$$

And if the total rate of change of f is due to collisions, then

$$\frac{df}{dt} = \left(\frac{\partial f}{\partial t}\right)_{collisions} \tag{4.17}$$

Substituting eqs.(4.15),(4.16),and (4.17) into eq.(4.13) gives for the Boltzmann equation

$$\left(\frac{\partial f}{\partial t}\right)_{collisions} = \frac{1}{\hbar}\vec{F}.\nabla_k f \tag{4.18}$$

At this point, the assumption is made that $\left(\frac{\partial f}{\partial t}\right)_{collisions}$ can be characterized by a collision relaxation time $\tau = \tau(\vec{k})$:

$$\left(\frac{\partial f}{\partial t}\right)_{collisions} = -\frac{(f - f_o)}{\tau} \tag{4.19}$$

Therefore, the Boltzmann equation becomes:

$$-\frac{(f - f_o)}{\tau} = \frac{1}{\hbar}\vec{F}.\nabla_k f \tag{4.20}$$

If the external force F is due to electric and magnetic fields, eq.(4.20) becomes:

$$-\frac{(f - f_o)}{\tau} = -\frac{e}{\hbar}\left(\vec{E} + \vec{v}\times\vec{B}\right).\nabla_k f \tag{4.21}$$

The Boltzmann transport equation can now be solved using a method developped by Jones and Zener[10]. The treatment consists in writting f as:

$$f = f_0 - \phi(\vec{k}) \frac{\partial f_0}{\partial \mathcal{E}} \tag{4.22}$$

where $\mathcal{E}$ is the energy of the state. Differentiation of both sides gives:

$$\nabla_k f = \nabla_k f_0 - \frac{\partial f_0}{\partial \mathcal{E}} \nabla_k \phi(\vec{k}) - \phi(\vec{k}) \nabla_k \left(\frac{\partial f_0}{\partial \mathcal{E}} \right) \tag{4.23}$$

but $$\nabla_k \mathcal{E} = \hbar \vec{v} \quad \text{and} \quad \nabla_k f_0 = \hbar \vec{v} \frac{\partial f_0}{\partial \mathcal{E}} \tag{4.24}$$

Substituting eq.(4.24) into eq.(4.23) gives:

$$\nabla_k f = \hbar \vec{v} \frac{\partial f_0}{\partial \mathcal{E}} - \phi(\vec{k}) \frac{\partial}{\partial \mathcal{E}} \left[\hbar \vec{v} \frac{\partial f_0}{\partial \mathcal{E}} \right] - \frac{\partial f_0}{\partial \mathcal{E}} \nabla_k \phi(\vec{k})$$

or $$\nabla_k f = \hbar \vec{v} \left[\frac{\partial f_0}{\partial \mathcal{E}} - \phi(\vec{k}) \frac{\partial^2 f_0}{\partial \mathcal{E}^2} \right] - \frac{\partial f_0}{\partial \mathcal{E}} \nabla_k \phi(\vec{k}) \tag{4.25}$$

Now since $\vec{v} \times \vec{v} = 0$, the last term in eq.(4.21) becomes:

$$-\frac{e}{\hbar} (\vec{v} \times \vec{B}) \cdot \nabla_k f = -\frac{e}{\hbar} \vec{B} \cdot (\nabla_k f \times \vec{v})$$

or $$-\frac{e}{\hbar} (\vec{v} \times \vec{B}) \cdot \nabla_k f = -\frac{e}{\hbar^2} \vec{B} \cdot \left[\frac{\partial f_0}{\partial \mathcal{E}} (\nabla_k \mathcal{E} \times \nabla_k \phi) \right] \tag{4.26}$$

If the magnetic field is chosen along the z-axis, eq.(4.26) becomes:

$$-\frac{e}{\hbar} (\vec{v} \times \vec{B}) \cdot \nabla_k f = -\frac{e}{\hbar^2} B_z \frac{\partial f_0}{\partial \mathcal{E}} \Omega_z \phi \tag{4.27}$$

where $$\vec{\Omega} \equiv \nabla_k \mathcal{E} \times \nabla_k \tag{4.28}$$

Now eqs.(4.22) and (4.27) are substituted into eq.(4.21) in order to obtain an expression for the unknown function $\phi = \phi(\vec{k})$. For an arbitrary direction of $\vec{B}$, this gives the linear first order equation:

$$\frac{\phi}{\tau} + \frac{e}{\hbar} \vec{E} \cdot \nabla_k \mathcal{E} + \frac{e}{\hbar^2} \vec{B} \cdot \vec{\Omega} \phi = 0 \tag{4.29}$$

where terms involving products of $\vec{E}$ and ϕ were neglected. This equation

was solved[10] by an iterative method to yield:

$$\phi(\vec{k}) = -\frac{e\mathcal{T}}{\hbar}\left\{\vec{E}\cdot\nabla_k\mathcal{E} - \left(\frac{e}{\hbar^2}\right)\vec{B}\cdot\vec{\Omega}(\mathcal{T}\vec{E}\cdot\nabla_k\mathcal{E}) + \left(\frac{e}{\hbar^2}\right)^2\vec{B}\cdot\vec{\Omega}\left[\mathcal{T}\vec{B}\cdot\vec{\Omega}(\mathcal{T}\vec{E}\cdot\nabla_k\mathcal{E})\right] + \cdots\cdots\right\} \tag{4.30}$$

The current density is given by:

$$\vec{J} = -\frac{e}{4\pi^3}\int(f - f_0)\vec{v}\,d^3k = \frac{e}{4\pi^3}\int\phi\frac{\partial f_0}{\partial\mathcal{E}}\vec{v}\,d^3k \tag{4.31}$$

$e > 0$ for electrons.

Since f_o is the Fermi-Dirac distribution function, it follows that:

$$-\frac{\partial f_0}{\partial\mathcal{E}} = f_0(1 - f_0)/kT \tag{4.32}$$

Furthermore, if the density of electrons in the conduction band is small enough that $f_o \ll 1$, i.e., if the system is non-degenerate so that it may be described by classical Boltzmann statistics, equation (4.32) reduces to:

$$-\left(\frac{\partial f_0}{\partial\mathcal{E}}\right) \approx \frac{f_0}{kT} \tag{4.33}$$

Substituting eq.(4.33) into eq.(4.31) gives:

$$\vec{J} = -\left(\frac{e}{4\pi^3}\right)\frac{1}{kT}\int\vec{v}\,\phi f_0\,d^3k \tag{4.34}$$

In order to calculate the drift mobility, $\vec{B}$ is set to zero. Eq.(4.30) then reduces to:

$$\phi(\vec{k}) = -\frac{e\mathcal{T}}{\hbar}\vec{E}\cdot\nabla_k\mathcal{E} = -e\mathcal{T}\vec{E}\cdot\vec{v} \tag{4.35}$$

Substituting this into eq.(4.31) for the current density gives:

$$\vec{J} = \frac{e^2}{4\pi^3}\frac{\vec{E}}{kT}\cdot\int f_0\,\mathcal{T}\vec{v}\,\vec{v}\,d^3k \tag{4.36}$$

or

$$\vec{J} = ne^2\frac{\vec{E}}{kT}\cdot\langle\mathcal{T}\vec{v}\,\vec{v}\rangle \tag{4.37}$$

where n is the charge density given by:

$$n = \frac{1}{4\pi^3} \int f_0 \, d^3k \tag{4.38}$$

The brackets indicate the usual statistical average

$$\langle A \rangle = \frac{\int A f_0 \, d^3k}{\int f_0 \, d^3k} \tag{4.39}$$

and the domain of integration is the first Brillouin zone.

The current density is given by:

$$\vec{J} \equiv - n e \vec{\mu} . \vec{E} = \vec{\sigma} . \vec{E} \tag{4.40}$$

where $\vec{\sigma}$ and $\vec{\mu}$ are the conductivity and drift mobility tensors, respectively. The latter is therefore given by:

$$\vec{\mu} = -\left(\frac{e}{kT}\right) \langle \mathcal{T} \vec{v} \vec{v} \rangle \tag{4.41}$$

In this particular case, since $\vec{E} = \hat{i} E_x$, the drift mobility in the direction of the applied field is:

$$\mu_D = \mu_{xx} = -\frac{e}{kT} \langle \mathcal{T} v_x^2 \rangle \tag{4.41a}$$

To calculate the Hall mobility tensor, external fields are introduced:

$$\vec{E} = \hat{i} E_x + \hat{j} E_H \quad , \quad \vec{B} = \hat{k} B_z \tag{4.42}$$

Substituting into eq.(4.30) gives, to first order in B:

$$\phi(\vec{k}) = -\left(\frac{e}{\hbar}\right) \mathcal{T} \left[E_x \left(\frac{\partial \mathcal{E}}{\partial k_x}\right) + E_H \left(\frac{\partial \mathcal{E}}{\partial k_y}\right) \right] +$$

$$\left(\frac{e^2}{\hbar^3}\right) \mathcal{T} B_z \Omega_z \left\{ \mathcal{T} \left[E_x \left(\frac{\partial \mathcal{E}}{\partial k_x}\right) + E_H \left(\frac{\partial \mathcal{E}}{\partial k_y}\right) \right] \right\} \tag{4.43}$$

Substituting this into eq.(4.34), for the current density in the y direction gives:

$$J_y = \frac{e^2}{4\pi^3} \left(\frac{1}{kT}\right) \int \mathcal{T} v_y (E_x v_x + E_H v_y) f_0 \, d^3k$$

$$- \frac{e^3}{4\pi^3 \hbar^2} \left(\frac{B_z}{kT}\right) \int \mathcal{T} f_0 v_y \Omega_z \left[\mathcal{T} (E_x v_x + E_H v_y) \right] d^3k \tag{4.44}$$

but since E_x and E_H are constant, then

$$J_y = \frac{ne^2}{kT} E_x \langle \mathcal{T} v_y v_x \rangle + \frac{ne^2}{kT} E_H \langle \mathcal{T} v_y^2 \rangle$$
$$- \frac{ne^3}{\hbar^2} \frac{B_z}{kT} E_x \langle \mathcal{T} v_y \Omega_z (\mathcal{T} v_x) \rangle$$
$$- \frac{ne^3}{\hbar^2} \frac{B_z}{kT} E_H \langle \mathcal{T} v_y \Omega_z (\mathcal{T} v_y) \rangle \qquad (4.45)$$

But in the steady state, $J_y = 0$. Also, the last term in eq.(4.45) represents the magneto-resistance term, and is not significant for naphthalene. Finally, $\langle \mathcal{T} v_y v_x \rangle$ is small since $J_y \approx 0$ in the absence of a magnetic field. Therefore, eq.(4.45) becomes:

$$E_H \langle \mathcal{T} v_y^2 \rangle = \frac{e}{\hbar^2} B_z E_x \langle \mathcal{T} v_y \Omega_z (\mathcal{T} v_x) \rangle \qquad (4.46)$$

But from eq.(4.10)

$$\mu_H = \frac{V_H}{E_x B_z} \qquad (4.47)$$

Therefore, the Hall mobility is given by:

$$\mu_H = \frac{E_H}{E_x B_z} = \frac{e}{\hbar^2} \frac{\langle \mathcal{T} v_y \Omega_z (\mathcal{T} v_x) \rangle}{\langle \mathcal{T} v_y^2 \rangle} \qquad (4.48)$$

Expanding the operator Ω_z, the numerator of eq.(4.48) becomes:

$$\langle \mathcal{T} v_y \Omega_z (\mathcal{T} v_x) \rangle = \hbar^2 \langle \mathcal{T}^2 (v_y v_x M^{-1}_{yx} - v_y^2 M^{-1}_{xx}) \rangle$$
$$+ \langle \mathcal{T} v_y v_x \Omega_z \mathcal{T} \rangle \qquad (4.49)$$

where M^{-1}_{ij} is the symmetric effective mass tensor, defined by:

$$M^{-1}_{ij} \equiv \frac{1}{\hbar^2} \left(\frac{\partial^2 \mathcal{E}}{\partial k_i \partial k_j} \right) \qquad (4.50)$$

Expanding the last term of eq.(4.49):

$$\langle \mathcal{T} v_y v_x \Omega_z \mathcal{T} \rangle = \langle \mathcal{T} v_y v_x \left(\frac{\partial \mathcal{E}}{\partial k_x} \frac{\partial}{\partial k_y} - \frac{\partial \mathcal{E}}{\partial k_y} \frac{\partial}{\partial k_x} \right) \mathcal{T} \rangle$$

$$= \hbar \langle \mathcal{T} v_y \left(v_x^2 \frac{\partial \mathcal{T}}{\partial k_y} - v_x v_y \frac{\partial \mathcal{T}}{\partial k_x} \right) \rangle \qquad (4.51)$$

The last two terms are integrated by parts; the divergence theorem is then applied to give:

$$\langle \mathcal{T} v_y v_x \Omega_z \mathcal{T} \rangle = \frac{\hbar^2}{2} \left[\langle \mathcal{T}^2 v_y^2 M_{xx}^{-1} \rangle - \langle \mathcal{T}^2 v_x^2 M_{yy}^{-1} \rangle \right] \qquad (4.52)$$

Substituting eqs.(4.49) and (4.52) into eq.(4.48) gives:

$$\mu_H = \frac{1}{2} \frac{e \langle \mathcal{T}^2 [2 v_y v_x M_{yx}^{-1} - v_y^2 M_{xx}^{-1} - v_x^2 M_{yy}^{-1}] \rangle}{\langle \mathcal{T} v_y^2 \rangle} \qquad (4.53)$$

Combining eqs.(4.53) and (4.41a), the ratio of Hall to drift mobilities is:

$$\frac{\mu_H}{\mu_{xx}} = \frac{1}{2} \frac{kT \langle \mathcal{T}^2 [v_y^2 M_{xx}^{-1} + v_x^2 M_{yy}^{-1} - 2 v_y v_x M_{yx}^{-1} \rangle}{\langle \mathcal{T} v_x^2 \rangle \langle \mathcal{T} v_y^2 \rangle} \qquad (4.54)$$

4. Calculation of the Hall and Drift Mobilities in the Band Model

The pressure dependence of the lattice parameters of naphthalene was found to be (see chapter two):

$$\begin{aligned}
\vec{a} &= [8.251 \ (1 \ - \ 0.056P \ )] \hat{a} \\
\vec{b} &= [5.975 \ (1 \ - \ 0.032P \ )] \hat{b} \\
\vec{c} &= [8.670 \ (1 \ - \ 0.026P \ )] \ (\cos\beta \ \hat{a} \ + \ \sin\beta \ \hat{c}') \\
\beta &= 122.77 \ (1 \ + \ 0.014P \ ) \qquad (4.55)
\end{aligned}$$

where $\hat{a}$, $\hat{b}$ and $\hat{c}'$ form a right-handed coordinate system; P is in 10^{10}dynes/cm^2.

The reciprocal lattice vectors are defined by:

$$\vec{a}^{-1} = \frac{2\pi \ (\vec{b} \times \vec{c} \ )}{\vec{a} . (\vec{b} \times \vec{c} \ )} \quad , \quad \text{etc.}$$

which gives:

$$\vec{a}^{-1} = \frac{2\pi}{a \sin\beta} \ (\sin\beta \ \hat{a} \ - \ \cos\beta \ \hat{c}')$$

$$\vec{b}^{-1} = \frac{2\pi}{b} \ \hat{b}$$

$$\vec{c}^{-1} = \frac{2\pi}{c \sin\beta} \hat{c}' \qquad (4.56)$$

Calculations of the Hall and drift mobility tensors were carried out in the relaxation (or collision) time approximation[11]. Two simplified models for the relaxation time were considered:

a) constant isotropic relaxation time, i.e. $\tau(\vec{k}) = \tau_0$

b) constant isotropic mean free path, i.e. $\lambda = \tau(\vec{k}) |\vec{v}(\vec{k})|$

Equations (4.41) and (4.53) were used to evaluate the drift and Hall mobility tensors, respectively. The group velocity $\vec{v}(\vec{k})$ and the effective mass tensor M^{-1}_{ij} were explicitely expressed in terms of the band energies. In calculating averages over the Boltzmann distribution, both branches of the electronic bands were taken into consideration. The procedure used is illustrated by the following example, giving the average of $v_i v_j$:

$$\langle v_i v_j \rangle = \int \left\{ \frac{\partial \mathcal{E}_+}{\partial k_i} \frac{\partial \mathcal{E}_+}{\partial k_j} \exp\left[-\beta' \mathcal{E}_+(\vec{k})\right] + \frac{\partial \mathcal{E}_-}{\partial k_i} \frac{\partial \mathcal{E}_-}{\partial k_j} \exp\left[-\beta' \mathcal{E}_-(\vec{k})\right] \right\} d^3k \Big/$$

$$\hbar^2 \int \left\{ \exp\left[-\beta' \mathcal{E}_+(\vec{k})\right] + \exp\left[-\beta' \mathcal{E}_-(\vec{k})\right] \right\} d^3k \qquad (4.57)$$

where $\beta' = 1/kT$; the two branches $\mathcal{E}_+$ and $\mathcal{E}_-$ correspond to the symmetric and antisymmetric combinations of the basic molecular wavefunctions within the unit cell. They are given by:

$$\begin{aligned} \mathcal{E}_\pm(\vec{k}) = {} & 2E_2 \cos(\vec{k}\cdot\vec{c}) + 2E_3 \cos(\vec{k}\cdot\vec{b}) \\ & + 2E_4 \left[\cos\vec{k}\cdot(\vec{b}+\vec{c}) + \cos\vec{k}\cdot(\vec{b}-\vec{c})\right] \\ & + 2E_5 \cos(\vec{k}\cdot\vec{a}) + 2E_6 \cos\vec{k}\cdot(\vec{c}+\vec{a}) \\ & + 2E_7 \left[\cos\vec{k}\cdot(\vec{a}+\vec{b}) + \cos\vec{k}\cdot(\vec{a}-\vec{b})\right] \\ & \pm 2E_9 \left[\cos\vec{k}\cdot\tfrac{1}{2}(\vec{a}+\vec{b}) + \cos\vec{k}\cdot\tfrac{1}{2}(\vec{a}-\vec{b})\right] \\ & \pm 2E_{10}\left[\cos\vec{k}\cdot\left\{\tfrac{1}{2}(\vec{a}+\vec{b})+\vec{c}\right\} + \cos\vec{k}\cdot\left\{\tfrac{1}{2}(\vec{a}-\vec{b})+\vec{c}\right\}\right] \end{aligned} \qquad (4.58)$$

where E_8 , E_{11} , E_{12} , E_{13} and E_{14} have been omitted, since they are much smaller than the other transfer integrals. The values of the intermolecular integrals used in the calculations were taken from tables 3.3 , 3.4 and 3.7 .

All integrations appearing in eqs.(4.41) and (4.53) were performed

in $\vec{k}$-space over the first Brillouin zone. The first Brillouin zone is constructed from a reciprocal lattice formed by the vectors of eq.(4.56). Planes are drawn which are the perpendicular bissectors of these lattice vectors. The smallest volume enclosed by these planes is the first Brillouin zone[12]; it is shown in fig. 4.2 .

A computer program was developped to calculate the Hall and drift mobility tensors in the pressure range 0 to 6 kilobars. Evaluation of both mobility tensors, for the cases of constant relaxation time and constant mean free path, were carried out simultaneously by applying the trapezoidal integration rule (using $12^3 = 1728$ integration points); the density of points chosen allowed all integrals to converge.

Tables 4.1 to 4.6 show the components of the drift mobility tensor calculated assuming constant free time and constant free path (not including the constant multiplicative factors $e\tau/kT$ and $e\lambda/kT$, respectively), while tables 4.7 to 4.12 give the corresponding components of the Hall mobility tensor (without the multiplicative factors $10^{14}\tau$ and $10^{7}\lambda$); the minus signs indicate anomalous Hall mobilities.

All mobility components were evaluated for three different energy bands:

(i) The first band was constructed from only the two-center resonance integrals.

(ii) The second one included the contributions of the three-center integrals.

(iii) The third band added the contributions of the exchange effects and the vibrational overlap.

All mobility components which are not listed are at least 100 times smaller than the smallest terms in their corresponding tables. For the Hall mobilities μ_{ij} , the first subscript i indicates the direction of the applied electric field, while the second index j corresponds to the direction of the magnetic field.

Table 4.13 shows a comparison between the mobility anisotropies, at atmospheric pressure, obtained with the third band model and the available experimental data for naphthalene[13,14,15]. It can be seen that, although both the constant τ and the constant λ approximations tend to exaggerate the drift mobility anisotropy, the constant τ approximation does it to a somewhat greater degree. This is in agreement with Leblanc's observation[16]

that for conduction in narrow bands, mean free path is constant rather than the mean free time. The discrepancy may also be due to the assumption of an isotropic relaxation time. Kubarev and Mikhailov[17,18] have suggested that the relaxation time in a particular direction be taken inversely proportional to the bandwidth in that direction. As shown in the last two columns of table 4.13, this would in fact lead to a closer agreement with the anisotropies obtained from the experimental values of the drift mobility.

Finally, figs. 4.3(a,b) to 4.14(a,b) , where a refers to holes and b to electrons, show the variation with pressure of the mobility tensors. All the ordinates are of the form μ/μ_o , where μ_o is the atmospheric value of the plotted mobility.

Figs. 4.3 to 4.8 give the variation with pressure of the normalized drift mobility tensor. Figs. 4.3 and 4.4 correspond to calculations carried out in the constant τ and constant λ approximations, respectively, using only the two-center integrals. Figs. 4.5 and 4.6 (constant τ and constant λ approximations respectively) correspond to the case when two- and three-center integrals are taken into consideration. Figs. 4.7 and 4.8 (constant τ and constant λ approximations respectively) give the pressure dependence of the drift mobility tensor when exchange and vibrational effects are taken into consideration. It can be seen that the curves for the constant τ approximation (figs. 4.3 , 4.5 and 4.7) are in general agreement, even though the atmospheric values of the plotted mobilities increase with the inclusion of additional interactions (see tables 4.1 , 4.3 and 4.5). Similar conclusions can be reached concerning the curves for the constant λ approximation (figs. 4.4 , 4.6 and 4.8, and tables 4.2 , 4.4 and 4.6).

Figs. 4.9 to 4.14 show the pressure dependence of the normalized Hall mobility tensor; not all components of the tensor were plotted, but only the three or four components that had the largest values at atmospheric pressure. The Hall mobility curves obtained by using the resonance integrals only (figs. 4.11 and 4.12) are now compared with those obtained when exchange and vibrational effects are taken into consideration (figs. 4.13 and 4.14). One notices that the curves for the constant τ approximation (figs. 4.11 and 4.13) are in general agreement, except for the variation with pressure of the Hall mobility of holes μ_{12} (current parallel to the

a axis, and magnetic field parallel to the b axis). Similarly, the two curves corresponding to the constant λ approximation (figs. 4.12 and 4.14) show opposite variations with pressure for the Hall mobility of holes μ_{21}. Also, by comparing figs. 4.13 and 4.14 for the constant τ and constant λ approximations, respectively, one notices the same reversal in the sign of the variation of μ_{21} (holes) with pressure. This suggests that measurements of the Hall mobilities μ_{21} and μ_{12} should favor one band model over the other, in addition to showing which approximation (constant τ or constant λ) describes best the transport of charges in naphthalene.

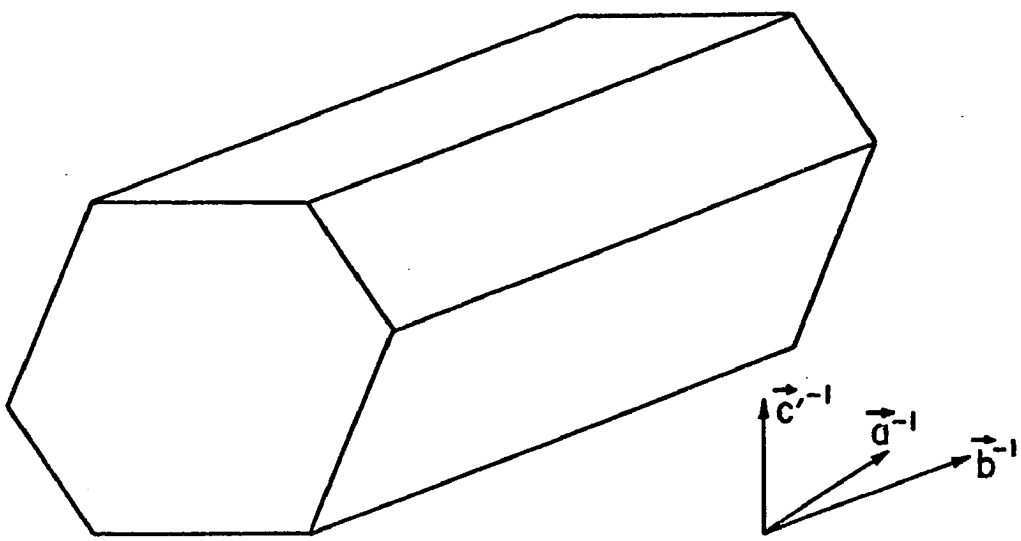

FIG. 4.2

Table 4.1 - Components of the drift mobility tensor (constant τ approximation) corresponding to the two-center resonance integrals[a].

Component \ Pressure (Kbars)	Atm.	1.0	2.0	3.0	4.0	5.0	6.0
			Hole				
μ_{aa}	7.28	8.45	9.78	11.27	12.95	14.81	16.90
μ_{bb}	161.19	171.86	182.89	194.89	206.93	220.23	233.84
$\mu_{c'c'}$	30.31	33.94	37.89	42.17	46.85	51.88	57.33
$\mu_{ac'}$	-1.98	-2.37	-2.82	-3.33	-3.90	-4.55	-5.27
			Electron				
μ_{aa}	43.17	45.22	47.33	49.51	51.69	53.93	56.19
μ_{bb}	28.64	30.32	32.08	33.93	35.87	37.91	40.05
$\mu_{c'c'}$	0.97	1.30	1.70	2.20	2.82	3.56	4.45
$\mu_{ac'}$	-0.40	-0.52	-0.68	-0.87	-1.10	-1.39	-1.73

[a] All mobility components in units of $10^{10} e\tau/kT$ $cm^2/V\text{-}sec$; τ in seconds, e in coulombs and kT in joules.

Table 4.2 - Components of the drift mobility tensor (constant λ approximation) corresponding to the two-center resonance integrals[a].

Component \ Pressure (Kbars)	Atm.	1.0	2.0	3.0	4.0	5.0	6.0
			Hole				
μ_{aa}	0.514	0.572	0.635	0.701	0.774	0.851	0.933
μ_{bb}	10.076	10.332	10.584	10.851	11.100	11.372	11.634
$\mu_{c'c'}$	1.979	2.124	2.276	2.432	2.599	2.767	2.945
$\mu_{ac'}$	-0.145	-0.168	-0.194	-0.221	-0.251	-0.283	-0.317
			Electron				
μ_{aa}	4.518	4.606	4.692	4.775	4.852	4.924	4.992
μ_{bb}	3.129	3.207	3.284	3.362	3.441	3.521	3.601
$\mu_{c'c'}$	0.172	0.221	0.278	0.344	0.420	0.508	0.607
$\mu_{ac'}$	-0.035	-0.046	-0.058	-0.073	-0.091	-0.113	-0.139

[a] All mobility components in units of $10^5 e\lambda/kT$ $cm^2/V\text{-}sec$; λ in cm, e in coulombs and kT in joules.

Table 4.3 - Components of the drift mobility tensor (constant τ approximation) corresponding to the resonance integrals (two-and three-center)[a].

Component \ Pressure (Kbars)	Atm.	1.0	2.0	3.0	4.0	5.0	6.0
			Hole				
μ_{aa}	9.36	10.92	12.62	14.56	16.75	19.18	21.92
μ_{bb}	235.45	249.91	265.01	281.11	297.48	314.79	332.64
$\mu_{c'c'}$	43.20	48.47	53.99	59.97	66.31	72.87	80.04
$\mu_{ac'}$	-2.63	-3.16	-3.92	-4.62	-5.38	-6.28	-7.21
			Electron				
μ_{aa}	44.91	47.15	49.41	51.72	54.06	56.46	58.88
μ_{bb}	31.12	33.01	34.97	37.01	39.15	41.41	43.79
$\mu_{c'c'}$	1.08	1.51	2.06	2.72	3.49	4.43	5.51
$\mu_{ac'}$	-0.48	-0.64	-0.85	-1.10	-1.40	-1.77	-2.20

[a] All mobility components in units of $10^{10} e\tau/kT$ $cm^2/V\text{-}sec$; τ in seconds, e in coulombs and kT in joules.

Table 4.4 - Components of the drift mobility tensor (constant λ approximation) corresponding to the resonance integrals (two-and three-center)[a].

Component \ Pressure (Kbars)	Atm.	1.0	2.0	3.0	4.0	5.0	6.0
			Hole				
μ_{aa}	0.544	0.609	0.676	0.750	0.831	0.917	1.012
μ_{bb}	12.167	12.439	12.718	13.003	13.278	13.563	13.840
$\mu_{c'c'}$	2.312	2.492	2.667	2.853	3.043	3.227	3.426
$\mu_{ac'}$	-0.155	-0.182	-0.219	-0.251	-0.283	-0.321	-0.358
			Electron				
μ_{aa}	4.584	4.673	4.756	4.837	4.913	4.985	5.051
μ_{bb}	3.244	3.327	3.409	3.491	3.575	3.659	3.746
$\mu_{c'c'}$	0.190	0.253	0.330	0.414	0.506	0.610	0.725
$\mu_{ac'}$	-0.042	-0.055	-0.073	-0.092	-0.115	-0.143	-0.175

[a] All mobility components in units of $10^5 e\lambda/kT$ $cm^2/V\text{-}sec$; λ in cm, e in coulombs and kT in joules.

Table 4.5 - Components of the drift mobility tensor (constant τ approximation) corresponding to the transfer integrals (IRS - IE).F[a].

Component \ Pressure (Kbars)	Atm.	1.0	2.0	3.0	4.0	5.0	6.0
				Hole			
μ_{aa}	36.81	41.09	45.74	50.91	56.51	62.56	69.25
μ_{bb}	606.31	631.28	656.44	682.07	708.13	735.03	761.95
$\mu_{c'c'}$	108.49	118.51	129.16	140.54	152.62	165.15	178.85
$\mu_{ac'}$	-5.91	-6.89	-8.13	-9.33	-10.57	-11.91	-13.31
				Electron			
μ_{aa}	123.10	126.46	129.81	133.04	136.21	139.39	142.44
μ_{bb}	76.22	79.20	82.29	85.43	88.71	92.08	95.61
$\mu_{c'c'}$	3.19	4.44	5.99	7.88	10.11	12.79	15.90
$\mu_{ac'}$	-1.16	-1.64	-2.24	-2.96	-3.85	-4.92	-6.18

[a] All mobility components in units of $10^{10} e\tau/kT$ $cm^2/V\text{-}sec$; τ in seconds, e in coulombs and kT in joules.

Table 4.6 - Components of the drift mobility tensor (constant λ approximation) corresponding to the transfer integrals (IRS - IE).F[a].

Component \ Pressure (Kbars)	Atm.	1.0	2.0	3.0	4.0	5.0	6.0
				Hole			
μ_{aa}	1.263	1.376	1.495	1.626	1.765	1.911	2.070
μ_{bb}	18.839	19.087	19.326	19.558	19.786	20.018	20.230
$\mu_{c'c'}$	3.581	3.820	4.066	4.323	4.589	4.855	5.142
$\mu_{ac'}$	-0.271	-0.309	-0.355	-0.397	-0.439	-0.483	-0.528
				Electron			
μ_{aa}	7.654	7.717	7.769	7.810	7.841	7.863	7.873
μ_{bb}	4.877	4.942	5.007	5.071	5.135	5.200	5.266
$\mu_{c'c'}$	0.334	0.448	0.582	0.736	0.908	1.102	1.317
$\mu_{ac'}$	-0.062	-0.087	-0.119	-0.156	-0.201	-0.255	-0.318

[a] All mobility components in units of $10^5 e\lambda/kT$ $cm^2/V\text{-}sec$; λ in cm, e in coulombs and kT in joules.

Table 4.7 - Components of the Hall mobility tensor (constant τ approximation) corresponding to the two-center resonance integrals[a].

Pressure (Kbars) / Component[b]	Atm.	1.0	2.0	3.0	4.0	5.0	6.0
				Hole			
μ_{13}	-0.071	-0.079	-0.086	-0.094	-0.103	-0.111	-0.120
μ_{12}	-0.036	-0.034	-0.031	-0.028	-0.023	-0.018	-0.012
μ_{23}	-1.571	-1.593	-1.613	-1.630	-1.643	-1.655	-1.662
μ_{21}	-1.588	-1.610	-1.630	-1.647	-1.660	-1.671	-1.676
μ_{32}	-0.152	-0.138	-0.122	-0.105	-0.085	-0.065	-0.042
μ_{31}	-0.298	-0.318	-0.338	-0.357	-0.376	-0.394	-0.411
				Electron			
μ_{13}	0.506	0.516	0.526	0.535	0.543	0.551	0.557
μ_{12}	-0.537	-0.561	-0.582	-0.599	-0.614	-0.626	-0.637
μ_{23}	0.334	0.345	0.356	0.366	0.376	0.386	0.396
μ_{21}	-0.179	-0.174	-0.169	-0.163	-0.156	-0.149	-0.142
μ_{32}	-0.012	-0.016	-0.021	-0.026	-0.033	-0.041	-0.050
μ_{31}	-0.006	-0.007	-0.009	-0.011	-0.012	-0.014	-0.016

[a] All mobility components in units of $10^{14}\tau$ $cm^2/V\text{-}sec$; τ in seconds.

[b] For μ_{ij} , the first subscript i indicates the direction of the applied electric field, while the second index j corresponds to the direction of the magnetic field.

Table 4.8 - Components of the Hall mobility tensor (constant λ approximation) corresponding to the two-center resonance integrals[a].

Pressure (Kbars) / Component[b]	Atm.	1.0	2.0	3.0	4.0	5.0	6.0
				Hole			
μ_{13}	-0.158	-0.141	-0.121	-0.102	-0.080	-0.057	-0.033
μ_{12}	0.428	0.492	0.556	0.622	0.690	0.756	0.822
μ_{23}	-3.101	-2.542	-2.018	-1.577	-1.150	-0.761	-0.409
μ_{21}	-2.756	-2.301	-1.916	-1.514	-1.119	-0.700	-0.285
μ_{32}	1.648	1.828	1.994	2.155	2.317	2.458	2.592
μ_{31}	-0.541	-0.473	-0.412	-0.339	-0.262	-0.170	-0.072
				Electron			
μ_{13}	1.105	1.124	1.142	1.156	1.167	1.175	1.181
μ_{12}	-12.810	-12.120	-11.320	-10.710	-10.170	-9.690	-9.270
μ_{23}	0.765	0.783	0.800	0.814	0.828	0.840	0.852
μ_{21}	-5.740	-5.481	-5.243	-5.029	-4.837	-4.661	-4.495
μ_{32}	-0.489	-0.581	-0.670	-0.771	-0.881	-1.000	-1.128
μ_{31}	-0.316	-0.377	-0.443	-0.514	-0.591	-0.672	-0.758

[a] All mobility components in units of $10^7\lambda$ $cm^2/V\text{-}sec$; λ in cm .

[b] For μ_{ij} , the first subscript i indicates the direction of the applied electric field, while the second index j corresponds to the direction of the magnetic field.

Table 4.9 - Components of the Hall mobility tensor (constant τ approximation) corresponding to the resonance integrals (two-and three-center)[a].

Pressure (Kbars) / Component[b]	Atm.	1.0	2.0	3.0	4.0	5.0	6.0
				Hole			
μ_{13}	-0.071	-0.078	-0.086	-0.094	-0.103	-0.111	-0.120
μ_{12}	-0.040	-0.037	-0.023	-0.017	-0.011	+0.001	+0.010
μ_{23}	-1.772	-1.787	-1.813	-1.821	-1.824	-1.827	-1.820
μ_{21}	-1.806	-1.820	-1.845	-1.853	-1.853	-1.854	-1.843
μ_{32}	-0.183	-0.162	-0.098	-0.070	-0.042	+0.004	+0.038
μ_{31}	-0.331	-0.353	-0.376	-0.395	-0.413	-0.429	-0.444
				Electron			
μ_{13}	0.543	0.552	0.561	0.568	0.575	0.581	0.586
μ_{12}	-0.548	-0.590	-0.639	-0.659	-0.675	-0.678	-0.688
μ_{23}	0.376	0.386	0.397	0.407	0.416	0.426	0.436
μ_{21}	-0.202	-0.190	-0.184	-0.175	-0.169	-0.159	-0.153
μ_{32}	-0.013	-0.019	-0.027	-0.035	-0.044	-0.053	-0.064
μ_{31}	-0.007	-0.009	-0.011	-0.013	-0.015	-0.017	-0.019

[a] All mobility components in units of $10^{14}\tau$ $cm^2/V\text{-}sec$; τ in seconds.

[b] For μ_{ij} , the first subscript i indicates the direction of the applied electric field, while the second index j corresponds to the direction of the magnetic field.

Table 4.10 - Components of the Hall mobility tensor (constant λ approximation) corresponding to the resonance integrals (two-and three-center)[a].

Component[b] \ Pressure (Kbars)	Atm.	1.0	2.0	3.0	4.0	5.0	6.0
				Hole			
μ_{13}	-0.035	-0.012	-0.010	+0.014	+0.048	+0.083	+0.121
μ_{12}	0.396	0.460	0.569	0.630	0.695	0.785	0.852
μ_{23}	-0.779	-0.240	-0.195	+0.244	+0.761	+1.230	+1.659
μ_{21}	-1.166	-0.625	-0.351	+0.057	+0.458	+0.834	+1.251
μ_{32}	1.680	1.880	2.246	2.397	2.545	2.761	2.887
μ_{31}	-0.222	-0.125	-0.074	+0.012	+0.105	+0.198	+0.310
				Electron			
μ_{13}	1.385	1.394	1.406	1.408	1.403	1.390	1.379
μ_{12}	-13.140	-12.290	-11.520	-10.830	-10.260	-9.682	-9.259
μ_{23}	0.980	0.992	1.008	1.016	1.021	1.021	1.022
μ_{21}	-5.856	-5.496	-5.197	-4.956	-4.762	-4.572	-4.411
μ_{32}	-0.544	-0.667	-0.799	-0.926	-1.056	-1.185	-1.328
μ_{31}	-0.343	-0.419	-0.503	-0.587	-0.674	-0.763	-0.853

[a] All mobility components in units of $10^7\lambda$ $cm^2/V\text{-}sec$; λ in cm .

[b] For μ_{ij} , the first subscript i indicates the direction of the applied electric field, while the second index j corresponds to the direction of the magnetic field.

Table 4.11 - Components of the Hall mobility tensor (constant τ approximation) corresponding to the transfer integrals (IRS - IE).F[a].

Pressure (Kbars) / Component[b]	Atm.	1.0	2.0	3.0	4.0	5.0	6.0
				Hole			
μ_{13}	-0.128	-0.134	-0.139	-0.143	-0.146	-0.148	-0.148
μ_{12}	0.079	0.100	0.129	0.153	0.178	0.205	0.231
μ_{23}	-2.115	-2.055	-1.994	-1.917	-1.830	-1.736	-1.630
μ_{21}	-2.048	-1.975	-1.902	-1.807	-1.700	-1.584	-1.452
μ_{32}	0.232	0.288	0.364	0.423	0.480	0.541	0.597
μ_{31}	-0.367	-0.371	-0.374	-0.372	-0.366	-0.356	-0.341
				Electron			
μ_{13}	0.707	0.716	0.723	0.729	0.733	0.735	0.736
μ_{12}	-0.786	-0.849	-0.905	-0.937	-0.962	-0.975	-0.986
μ_{23}	0.438	0.448	0.458	0.468	0.478	0.485	0.494
μ_{21}	-0.309	-0.308	-0.307	-0.305	-0.303	-0.300	-0.297
μ_{32}	-0.020	-0.030	-0.042	-0.056	-0.071	-0.089	-0.110
μ_{31}	-0.013	-0.017	-0.022	-0.028	-0.035	-0.042	-0.049

[a] All mobility components in units of $10^{14}\tau$ cm^2/V-sec ; τ in seconds.

[b] For μ_{ij} , the first subscript i indicates the direction of the applied electric field, while the second index j corresponds to the direction of the magnetic field.

Table 4.12 - Components of the Hall mobility tensor (constant λ approximation) corresponding to the transfer integrals (IRS - IE).F[a].

Pressure (Kbars) / Component[b]	Atm.	1.0	2.0	3.0	4.0	5.0	6.0
				Hole			
μ_{13}	0.309	0.361	0.409	0.465	0.527	0.594	0.684
μ_{12}	1.013	1.069	1.150	1.207	1.262	1.326	1.403
μ_{23}	4.617	5.004	5.282	5.593	5.907	6.226	6.679
μ_{21}	5.380	5.829	6.209	6.590	6.907	7.191	7.434
μ_{32}	2.872	2.969	3.127	3.209	3.281	3.369	3.484
μ_{31}	1.023	1.167	1.306	1.457	1.602	1.744	1.890
				Electron			
μ_{13}	-0.975	-0.901	-0.825	-0.751	-0.683	-0.629	-0.571
μ_{12}	-14.552	-13.525	-12.484	-11.665	-10.983	-10.375	-9.870
μ_{23}	-0.621	-0.577	-0.532	-0.488	-0.448	-0.416	-0.382
μ_{21}	-6.356	-6.027	-5.754	-5.530	-5.343	-5.169	-5.008
μ_{32}	-0.635	-0.785	-0.936	-1.099	-1.272	-1.454	-1.651
μ_{31}	-0.435	-0.546	-0.669	-0.802	-0.944	-1.096	-1.252

[a] All mobility components in units of $10^7\lambda$ $cm^2/V\text{-}sec$; λ in cm .

[b] For μ_{ij} , the first subscript i indicates the direction of the applied electric field, while the second index j corresponds to the direction of the magnetic field.

Table 4.13 - Comparison of the drift mobility ratios of naphthalene in the anisotropic τ and the anisotropic λ approximations.

Ratio	B.W. ratios[a]	Exp.[b]	Mobility ratios const.τ[c]	const.λ[c]	anisot.τ[d]	anisot.λ[d]
			Hole			
bb/aa	8.019	1.55	16.471	14.916	2.054	1.860
c'c'/aa	5.560	0.73	2.947	2.835	0.530	0.510
			Electron			
bb/aa	1.000	1.02	0.619	0.637	0.619	0.637
c'c'/aa	0.099	0.97	0.026	0.044	0.261	0.439

[a] The bandwidth ratios were taken from table 3.11

[b] Average of the drift mobility data published by Mey et al[13], Silver et al[14], and Spielberg et al[15].

[c] The drift mobility ratios were taken from tables 4.5 and 4.6 .

[d] All values in the last two columns were obtained by multiplying the corresponding mobility ratios in the constant τ or constant λ approximations (fourth and fifth columns respectively) by the reciprocal of the bandwidth ratio given in the second column.

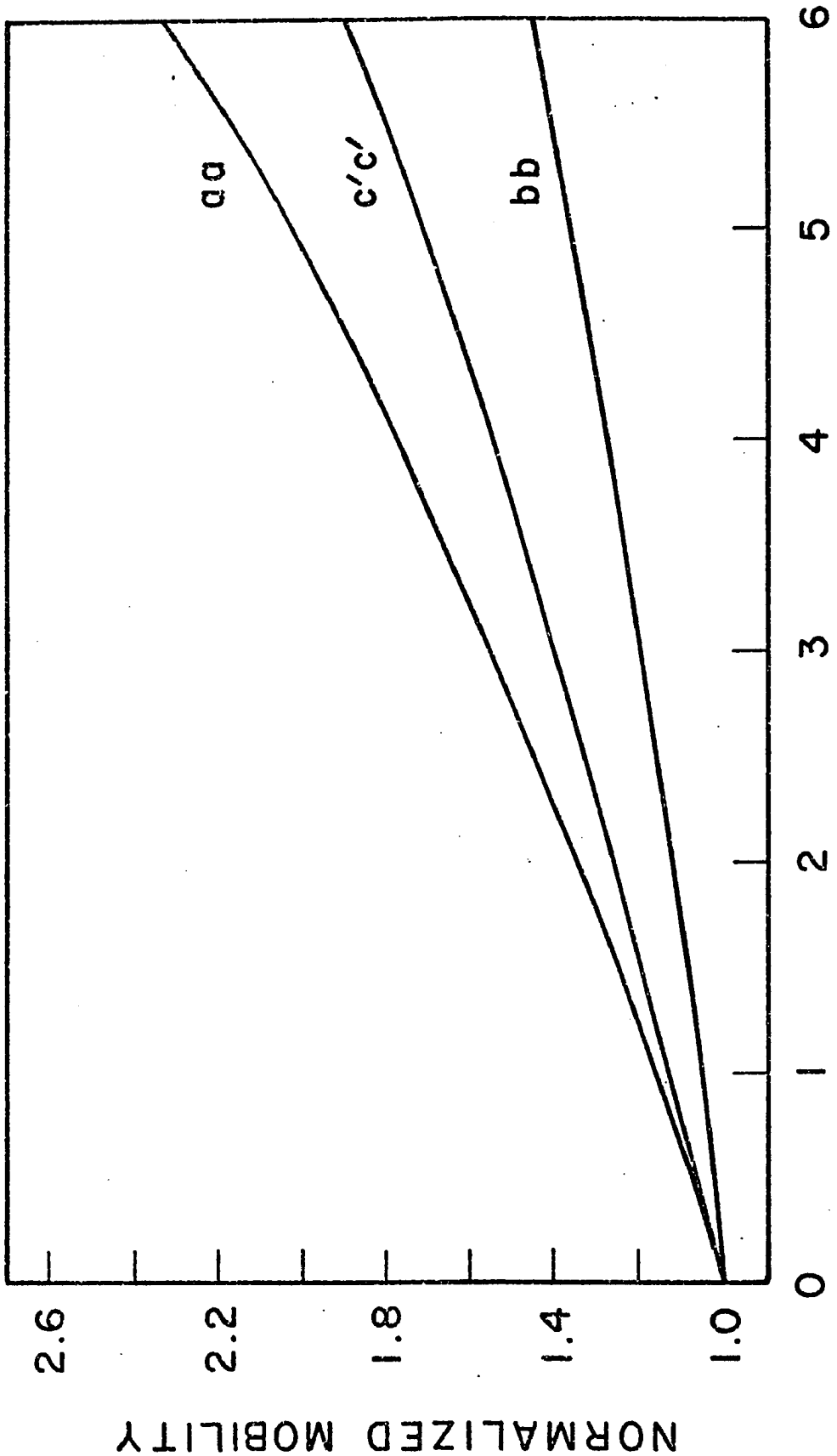

FIG. 4.3a

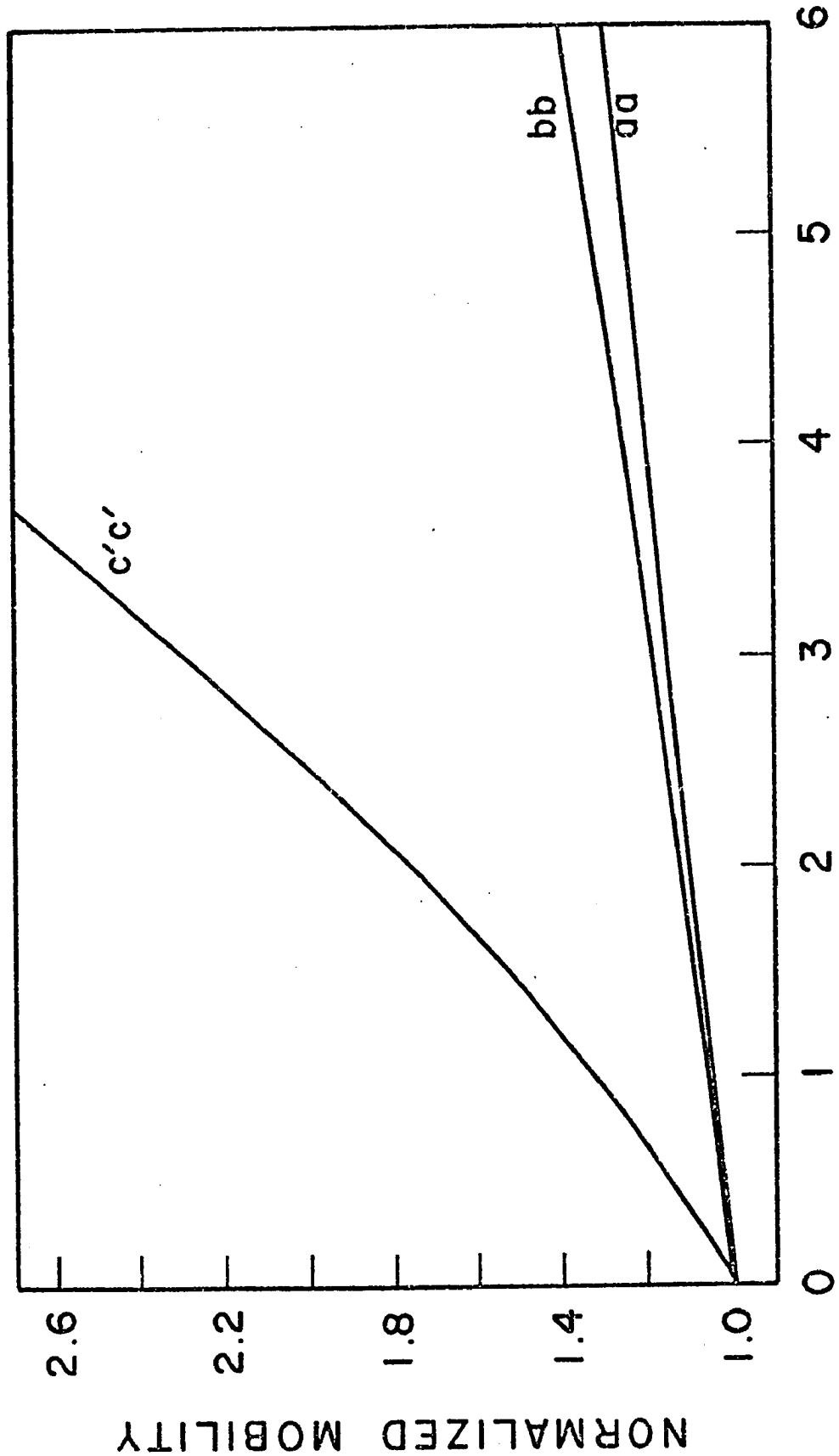

FIG. 4.3b

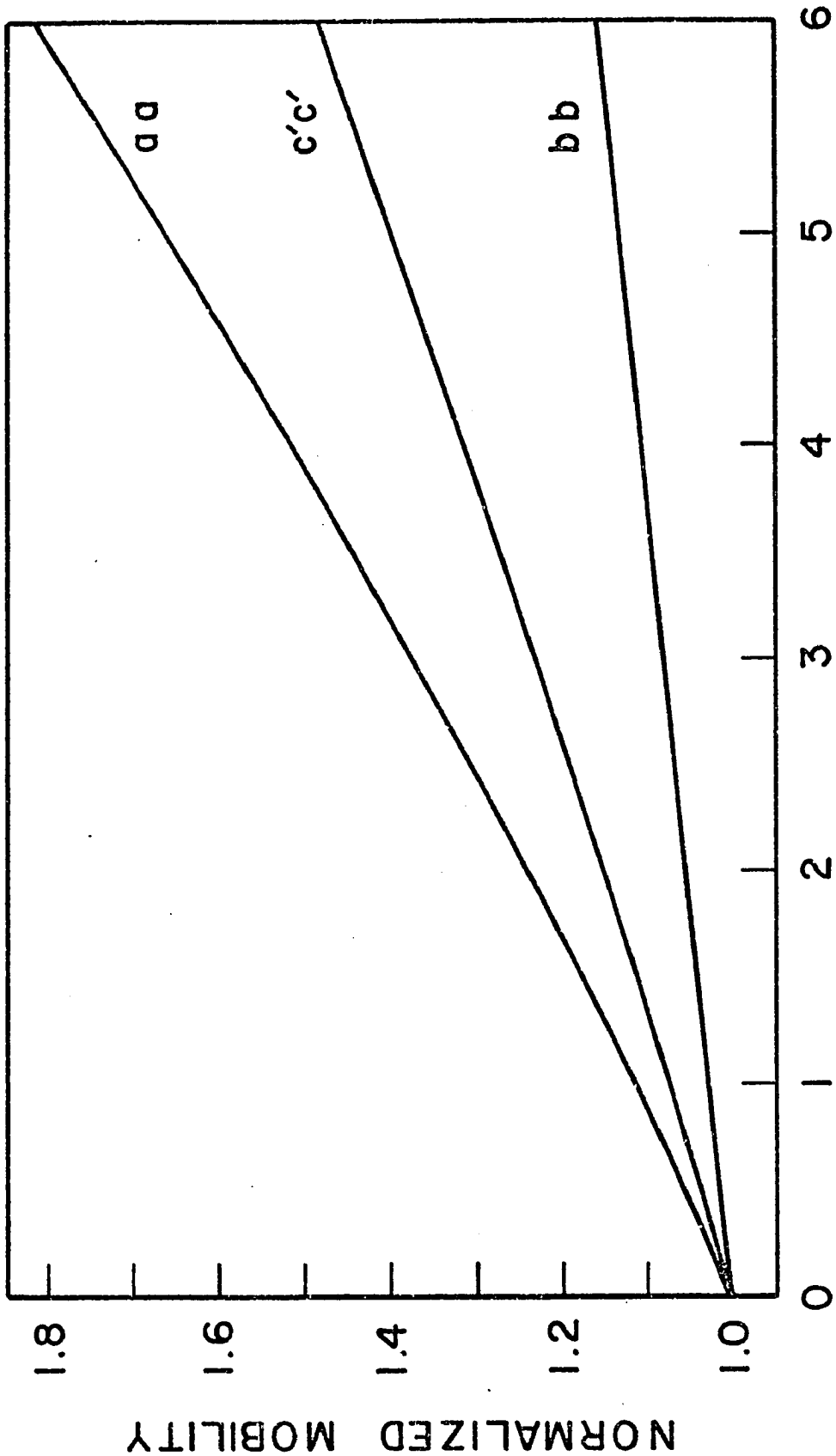

FIG. 4.4a

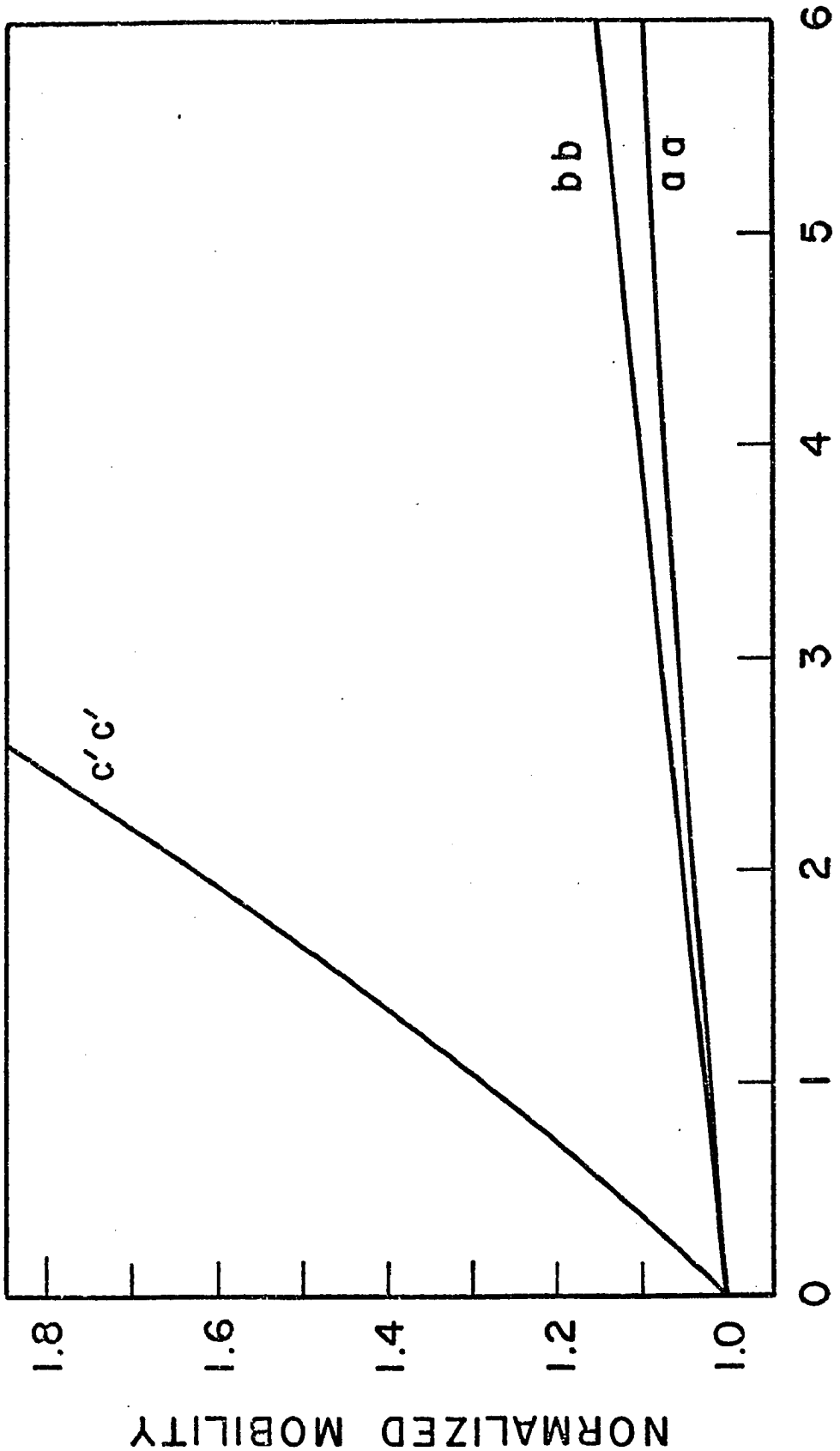

FIG. 4.4b

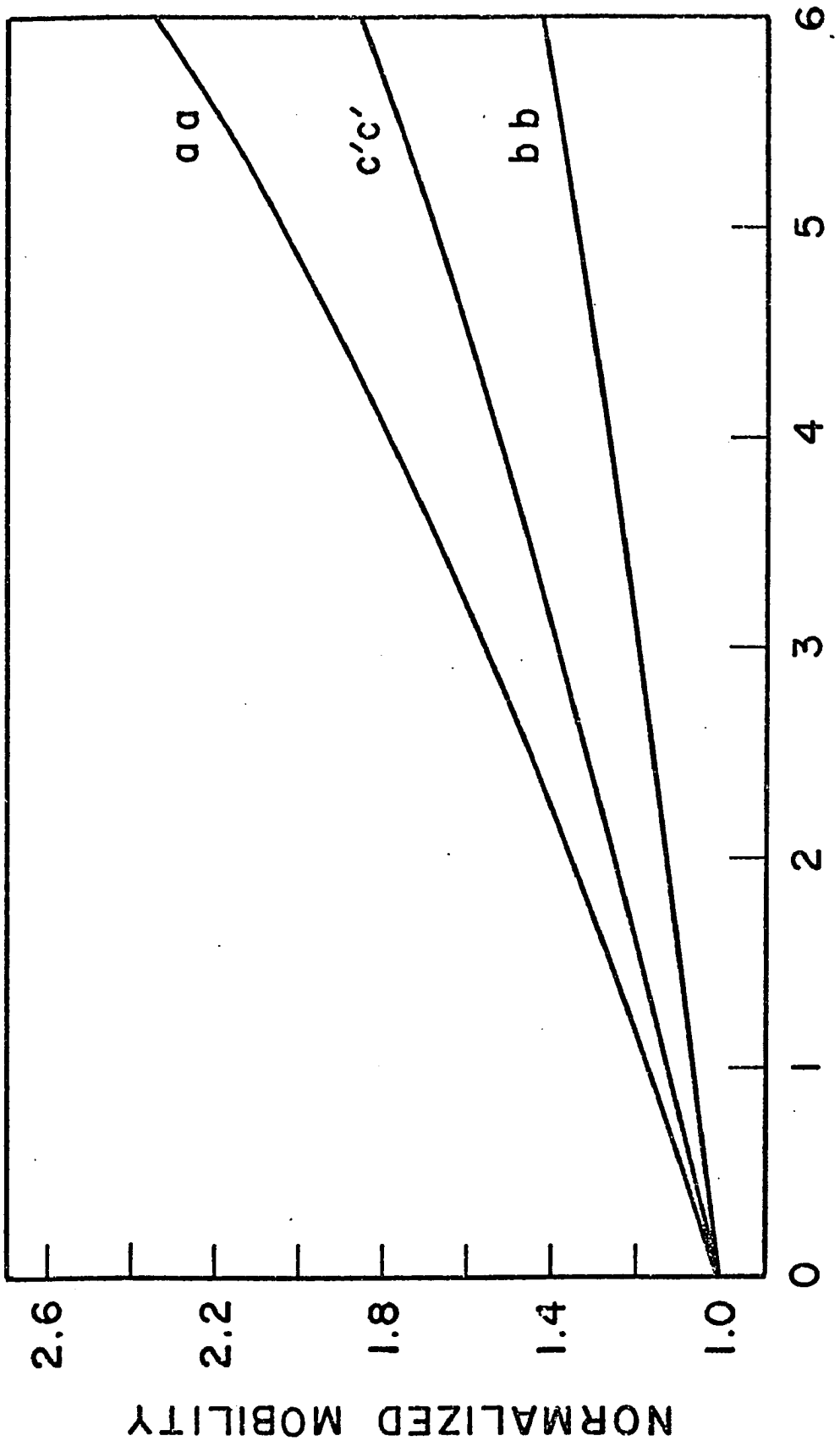

FIG. 4.5a

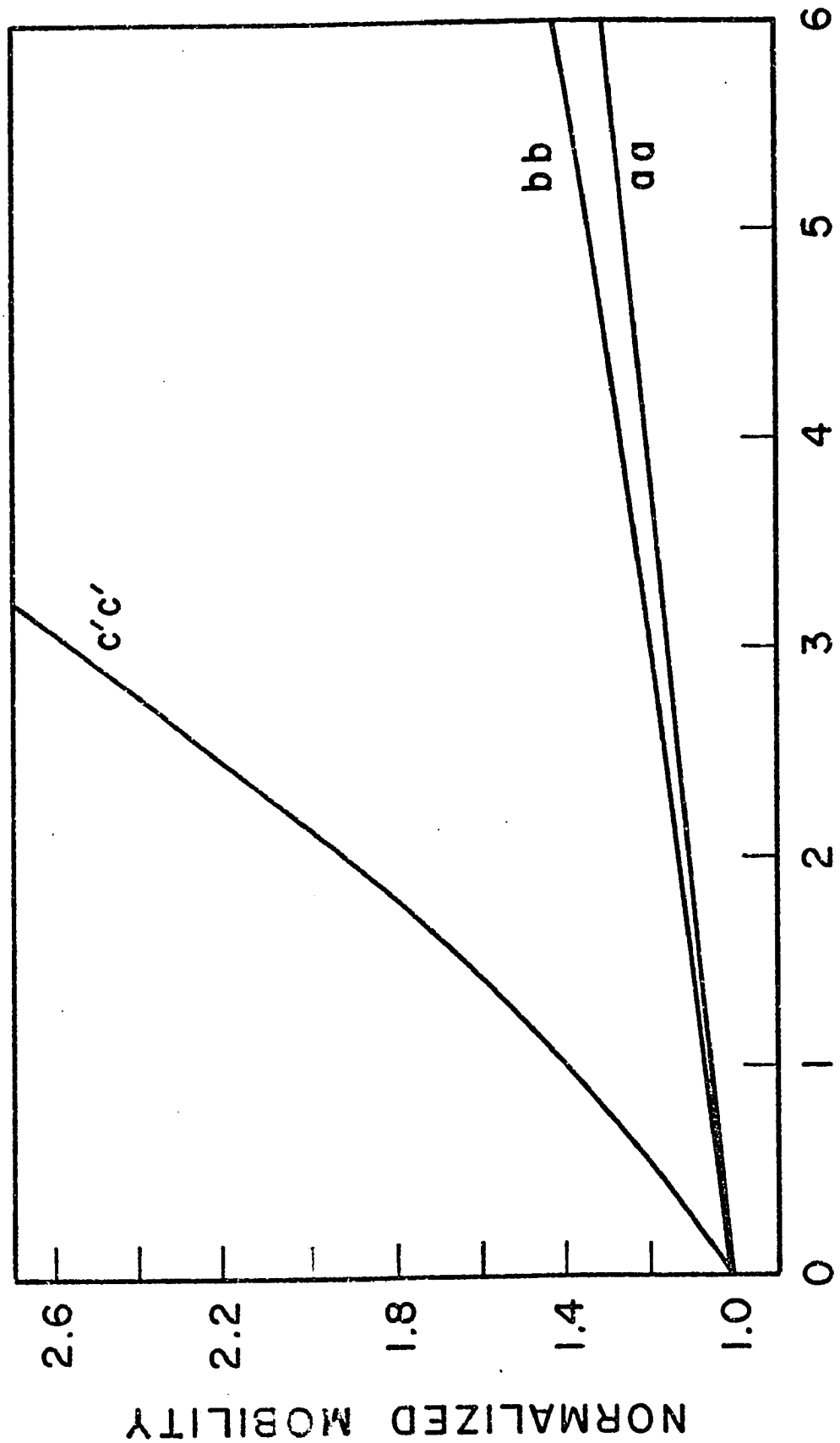

FIG. 4.5b

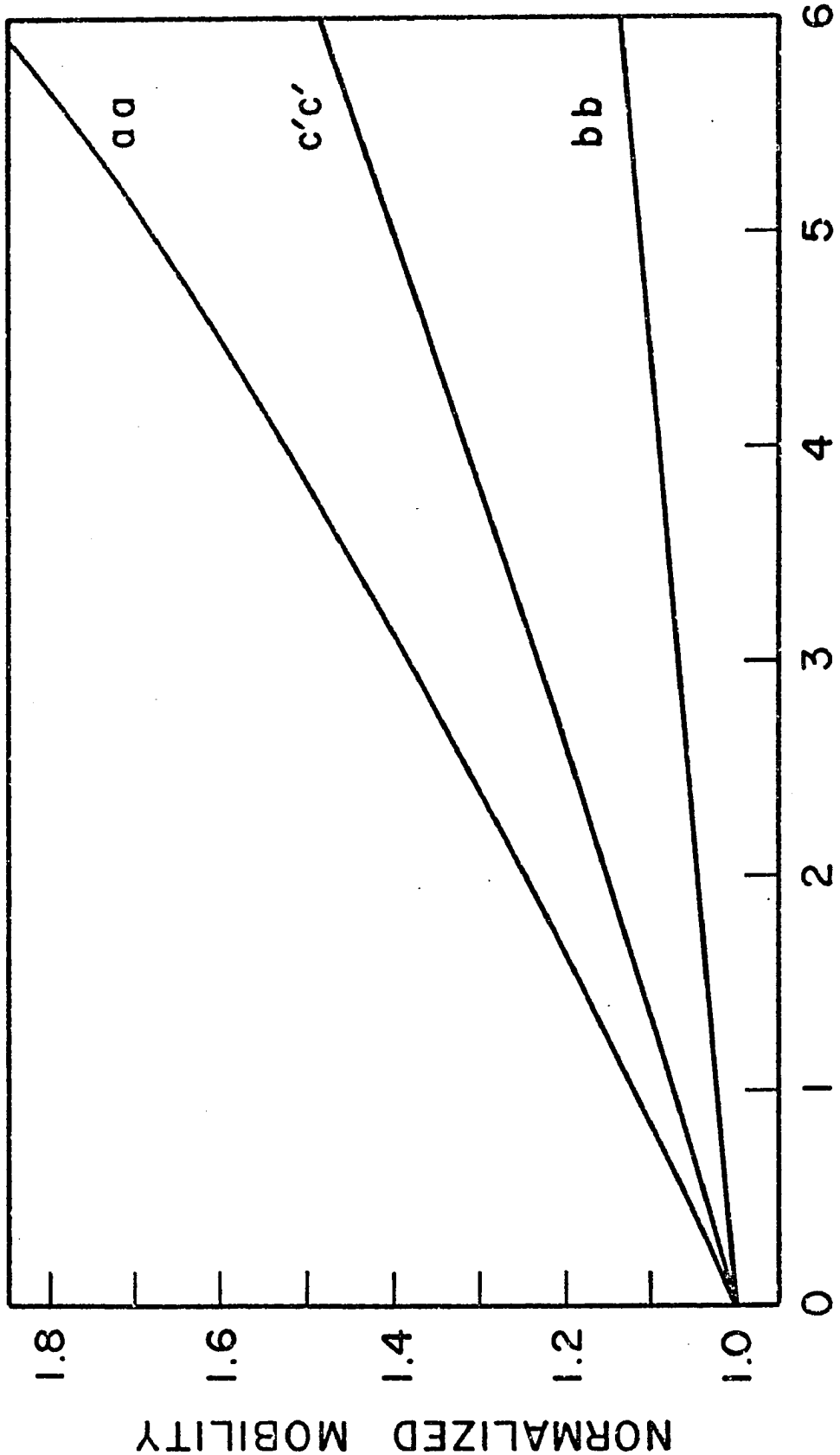

FIG. 4.6a

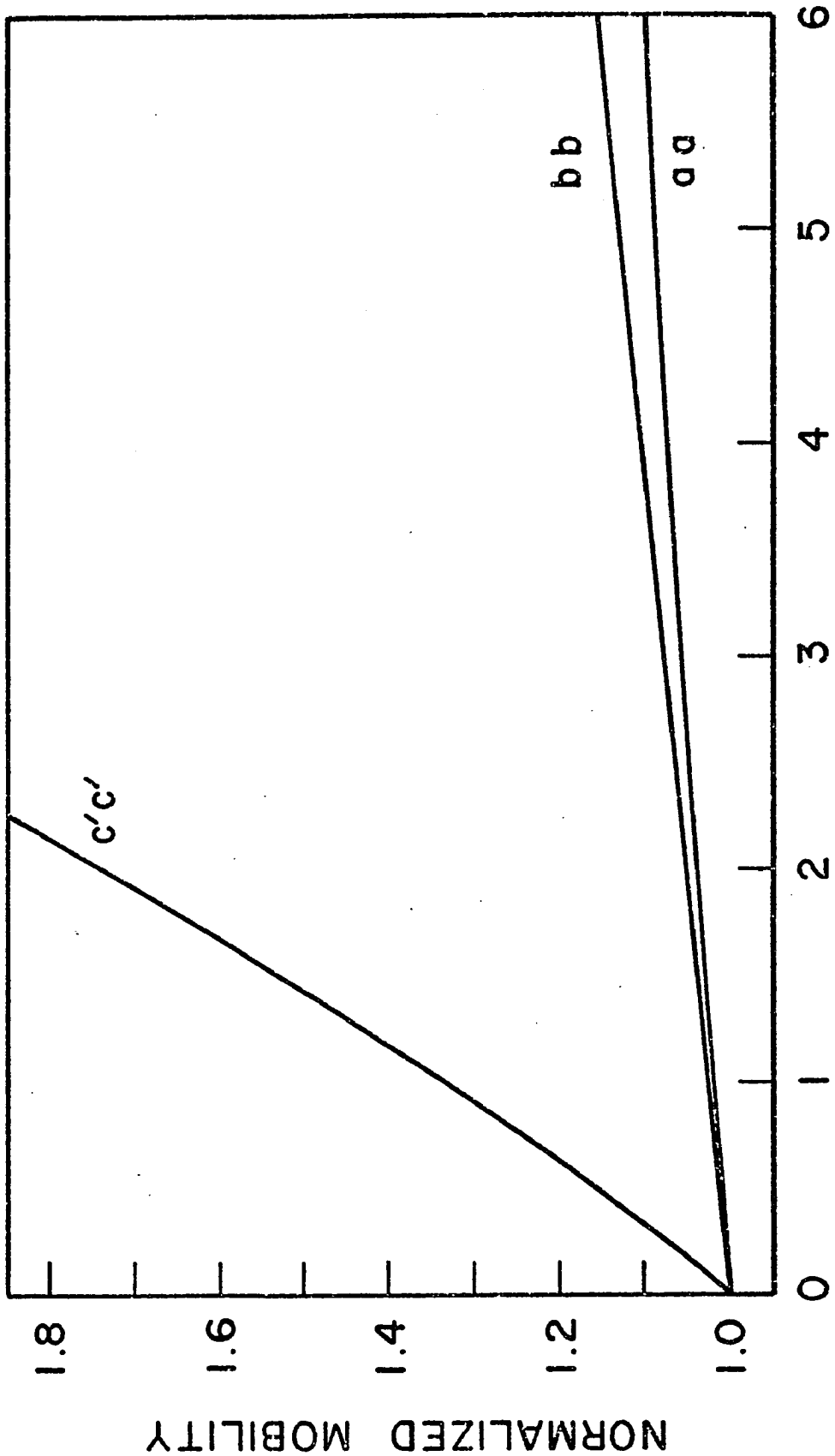

FIG. 4.6b

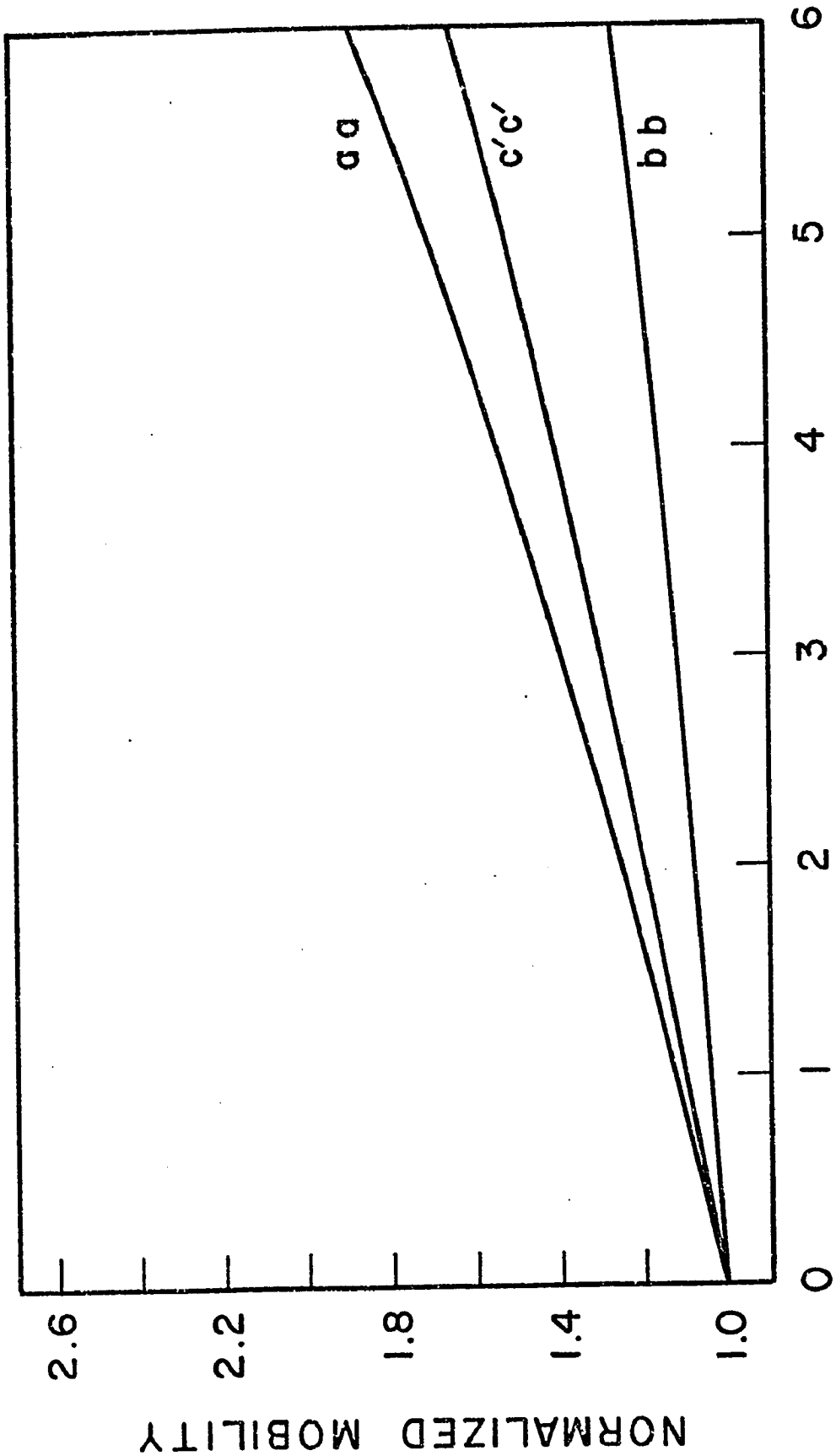

FIG. 4.7a

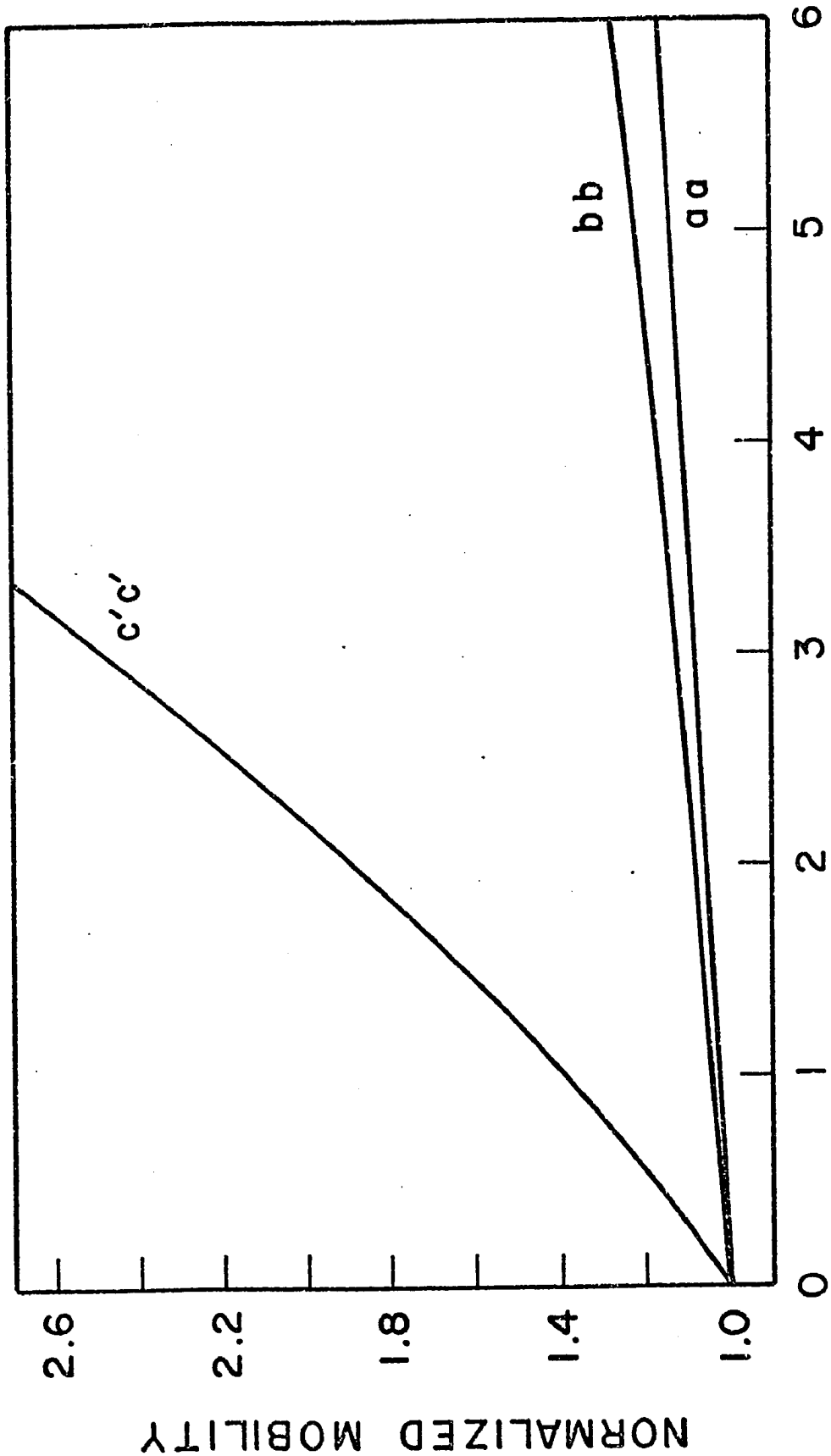

FIG. 4.7b

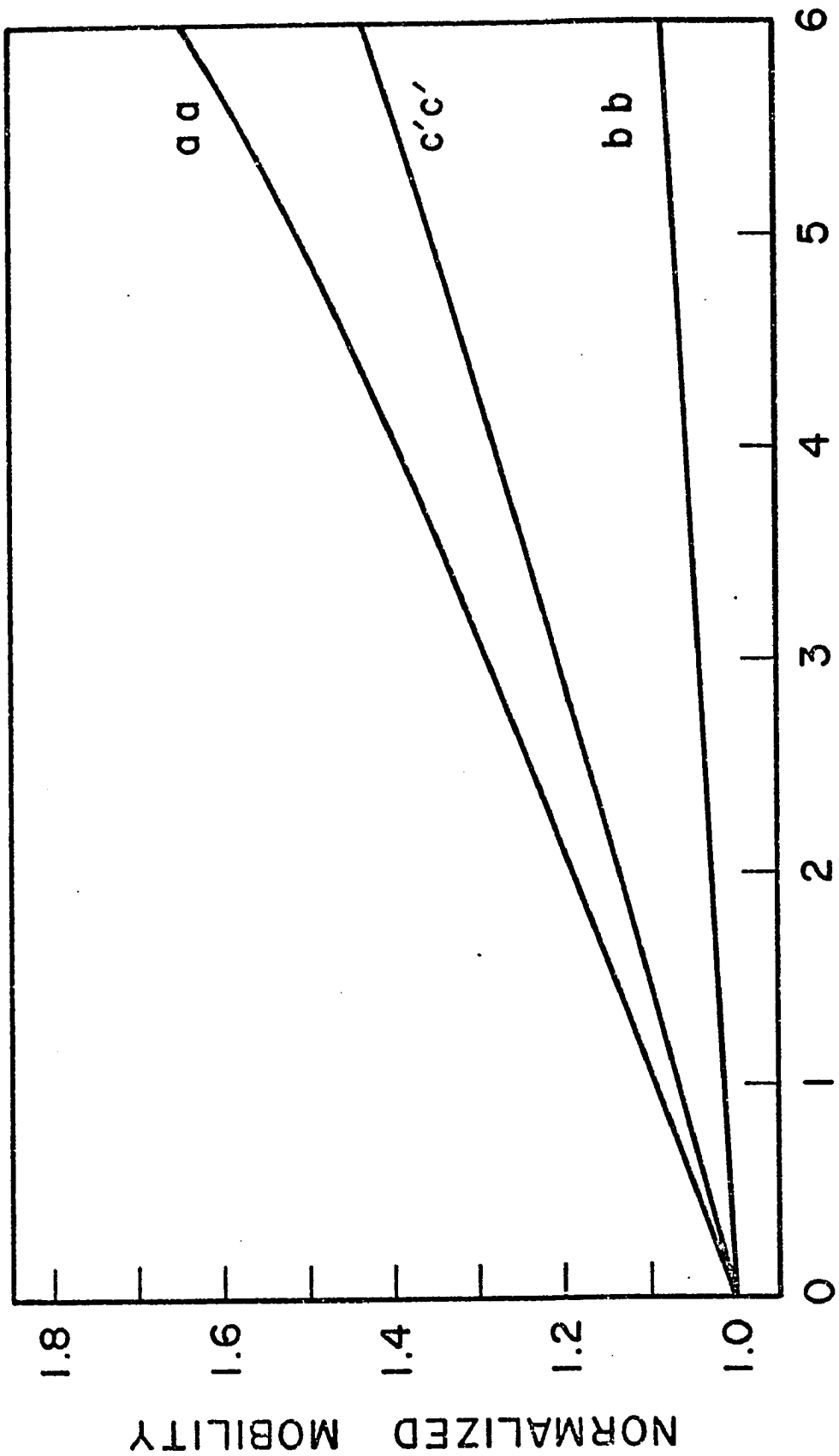

FIG. 4.8a

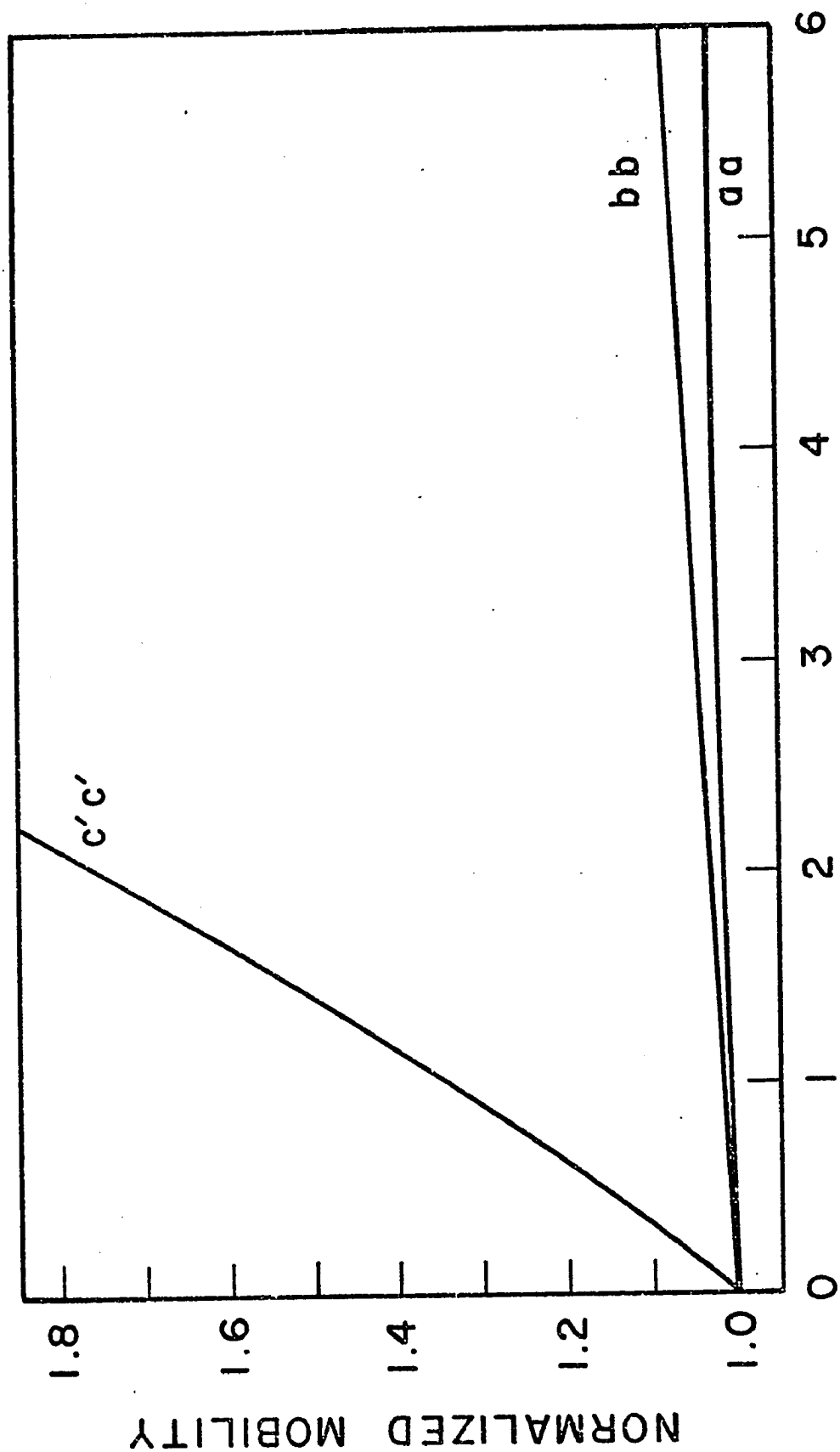

FIG. 4.8b

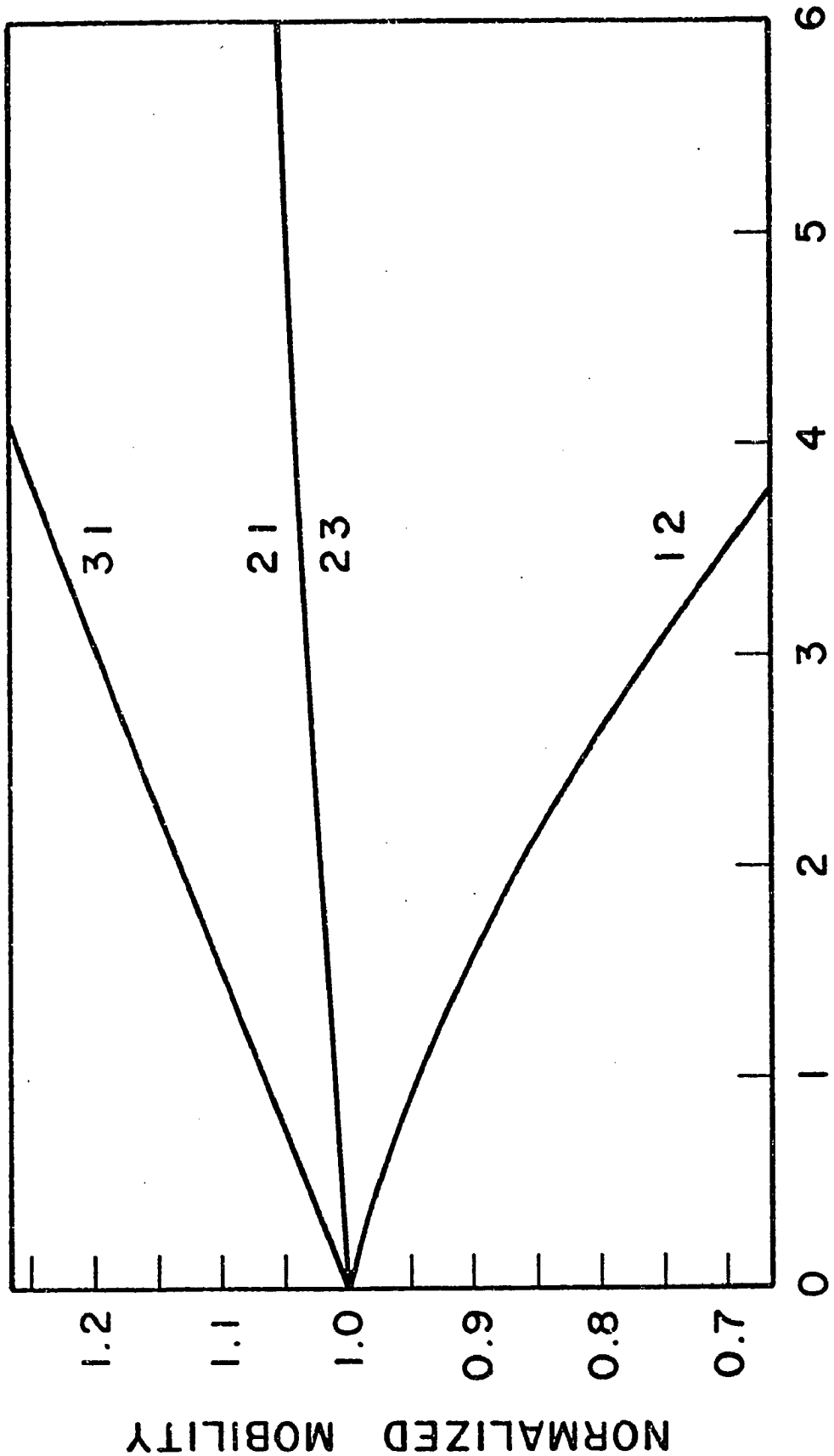

FIG. 4.9a

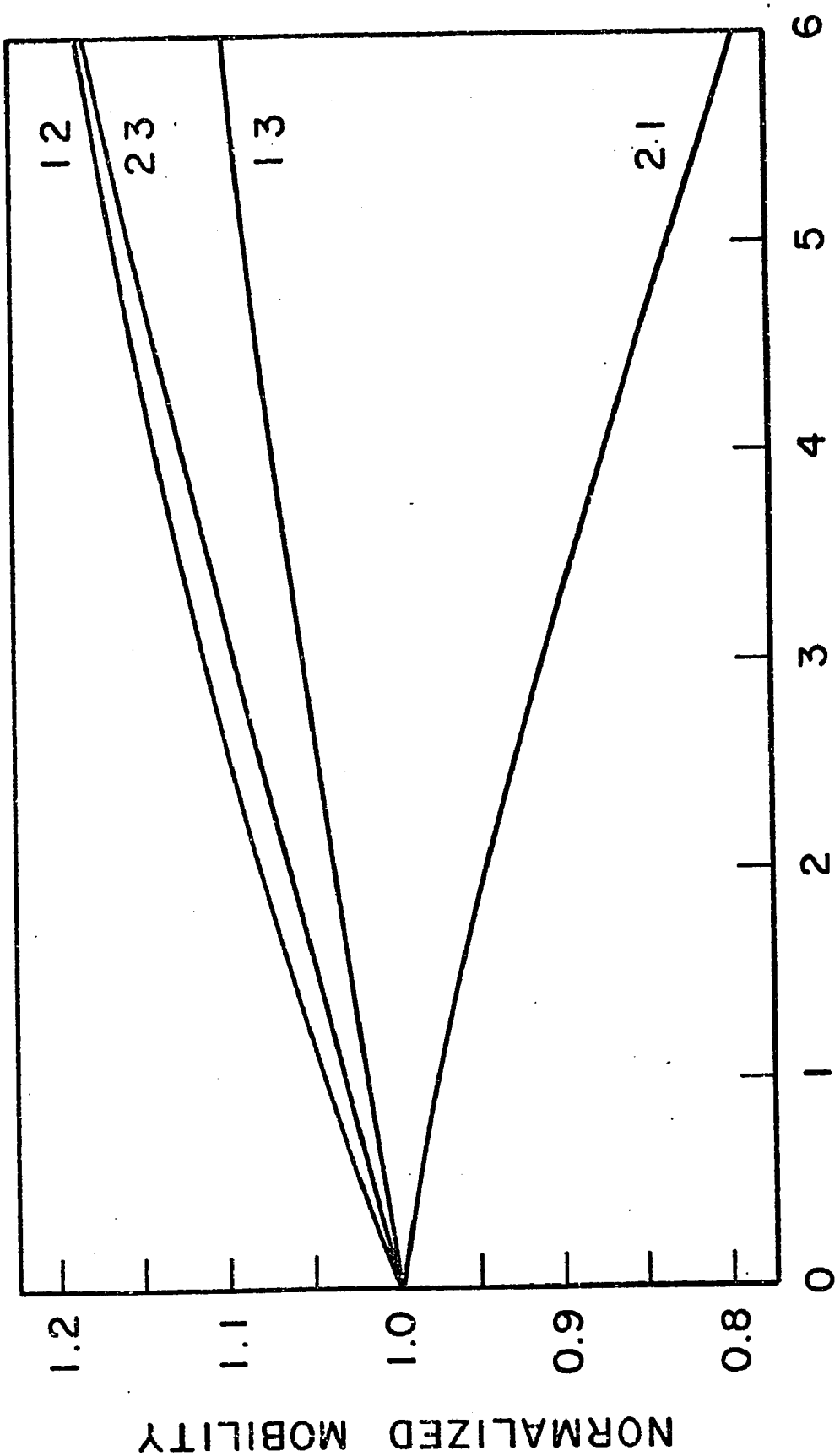

FIG. 4.9b

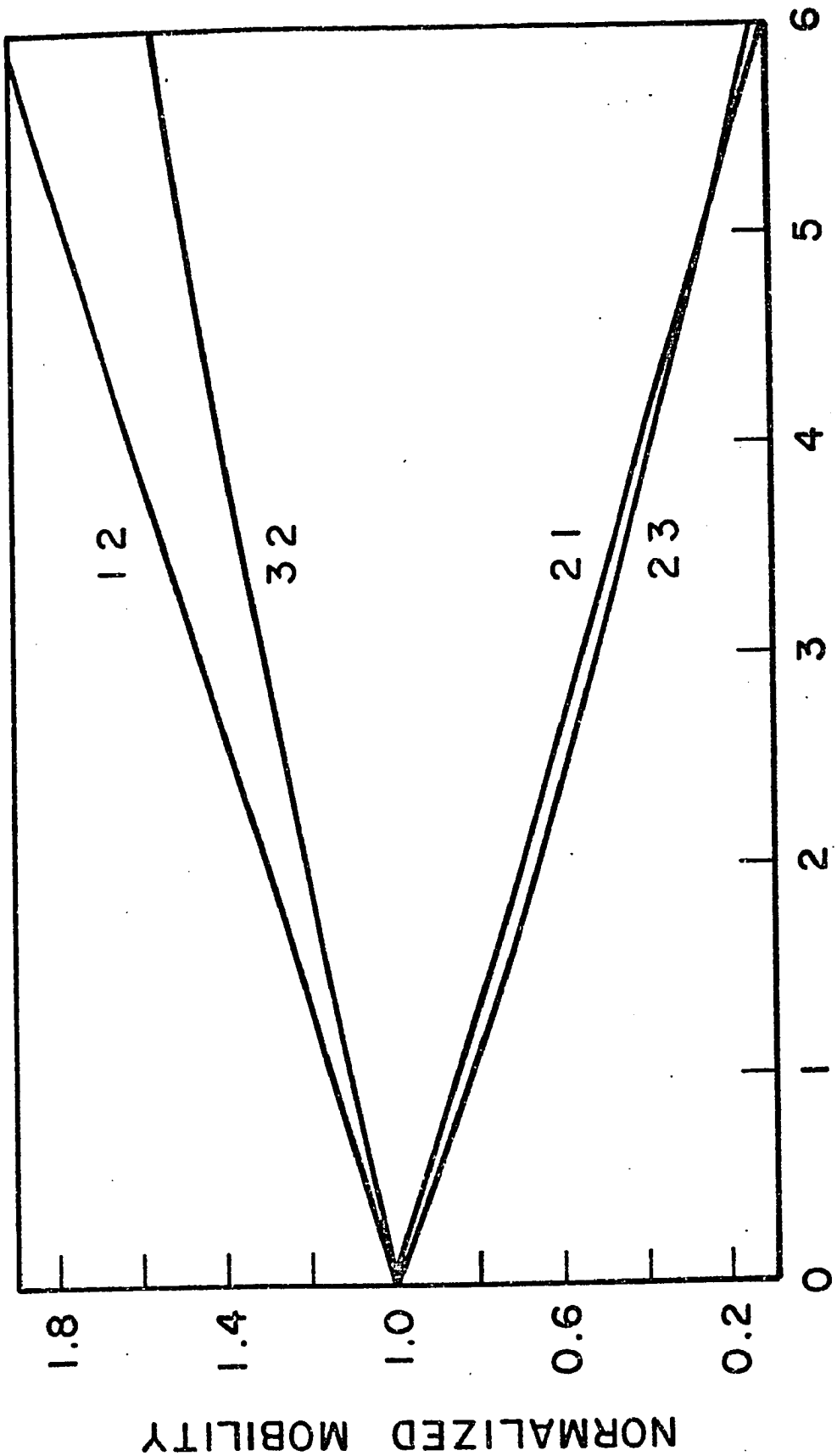

FIG. 4.10a

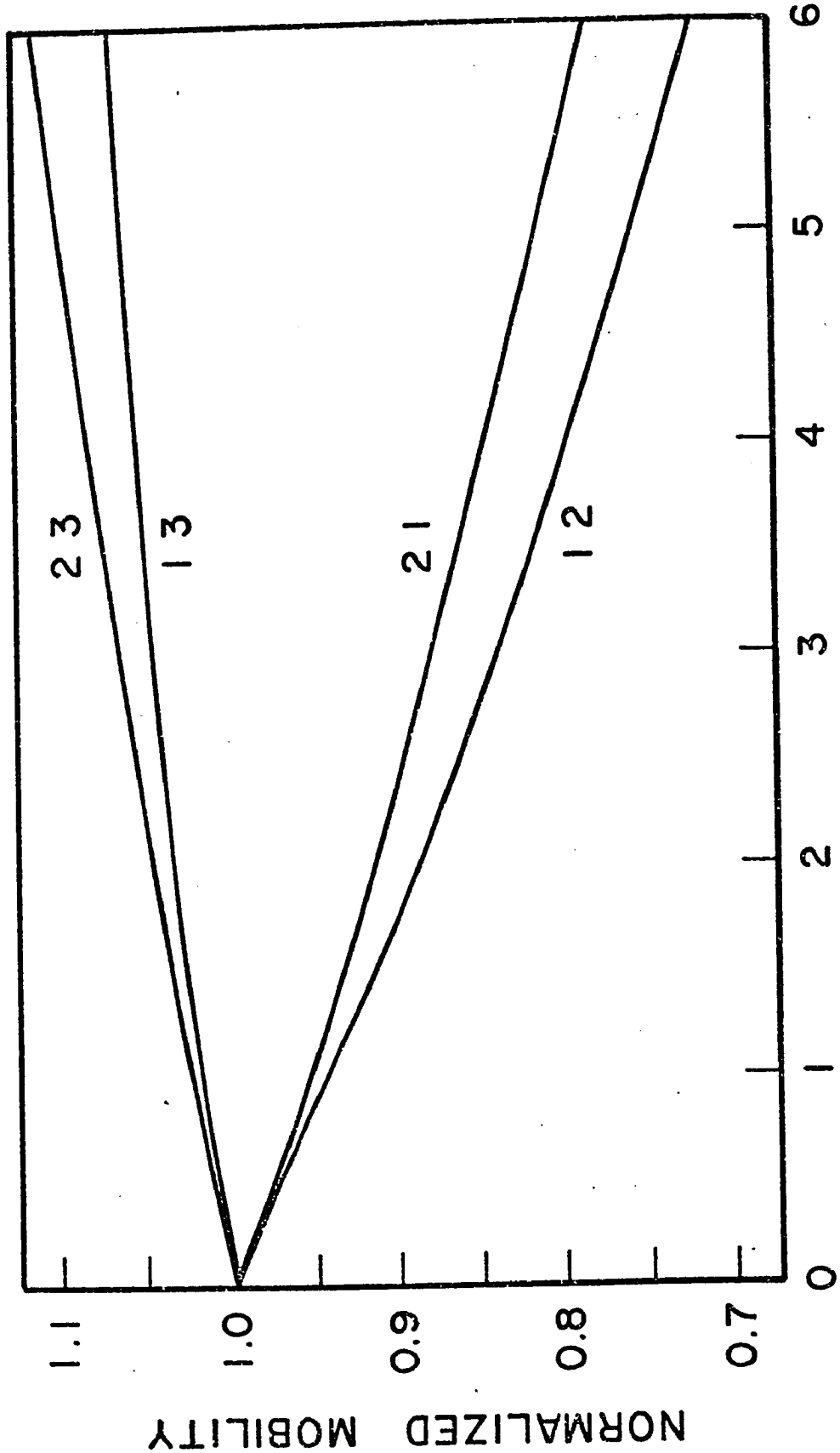

FIG. 4.10b

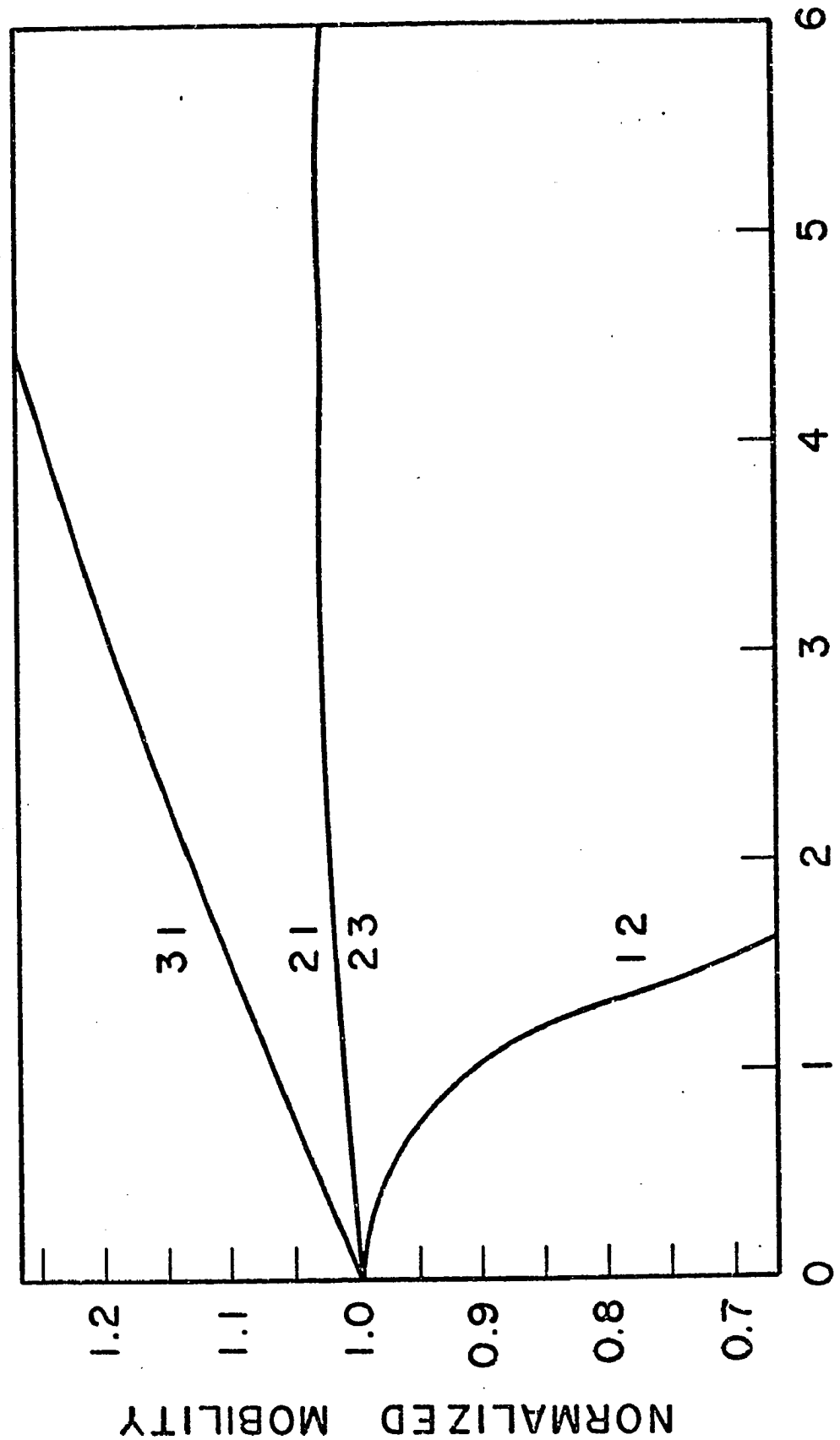

FIG. 4.11a

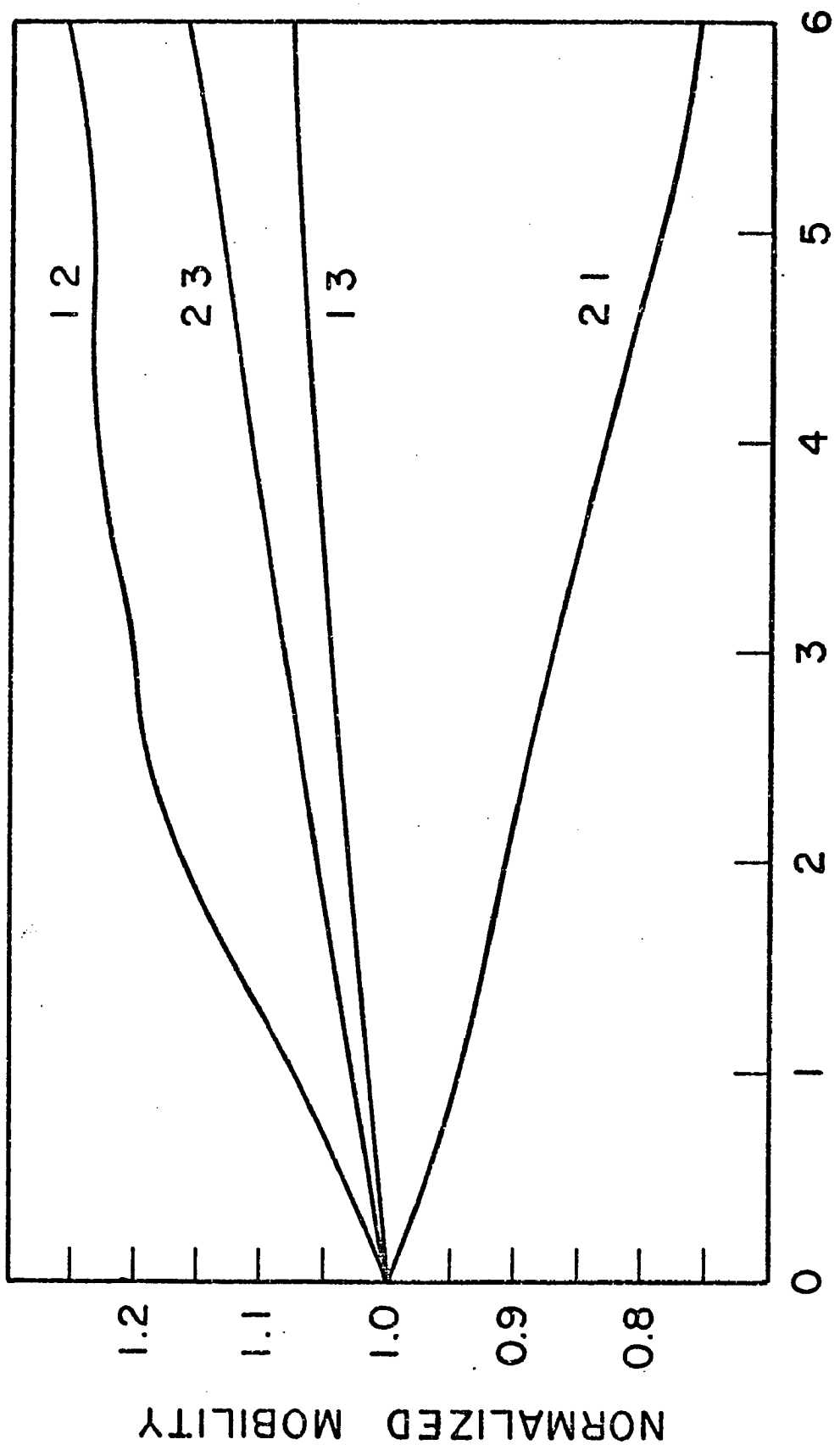

FIG. 4.11b

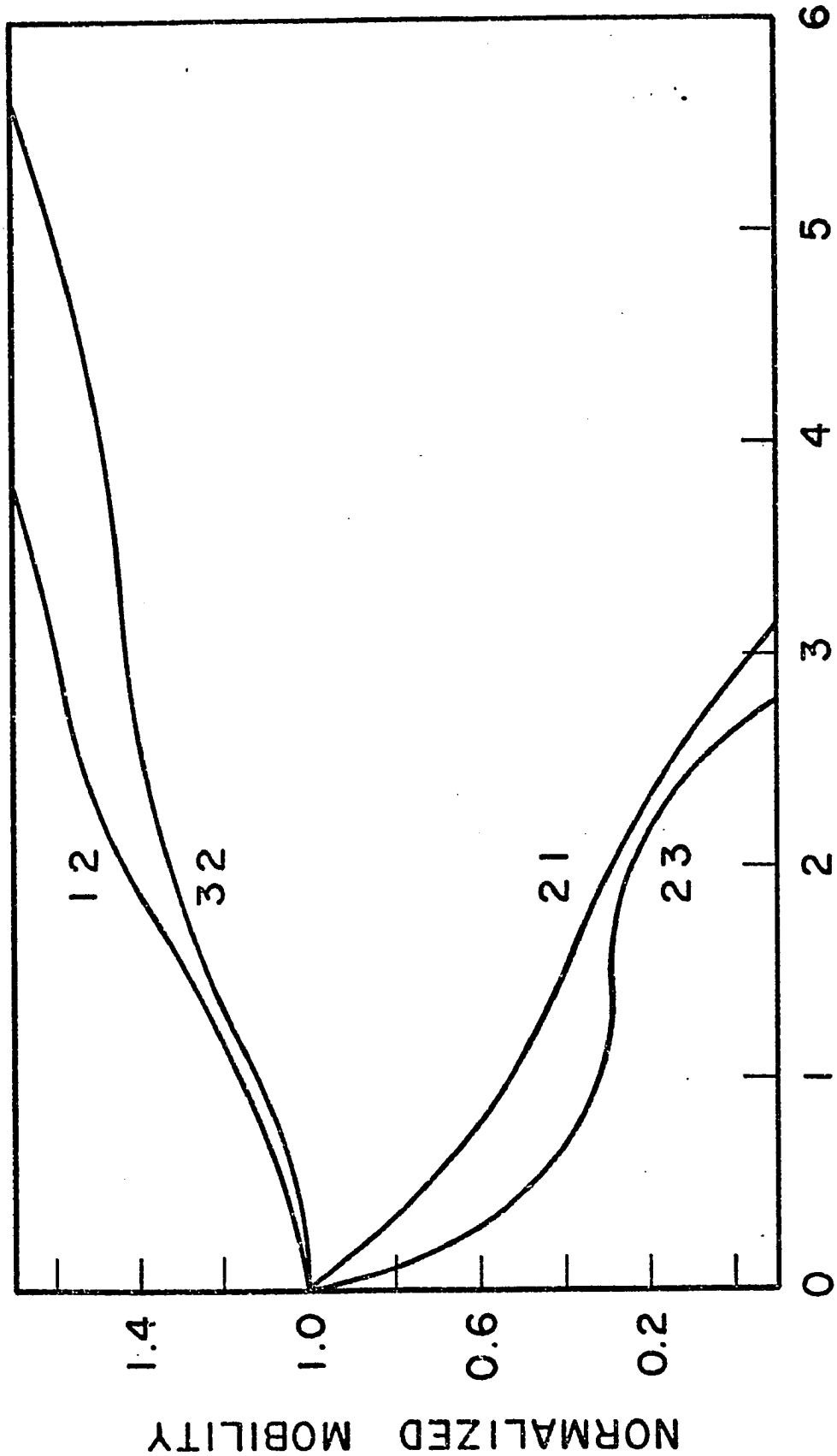

FIG. 4.12a

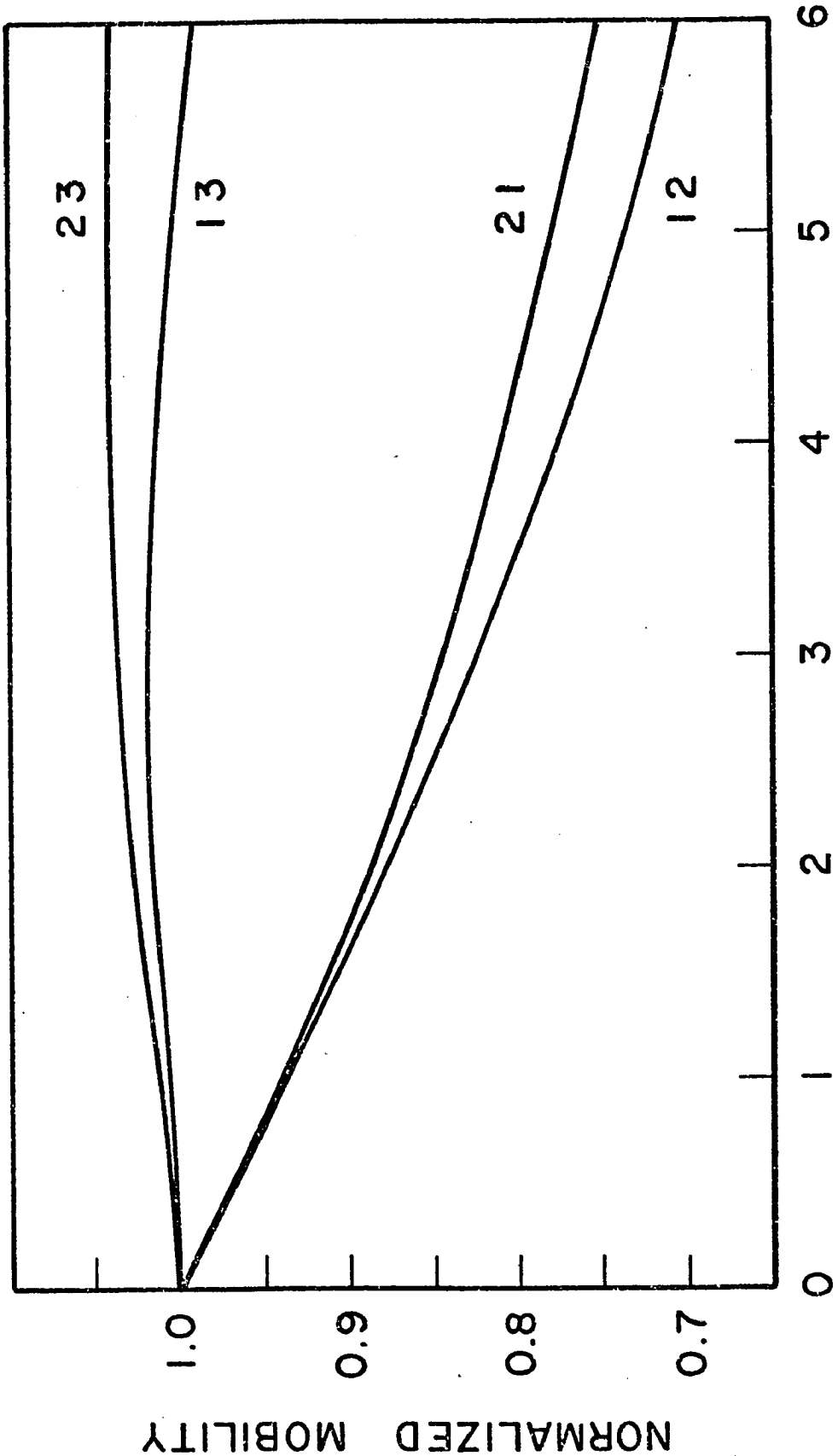

FIG. 4.12b

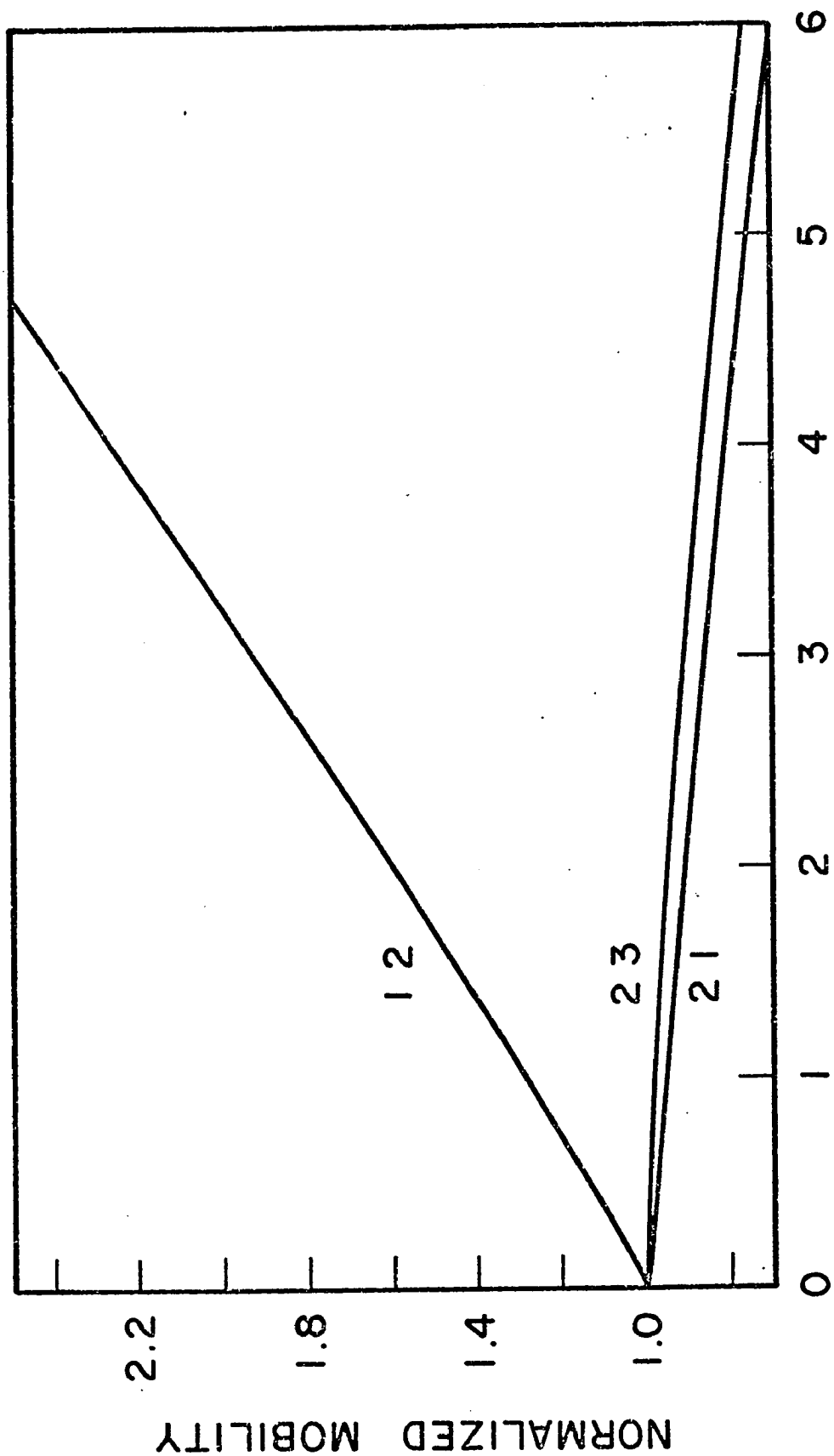

FIG. 4.13a

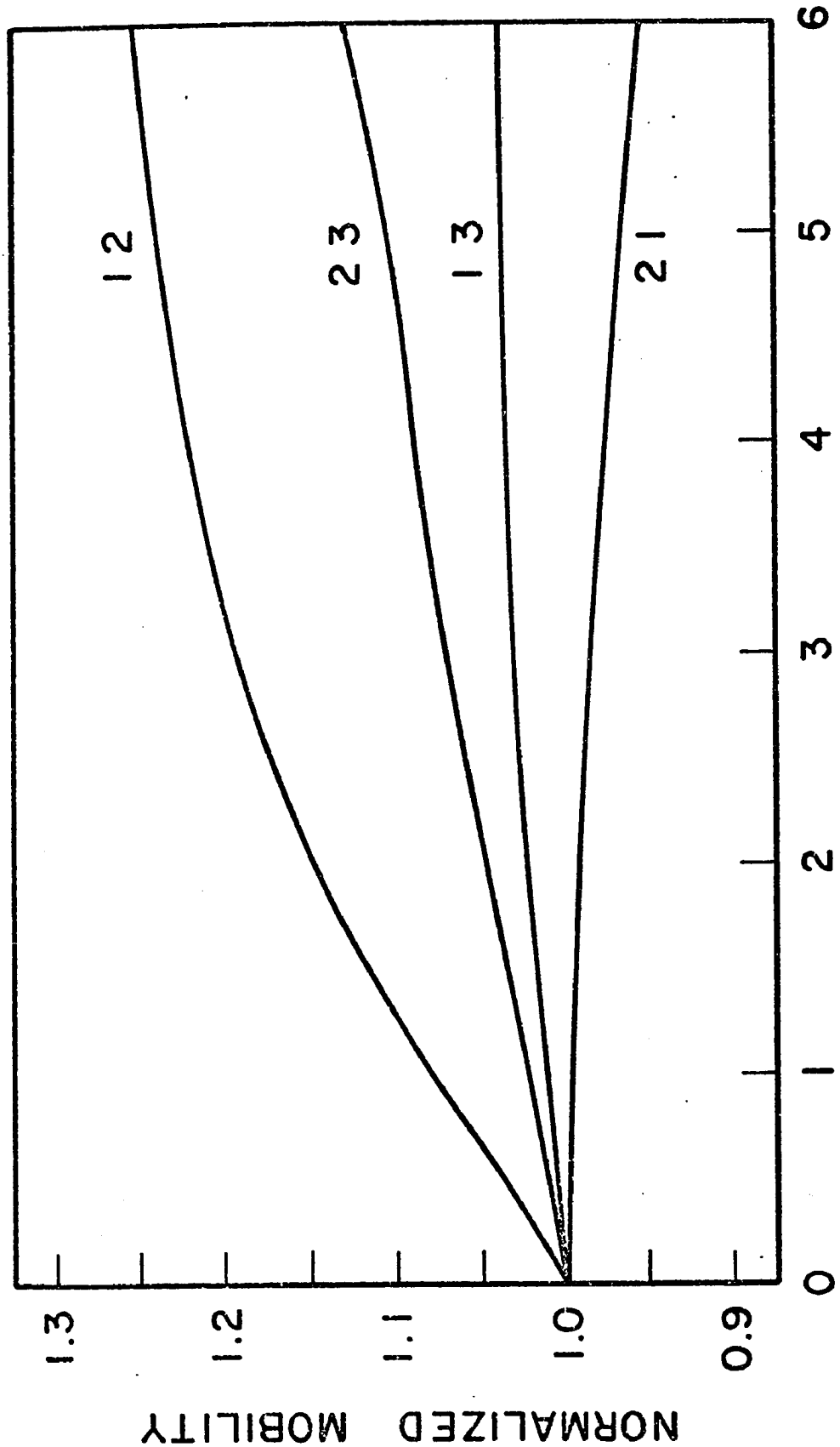

FIG. 4.13b

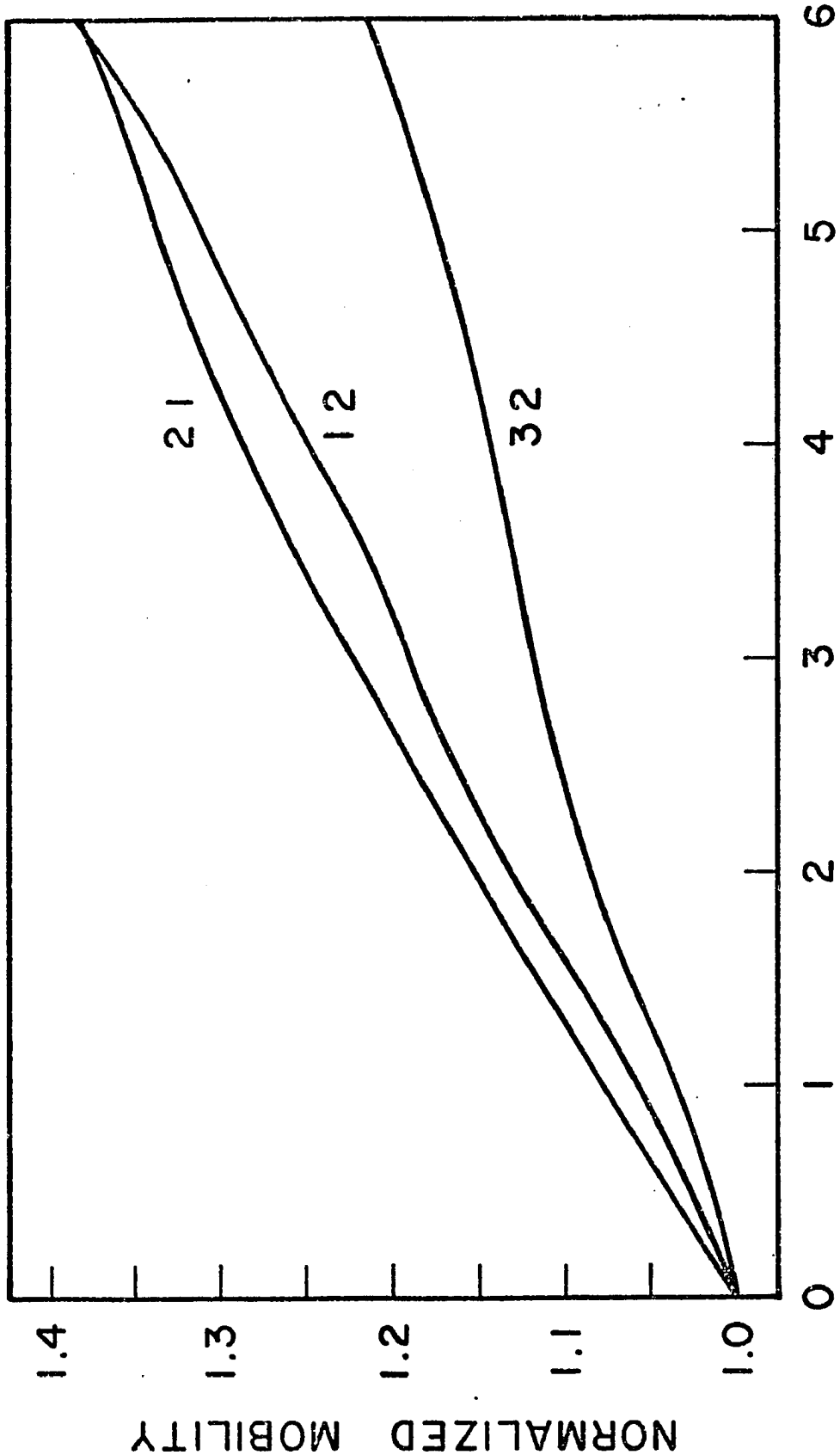

FIG. 4.14a

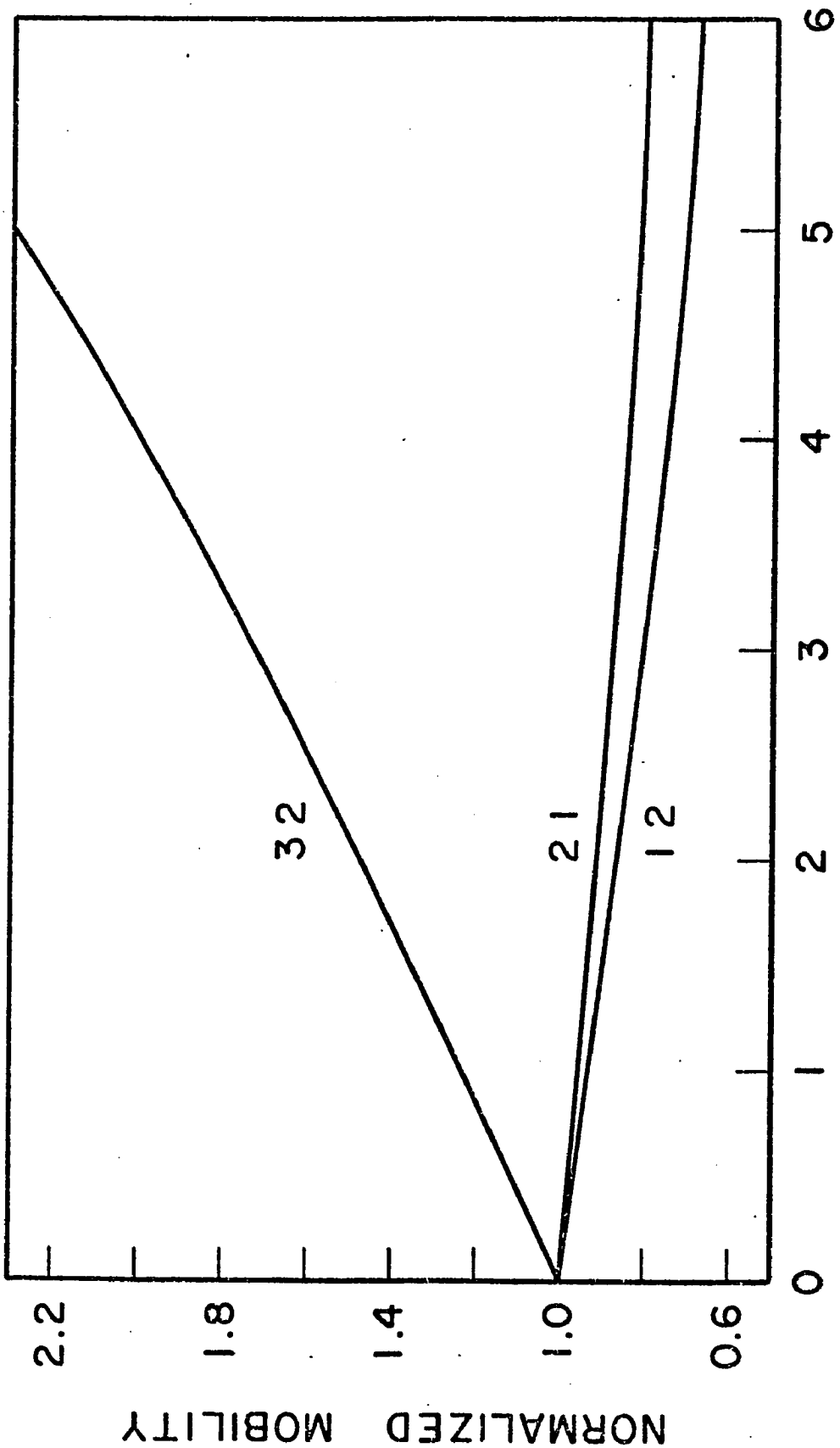

FIG. 4.14b

References - Chapter 4

1. W. Shockley, Electrons and Holes in Semiconductors, van Nostrand, Princeton, N.J., 1950.

2. O.H. Leblanc, Jr., J. Chem. Phys., 35, 1275 (1961).

3. G.D. Thaxton, R.C. Jarnagin and M. Silver, J. Phys. Chem., 66, 2461 (1962).

4. J.L. Katz, S.A. Rice, S.I. Choi and J. Jortner, J. Chem. Phys., 39, 1683 (1963).

5. O.H. Leblanc, Jr., J. Chem. Phys., 39, 2395 (1963).

6. L. Friedman, Phys. Rev., 133, A1668 (1964).

7. A.H. Wilson, The Theory of Metals, 2nd edn., Cambridge University Press, 1953.

8. J.M. Ziman, Electrons and Phonons, Oxford University Press, 1960.

9. A.C. Beer, Galvanomagnetic Effects in Semiconductors, Solid State Physics, suppl.4, (Eds. F. Seitz and D. Turnbull), Academic Press, New York, 1963.

10. H. Jones and C. Zener, Proc. Roy. Soc., A145, 268 (1934).

11. F.J. Blatt, Solid State Physics, 12, 199 (Eds. F. Seitz and D. Turnbull), Academic Press, New York, 1961.

12. C. Kittel, Introduction to Solid State Physics, 4th edn., p.69, Wiley, Inc., New York, 1971.

13. W. Mey and A.M. Hermann, Phys. Rev. B, 7, 1652 (1973).

14. M. Silver, J. Rho, D. Olness and R.C. Jarnagin, J. Chem. Phys., 38, 3030 (1963).

15. D.H. Spielberg, A.I. Korn and A.C. Damask, Phys. Rev. B, 3, 2012 (1971).

16. O.H. Leblanc, Jr., Private communication (1965) quoted in F. Gutmann and L.E. Lyons, Organic Semiconductors, p.259, Wiley, New York, 1967.

17. S.I. Kubarev and I.D. Mikhailov, Theor. Exp. Chem., 3, 265 (1967).

18. S.I. Kubarev and I.D. Mikhailov, Theor. Exp. Chem., 4, 134 (1968).

Chapter Five

Hall Effect in Naphthalene at High Pressures

1. Introduction

The only available high pressure data on the carrier mobilities of organics concern the drift mobility tensor of anthracene[1,2]. All previous work regarding Hall effect measurements in molecular crystals was done at atmospheric pressure. Most of it suffered from either a lack of completeness in that all possible orientations of the electric and magnetic fields were not considered, or from an inability to unequivocally determine the sign of the charge carrier being observed. Among the organics, anthracene was the most extensively investigated, while Hall mobility data for naphthalene were recently published by Spielberg et al[3]. A chronological review of the various methods of Hall effect measurements in molecular crystals is now presented.

Dresner[4] made a surface photo-Hall effect measurement in anthracene in which two-carrier effects were found to predominate; therefore, it was impossible for him to ascribe the Hall voltage to the Hall mobility of either carrier. More recently, and using hole injecting contacts along with weakly absorbed light, Dresner[5] was able to measure the Hall effect of holes in anthracene. However, he could not find an anomalous effect.

Delacote and Schott[6,7] measured the Hall mobility in anthracene using a split rear electrode arrangement and an incident pulsed light. One disadvantage of this method is that the Hall current is approximately 0.1% of the primary current so that the measurement involves the difference of two large quantities. A second disadvantage is the presence of the Frankevich effect[8].

Pethig and Morgan[9] performed a Hall measurement with the crystal unilluminated, and were thus unable to determine which injected carrier, or both, was responsible for their observations.

Toombs[10] using a low frequency a.c. phase sensitive method, measured the Hall effect with the magnetic field oriented along both the a or b directions. The charge carriers were photo-injected holes drifting along

the c' direction. However, no anomalous results were observed.

Smith[11], using a modification of the Redfield method[12], made photo-Hall measurements where the incident light was weakly absorbed. As a result, he may have observed both types of charge carriers.

Schadt and Williams[13] measured the Hall mobility of electrons in anthracene, using injecting electrodes with the crystal unilluminated. However, despite their precautions to avoid double injection, their results were spurious; also, no anomalous effect was observed.

Korn et al[14] and Spielberg et al[3] measured the Hall effect for anthracene and naphthalene, respectively. In both investigations strongly absorbed light was used, and the measurements were performed in the six different possible relative orientations of the electric and magnetic fields. Hall mobilities for hole carriers were measured for both materials, while electron mobilities were obtained only for naphthalene. Since the carriers were unambiguously known, the observed results could be analyzed for anomalous behavior.

2. Description of the Experimental Apparatus

The electrical system used to measure the Hall effect was similar to the one developed by Korn[15], except for some slight modifications introduced to accomodate the restrictions imposed by high pressure measurements. The high pressure system was assembled; it was essentially similar to the one shown in fig. 2.7 , except for the sample containing vessel. A high pressure manganin gauge was also developped.

2a. The Manganin Gauge

This is a secondary gauge which uses the variation in resistance of a manganin wire for measuring the pressure. Manganin is a convenient alloy because of its linear rate of increase of resistance with pressure ($\sim$ 0.4 Ω/kb up to 13 kilobars) and also for its very low temperature coefficient of resistance[16].

The cell, shown in fig. 5.1 , is made out of fully maraged Vascomax 350 CVM for increased strength ($\sim$ 360,000 psi). The gauge coil itself is of double silk-covered manganin wire 0.005 in. in diameter, and about 25 ft long, giving a resistance of approximately 180 ohms. The wire was wound non-inductively on itself into a coreless toroid of about 0.5 cm in diameter. The winding was done on a separate arbor, so mounted that the coil

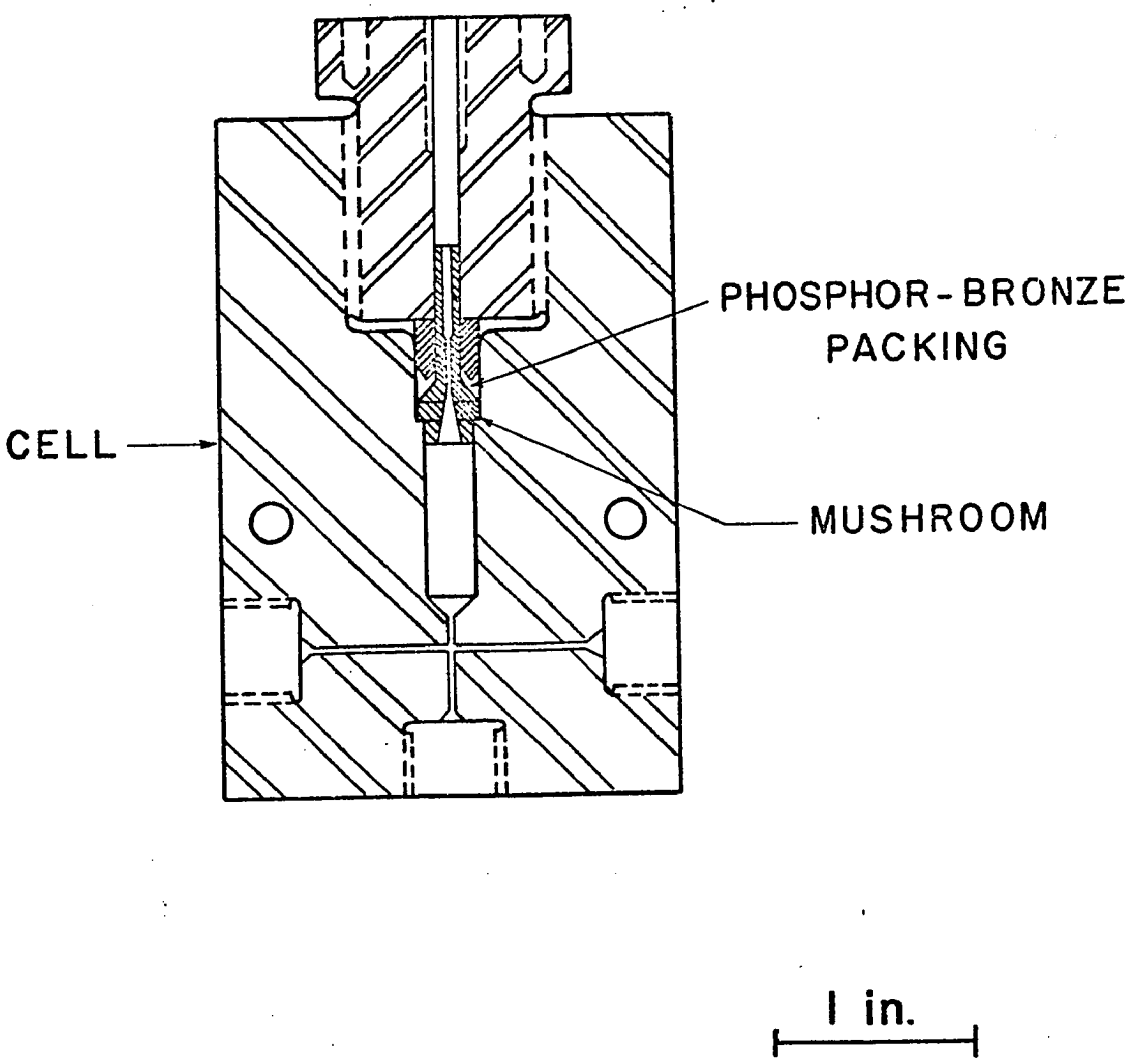

FIG. 5.1

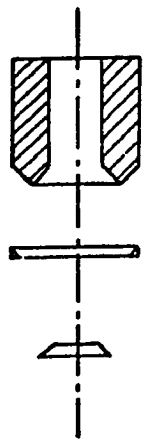

(c)

(b)

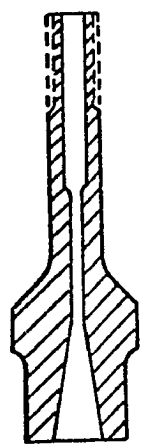

(a)

FIG. 5.2

could be readily pushed off after the winding was completed. The section of the toroid was made to retain its shape by covering it with a soft tissue slightly wetted with paper glue. The two ends of the wire were then soldered to the mushroom (Vascomax fully maraged), shown in fig. 5.2a , and to an insulated steel electrode in the shape of a rod having a cone at the middle of its length, shown in fig. 5.2b . The insulation between the cone and the mushroom was provided by means of a carefully fitted thin conical shell of delrin, shown shaded in fig. 5.2b . The rest of the rod was coated with a layer of General Electric insulating varnish (# 7031). The resistance of the manganin coil was measured with a standard Wheatstone bridge having an arm's ratio of 10 to 1.

To seal the gauge, a teflon and phosphor-bronze packing (shown in fig. 5.2c) was fitted on the outer cone of the mushroom (principle of the unsupported area). The seal between the rod and the inner cone of the mushroom was provided by the same delrin shell used for insulation. This was carried out by tightening the nut (thus crushing the teflon and phosphor-bronze packing), and then bringing the pressure in the system to approximately 1 kilobar. The body of the cell was then moderately heated (with a heat gun), while the pressure was being slowly increased in order to soften the delrin shell and allow it to flow, until no leak could be detected. The gauge was satisfactorily tested up to a pressure of 9 kilobars. Finally, the manganin gauge was aged to eliminate the wandering of the zero, and then calibrated against a Bourdon spring gauge.

2b. The High-Pressure Cell

The high-pressure cell, shown in fig. 5.3, was made out of beryllium copper (# 25 alloy). The material was chosen because of its non-permeability and strength, which was brought up to 176,000 psi by means of heat treatment to 600 °F for three hours; its hardness was R.C. 37 .

The cell had two optically flat sapphire windows (c-axis within ± 3°), 0.5 in. in diameter and in thickness, purchased from Insaco; these allowed the UV radiation to fall upon the sample. Window A had a hardened beryllium copper seat (fig. 5.4a), while window B was pressed against a push-piece (fig. 5.4b), also made out of hardened beryllium copper. The two windows were kept in place by means of a hardened beryllium copper spring (fig. 5.4c), 0.5 in. outer diameter and 0.35 in. inner diameter. The spring, which also

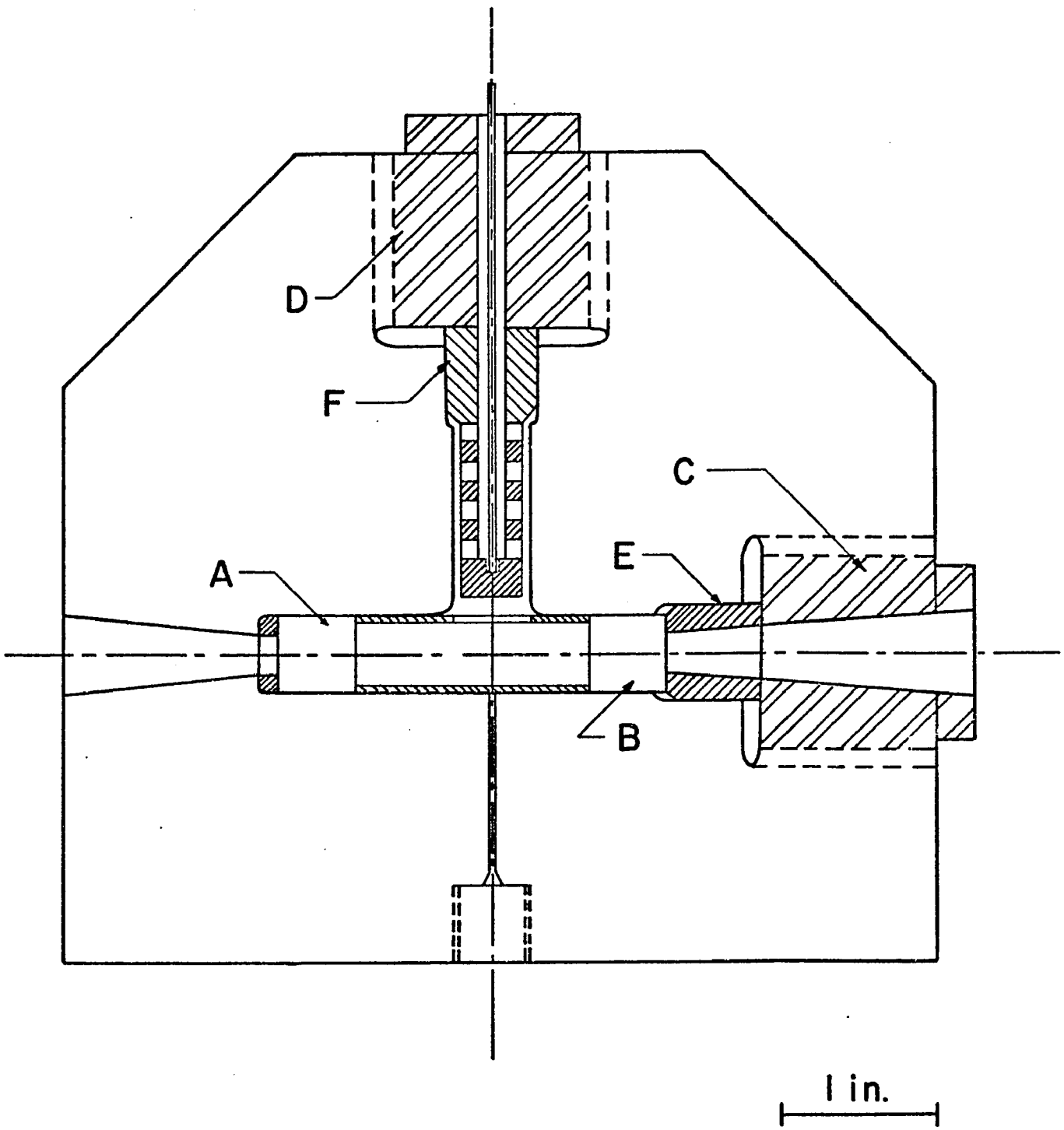

FIG. 5.3

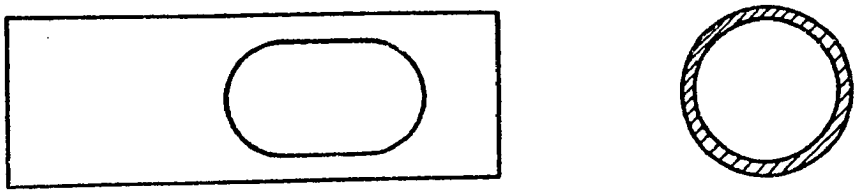

(c)

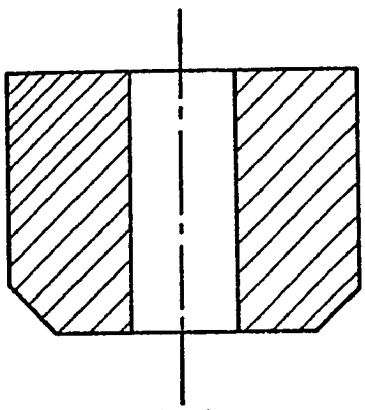

(b)

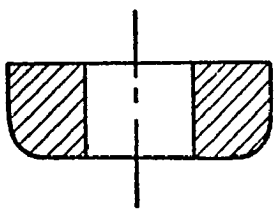

(a)

FIG. 5.4

supplied the initial preloading on the windows, had an 0.5 in. x 0.375 in. slot; the position of the latter was such that when plug C was tightened, the center of the slot fell exactly on the center line of plug D. This allowed the sample holder (fig. 5.6) to fit easily inside the spring.

The sample holder was supported by the stack, shown in fig. 5.5 . The latter consisted of four lead rings and an end-piece to which a support was welded. All metallic parts were electrically insulated from each other by means of four lucalox rings (0.375 in. outer diameter, 0.125 in. inner diameter and 0.125 in. thick) purchased from Insaco. The lead rings and end-piece were 0.375 in. in diameter and made out of hardened beryllium copper. The upper ring was electrically insulated from push-piece F by means of a fifth lucalox ring.

Each lead ring had two teflon insulated wires welded to it: one was soldered to its outer surface and went directly to one of the electrodes on the sample's surface inside the cell, while the second one was soldered to the inner surface of the ring and connected it to the Hall effect measuring equipment outside the cell. Another teflon insulated wire was welded to the outer surface of the end-piece, and used for connection to the transparent electrode of the sample holder. The five wires connected to the outer surfaces were thus "seeing" the high pressure, while the four inner wires were at atmospheric pressure. The whole stack, including push-piece F, was held together by means of a teflon insulated steel rod (0.047 in. in diameter) threaded into the end-piece on one side, and into a copper rod (diameter 0.25 in.) on the other side. The copper rod was electrically insulated from push-piece F by means of a delrin ring. The four inner teflon insulated wires, along with the copper rod, thus constituted five leads which were connected to the Hall effect measuring equipment.

To prevent leaks from occuring, a large number of surfaces had to be carefully lapped until all machine marks were removed and a good degree of flatness was attained. The surfaces that were lapped included both faces of all lead rings, the upper surface of the end-piece, the faces of push-pieces E and F that were in contact with the sapphire window and the lucalox ring respectively, as well as their conical surfaces. Also, both surfaces of the window seat were lapped, in addition to the area of the cell block in contact with it. The latter operation was carried out by means of a cylindrical rod 0.5 in. in diameter, made out of cast iron. All lap-

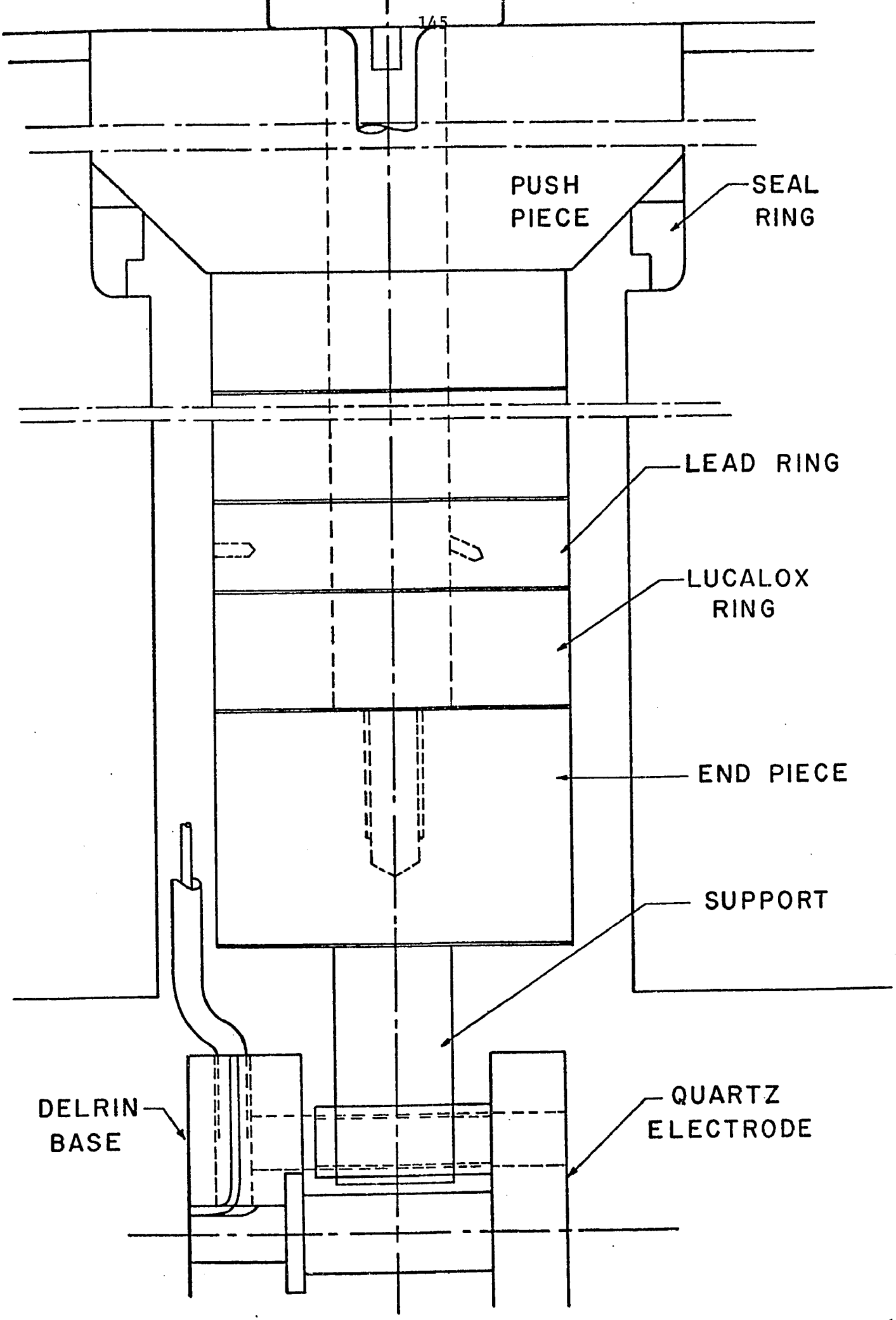

ping operations, except for the last one, were performed on a flat block made out of cast iron, and involved the use of lapping compounds in successively decreasing sizes of grit (from 12 to 4 microns). This was a long and painstaking process in which the last polish was carried out with Linde A, a compound obtained by mixing alumina powder (2-3 microns in size) and liquid soap.

However, despite all the precautions taken, the lapped surfaces still showed innumerable small scratches, and leaks developped upon pressurizing the cell. Therefore, metallic shims of various thicknesses had to be used on the lapped surfaces. It was found that copper shims, 0.002 in. thick, were suitable for the optical part of the cell; leaks from this part could be prevented by using three shims on each face of the window seat, and four shims between sapphire window B and push-piece E. On the other hand, lead gaskets, 0.002 in. thick, proved sufficient to stop any leak from the stack assembly.

Finally, the last source of leakage from the cell was eliminated by means of two seal rings (non hardened beryllium copper), pressing against the conical surfaces of the two push-pieces, E and F (principle of the unsupported area).

2c. The Crystal Holder

The crystal holder, shown in fig. 5.6, was mounted at the lower end of the stack and held in position by means of a beryllium copper support welded to the end-piece. It consisted essentially of a delrin base and a transparent electrode, both circular in shape, held together by means of eight 0-80 brass screws and four brass sleeves. The transparent electrode was made out of tin-oxide coated quartz, and had four ultrasonically drilled holes. Each hole cleared an 0-80 screw which was then threaded into one of the brass sleeves; another 0-80 screw, going through the delrin base, was threaded into the opposite end of the sleeve. All four screws going through the base were spring loaded (phosphor-bronze springs 0.085 in. in diameter and 3 mm long), thus allowing for some tightening on the crystal to insure good electrical contact without breaking the sample.

The dark electrode consisted of a copper platform snug-fitted into the delrin base, and connected to one of the lead rings of the stack. The three other teflon insulated wires, soldered to the outer sides of lead

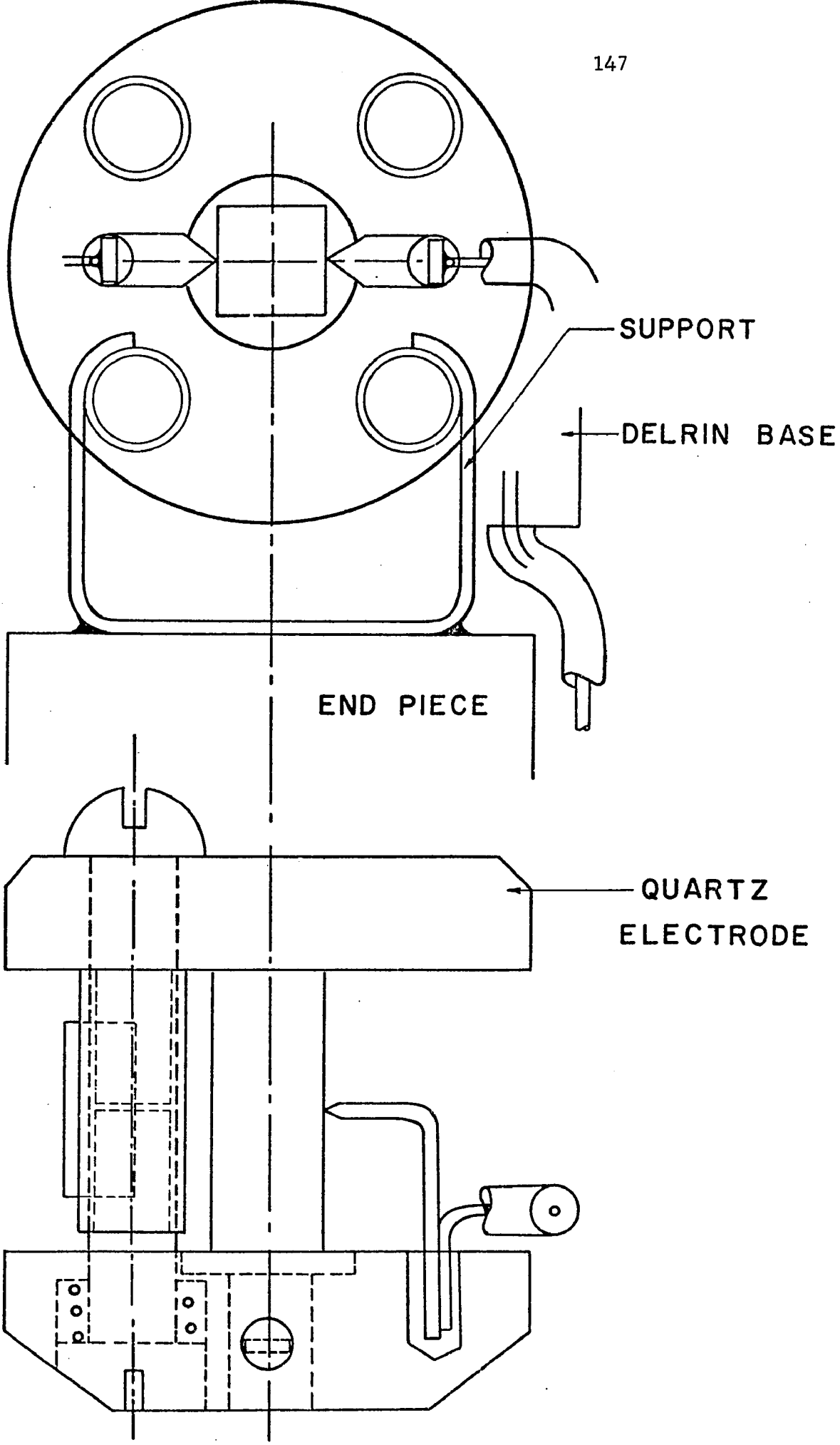

rings, were passed through separate holes in the delrin base and used as electrical connections for the two Hall probes and the guard ring. The fifth wire, soldered to the end-piece, provided the electrical contact to the tin-oxide coated quartz electrode. This was accomplished by pasting the wire to the edge of the coated surface, using Dupont # 4817 silver conducting paint. A layer of epoxy glue was then spread over the connection and allowed to dry overnight.

Because of the small sizes involved, the crystal holder had to be carefully cleaned in order to minimize leakage currents. This was done before mounting the sample, and consisted in thoroughly washing the delrin base with acetone. Its surface was then dried up and examined under the microscope for possible traces of silver paint.

The sides of the base and of the transparent electrode had to be chopped off, in order to allow for smooth fitting of the sample holder into the spring (fig. 5.4c). The length of the crystal holder was 0.43 in. and its diameter 0.35 in. As a result of this miniaturization, the sizes of crystals used were critical. Typical sample dimensions were 0.170 in. x 0.115 in. x 0.070 in. The crystal was brought down to the required size by polishing on a soft tissue soaked with ethyl alcohol. A guard ring was painted on the sample as near to the illuminated electrode as possible, using the Dupont # 4817 silver paint thinned with butyl acetate. The dark side of the crystal was coated with a thin layer of the same paint, in order to insure as uniform a field as possible in the sample, and for good electrical contact with the copper electrode. The Hall probes were made out of copper wire (0.002 in. in diameter), bent at one end in the shape of a very small loop. The loop was dipped into the Dupont # 4817 silver paint, and pasted on the surface of the crystal midway between the guard ring and the dark electrode.

Finally, a mask of black electrical tape was placed on the quartz electrode, to prevent the sides of the crystal from being illuminated. This insured against the generation of surface carriers by the guard ring.

2d. The Optical System

A 1000 watt xenon lamp, Hanovia 976-C1 , model # C-45-35-51 , from Oriel Optics Corporation, was used to illuminate the sample. In a crystal of high purity, charge carriers must be injected, since the conduction

is not intrinsic[17,18]. The lamp was used to photo-inject charge carriers into the naphthalene. A heat filter was placed in the beam to reduce the amount of infra-red radiation getting to the crystal. This was taken as a precaution against sublimation of the samples. The heat filter was a quartz container, about 0.5 in. thick, filled with a solution of copper sulphate in distilled water. It is prepared by taking a saturated solution of copper sulphate and dilute it one part to four with distilled water. The beam was then focused to the specimen's surface by means of a 20 cm focal length converging quartz lens. A block diagram of the optics is found in fig. 5.7 .

2e.The Electrical System

A block diagram of the circuit used for the Hall effect measurement is shown in fig. 5.8 .

In practice, it was not possible to paste the Hall probe exactly at the position of the zero equipotential surface of the crystal. Therefore, its voltage had to be balanced out by using a bucking potentiometer (see fig. 5.9).

2f.The Vibrating Reed Electrometer

A Cary vibrating reed electrometer was used to measure the potential of each Hall probe relative to the ground; the two probes were thus electrically independent. The input impedance of the electrometer exceeded 10^{16} ohms, and therefore did not load the crystal. Another useful property of this instrument was that compensating potentials for Hall probe misalignment voltage could be applied without destroying the high input impedance or adding to the circuit capacitance. Low circuit capacitance was necessary to reduce the time constant of a Hall voltage measurement.

A vibrating reed electrometer, with a 10^{12} ohms resistor across its input, was used as an ammeter to measure the photocurrent.

Because of the very high circuit resistances and the low currents involved, leakage currents were a major source of concern. Special care was taken to keep all insulators as clean as possible,,to prevent currents from leaking across the insulation.

2g.The Magnet

The magnet used was a conventional electromagnet, Magnion model L-128A ,

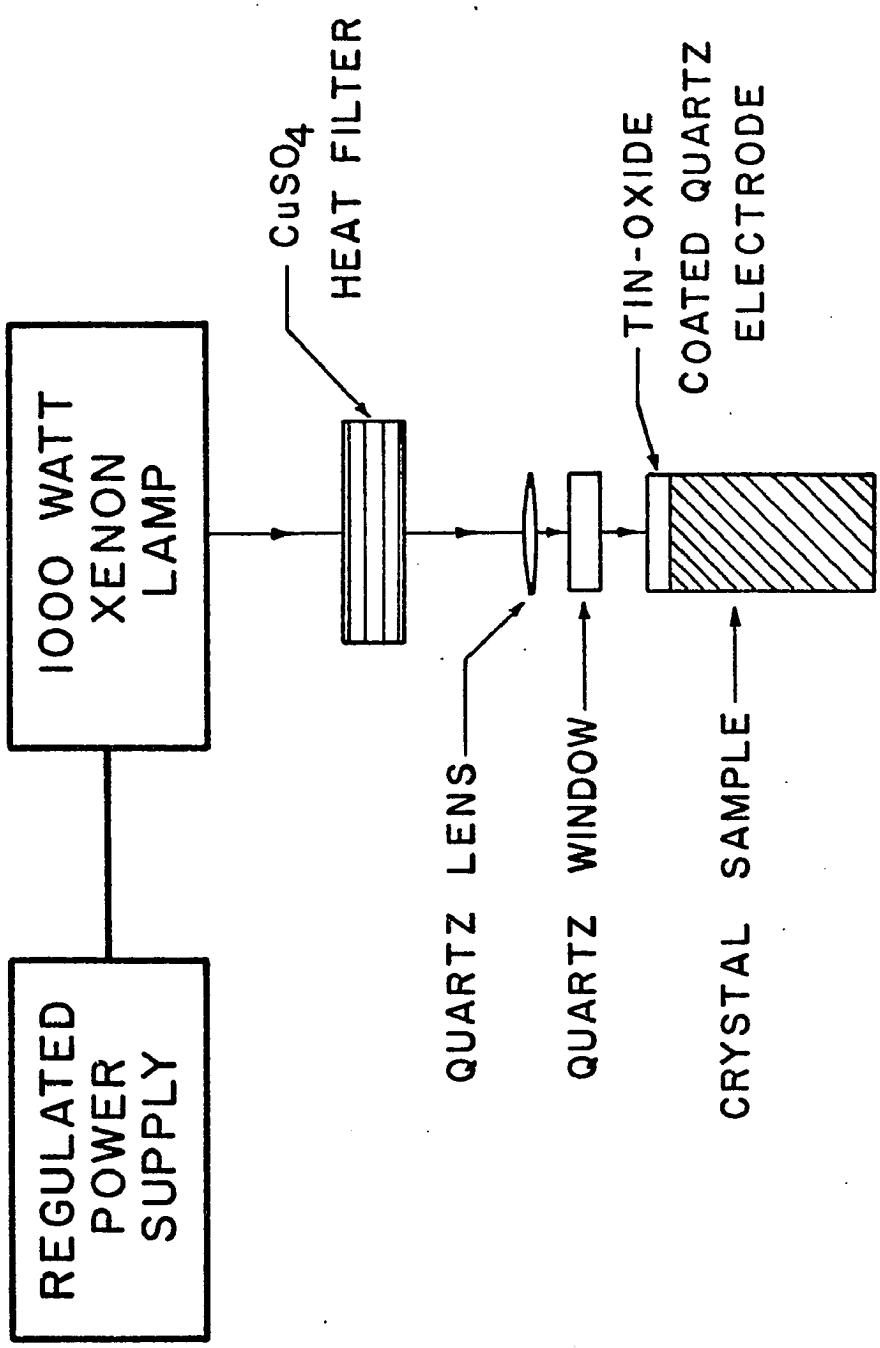

FIG. 5.7

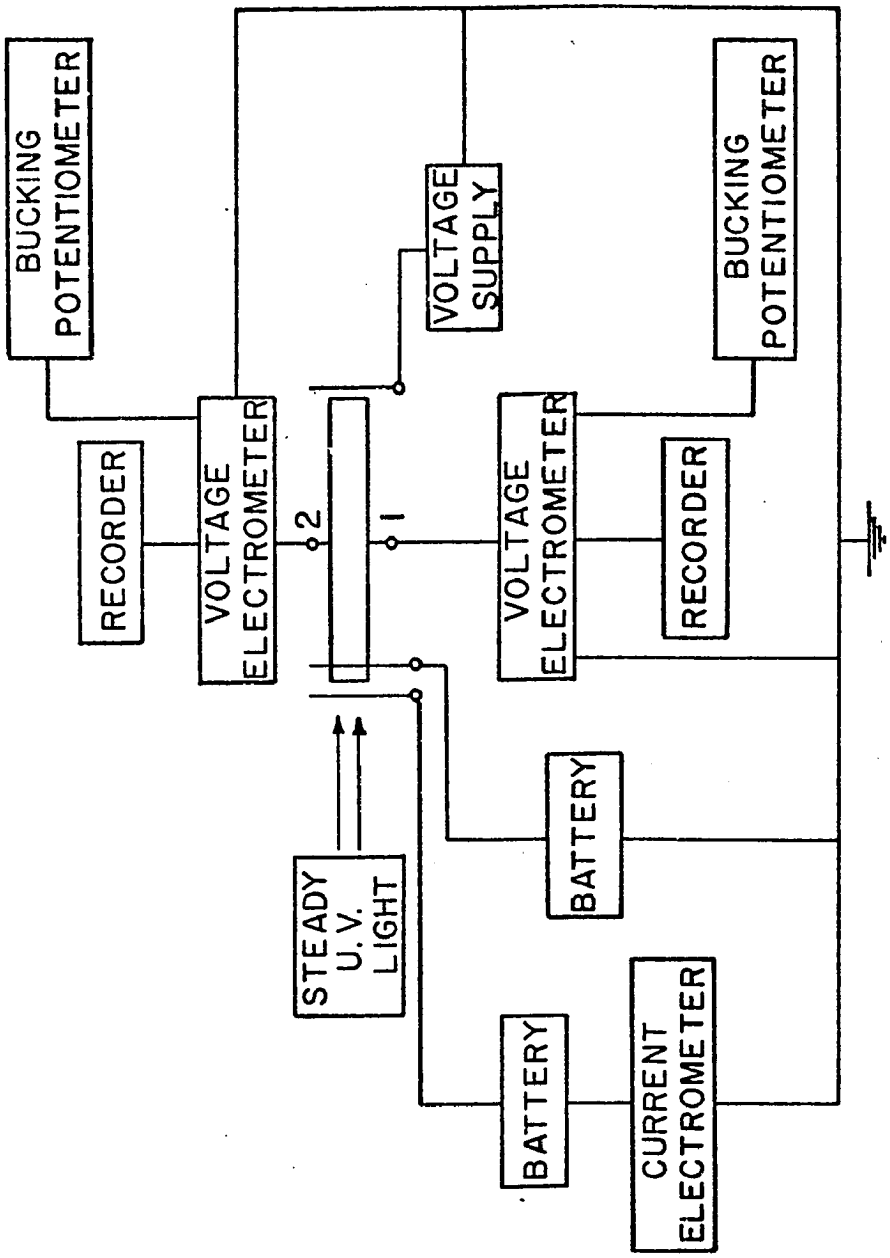

1 AND 2 ARE THE HALL PROBES

FIG. 5.8

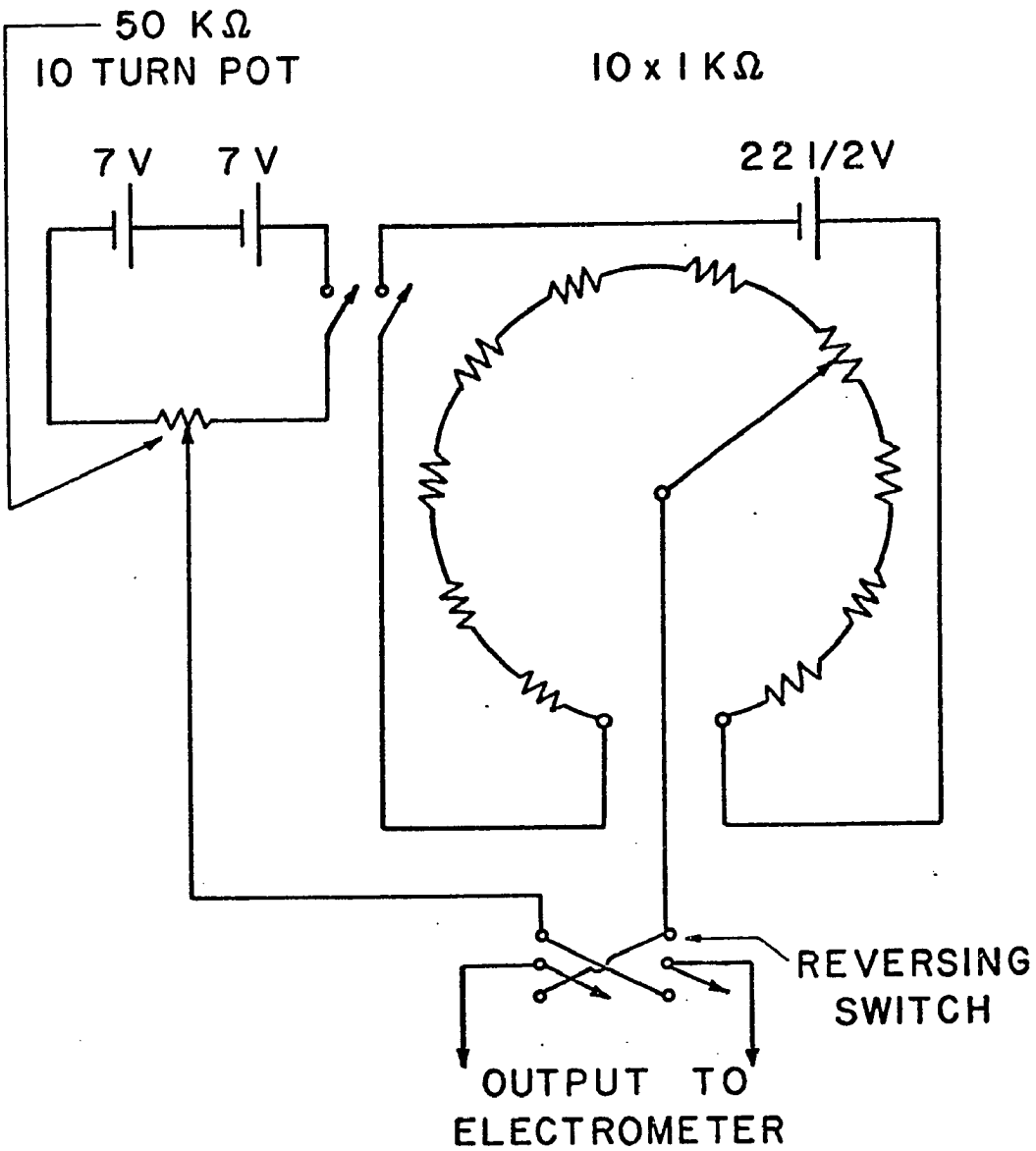

FIG. 5.9

manufactured by the Ventron Instruments Corporation. Its power supply was a model HSR-1365B from the same manufacturer, regulated by a model FFC-4 Field Regulator, also made by the Ventron Instruments Corporation. A continuously variable magnetic field, from 0 to 20 kilogauss, was obtained from such a system. The magnet had a two inch pole gap.

3. Computation of the Hall Mobility from the Measured Voltage

The computations follow the analysis due to Helfrich[19], Mott and Gurney[20] and adapted by Spielberg[21].

The geometry of the crystal sample is shown in fig. 4.1 ; the signs of the voltages correspond to hole conduction. For electron conduction, the signs are reversed. The directions of the various fields are also indicated on the diagram. The photo-injecting electrode (V_L) is located at $x = -\ell/2$, while the dark electrode (V_D) is located at $x = +\ell/2$, where ℓ is the sample length.

In the elementary theory of the Hall effect, V_H (the Hall voltage) would equal $2V_m$, where V_m is the measured voltage with respect to ground potential of one of the Hall probes (corresponding to V_1 or V_2). However, the real problem must include the effects of the finite dimensions of the sample, as well as the fact that the photo-injecting electrode forms an ohmic contact leading to space charge limited currents (SCLC). The latter can also be significantly reduced by carrier trapping. As a result, the internal field E_x is not equal to E_o , where

$$E_o = \frac{V_L + V_D}{\ell}$$

The primary electric field will now be determined.

3a. Determination of the Primary Electric Field, E_x

For convenience, a coordinate system x', y, z is chosen such that:

$$x' = x + \ell/2$$

The illuminated electrode is then at $x' = 0$ and the dark electrode at $x' = \ell$.

Assuming only steady-state space charge limited currents with no trapping, the basic equations governing current flow are

(i) the boundary conditions $n(0) = \infty$, $E_{x'}(0) = 0$ (5.1)

where n(x') is the carrier concentration.

(ii) the continuity equation

$$J_{x'} = e\, n(x')\, \mu\, E_{x'}(x') = \text{independent of } x' \tag{5.2}$$

(iii) the Poisson equation

$$e\, n(x') = \varepsilon\varepsilon_o \frac{dE_{x'}(x')}{dx'} \tag{5.3}$$

(iv) an equation for the integral of the field strength

$$\int_o^{\ell} E_{x'}(x')\, dx' = V_L + V_D \tag{5.4}$$

Taking en(x') from eq.(5.3) and substituting into eq.(5.2) gives:

$$J_{x'} = \varepsilon\varepsilon_o\, \mu\, E_{x'}(x') \frac{dE_{x'}(x')}{dx'} = \varepsilon\varepsilon_o \frac{\mu}{2} \frac{d\left[E_{x'}(x')\right]^2}{dx'} \tag{5.5}$$

Integrating this equation and solving for $E_{x'}(x')$ gives:

$$E_{x'}(x') = \sqrt{\frac{2}{\mu\, \varepsilon\varepsilon_o}\, J_{x'}\, x'} \tag{5.6}$$

Inserting this result into eq.(5.4) and integrating, one obtains:

$$\sqrt{\frac{2\, J_{x'}}{\mu\, \varepsilon\varepsilon_o}}\, \frac{2}{3}\, \ell^{3/2} = V_L + V_D \tag{5.7}$$

Solving this equation for $J_{x'}$ gives:

$$J_{x'} = \varepsilon\varepsilon_o \frac{9}{8}\, \mu\, \frac{\left(V_L + V_D\right)^2}{\ell^3} \tag{5.8}$$

This equation is known as Child's law for the trap-free insulator. Substituting it into eq.(5.6) gives:

$$E_{x'}(x') = \frac{3}{2} \frac{\left(V_L + V_D\right)}{\ell} \left(\frac{x'}{\ell}\right)^{\frac{1}{2}} \tag{5.9}$$

The potential distribution is obtained by integrating eq.(5.9) from zero to x', remembering that $V(x'=0) = V_L$ and $V(x'=\ell) = -V_D$. The result is:

$$V_{x'}(x') = V_L - \left(V_L + V_D\right) \left(\frac{x'}{\ell}\right)^{3/2} \tag{5.10}$$

One can adjust V_L and V_D to make the Hall probe potential $V(x_o') = 0$. From eq.(5.10), one can then obtain the value of (x_o'/ℓ) at the Hall probes. The result for $V(x_o') = 0$ is:

$$\left(\frac{x_o'}{\ell}\right)^{3/2} = \frac{V_L}{V_L + V_D} = \left[\frac{(x_o + \ell/2)}{\ell}\right]^{3/2} \qquad (5.11)$$

This gives for (x_o/ℓ) the value

$$\frac{x_o}{\ell} = \left(\frac{V_L}{V_L + V_D}\right)^{2/3} - \frac{1}{2} \qquad (5.12)$$

and the electric field strength at the position of the Hall probes is obtained by substituting eq.(5.11) into eq.(5.9)

$$E_{x'}(x_o') = \frac{3}{2}\frac{\left(V_L + V_D\right)^{2/3}\left(V_L\right)^{1/3}}{\ell} = E_x(x_o) \qquad (5.13)$$

Carrier trapping causes the observed steady-state SCL current to be smaller than Child's current, often by many orders of magnitude[22]. However, as argued by Rose[23], neither the average space-charge density nor the field distribution should be strongly affected by trapping. Also, if a monoenergetic set of shallow traps[a] with a homogeneous spatial distribution is assumed[22], the voltage distribution along the crystal will be the same as that given by eq.(5.10)[23].

3b. Calculation of the Hall Voltage from the Measured Voltage

In order to account for the effect of finite sample dimensions and space charge effects, two parameters, G and S, are introduced in the following manner

$$V_H = \frac{2\,Vm}{G\,S} \qquad (5.14)$$

where G is the geometrical factor[24] due to the finite dimensions, and S is the space charge factor[25].

3c. Evaluation of G

The case where space charge effects are neglected can be defined by setting $S = 1$.

Because of the finite dimensions of the sample $E_y \neq E_H$, where E_H is the standard homogeneous field for an infinite parallel plate capacitor, given by:

$$E_H = \frac{V_H}{w}$$

Now it is assumed that E_y is independent of z. It is also assumed

[a] According to Helfrich[19], shallow has a relative meaning, denoting traps that are closer to the band than is the Fermi level.

that the field E_y results from a charge distribution located at $y = \pm \frac{1}{2} w$, $-\frac{1}{2}\ell \leq x \leq +\frac{1}{2}\ell$. Thus for the interior of the sample

$$\nabla . \vec{E}_y = 0 \qquad \text{and} \qquad \nabla \times \vec{E}_y = 0$$

As a result of the curl equation:

$$\vec{E}_y(x,y) = - \nabla V_y(x,y) \tag{5.15}$$

Therefore:

$$\nabla^2 V_y(x,y) = 0 \tag{5.16}$$

The boundary conditions to be satisfied are:

$$V_y(x, \pm \tfrac{1}{2} w) = \pm V_m \qquad (-\tfrac{1}{2}\ell \leq x \leq +\tfrac{1}{2}\ell)$$

$$E_y(x, \pm \tfrac{1}{2} w) = - V_H/w \qquad (-\tfrac{1}{2}\ell \leq x \leq +\tfrac{1}{2}\ell)$$

and

$$V_y(\pm \ell, y) = 0$$

A solution to eq.(5.16) satisfying the above boundary conditions has been obtained by Isenberg et al[24]:

$$V_y(x,y) = \frac{4\ell V_H}{\pi^2 w} \sum_{n=o}^{\infty} \frac{(-1)^n \sinh[(2n+1)\pi y/\ell] \cos[(2n+1)\pi x/\ell]}{(2n+1)^2 \{\cosh (2n+1)\pi w/2\ell\}} \tag{5.17}$$

Since $2 V_m = V_y(x, \frac{1}{2} w) - V_y(x, -\frac{1}{2} w)$ and $\sinh(A) = - \sinh(-A)$, eq.(5.17) gives:

$$2 V_m = V_H \left[\frac{8\ell}{\pi^2 w} \sum_{n=o}^{\infty} \frac{(-1)^n \tanh[(2n+1)\pi w/2\ell] \cos[(2n+1)\pi x/\ell]}{(2n+1)^2} \right] \tag{5.18}$$

G is obtained by comparing eqs.(5.18) and (5.14)

$$G = \frac{8\ell}{\pi^2 w} \sum_{n=o}^{\infty} \frac{(-1)^n \tanh[(2n+1)\pi w/2\ell] \cos[(2n+1)\pi x/\ell]}{(2n+1)^2} \tag{5.19}$$

The value of G of interest will be that for which $(x/\ell) = (x_o/\ell)$, where the Hall probe potential is zero

$$\frac{x_o}{\ell} = \left(\frac{V_L}{V_L + V_D} \right)^{2/3} - \frac{1}{2} \tag{5.12}$$

The series for G rapidly converges.

3d. Evaluation of S

In the (y,z) plane defined by eq.(5.12), the density of charge carriers is assumed to be a function of y only. Therefore, the steady-state continuity equation for this plane is:

$$J_y = e\, n\, \mu_y\, E_y + e\, n\, \mu_y\, \mu_H\, E_x\, B_z - e\, D \left(\frac{dn}{dy}\right) = 0 \qquad (5.20)$$

where μ_y is the drift mobility in the y direction, μ_H is the Hall mobility given in eq.(4.12), and D is the diffusion constant for the charge carrier. Solving for $\frac{dn}{dy}$ and letting $E_y = -\frac{dV_y}{dy}$, one gets:

$$\frac{dn}{dy} = \left(\frac{\mu_y n}{D}\right)\left[\mu_H\, E_x\, B_z - \frac{dV_y}{dy}\right] \qquad (5.21)$$

This may be integrated to give:

$$\ln\left(\frac{n}{n_o}\right) = -\left(\frac{\mu_y}{D}\right) V_y + \left(\frac{\mu_y\, \mu_H\, E_x\, B_z}{D}\right) y \qquad (5.22)$$

where n_o is the carrier concentration for zero magnetic field. Within the dielectric material, one has:

$$\frac{dE_y}{dy} = \frac{e}{\epsilon_y \epsilon_o}\,(n - n_o) \qquad (5.23)$$

where ϵ_y is the dielectric constant in the y direction. From eqs.(5.22) and (5.23) one obtains:

$$-\frac{d^2 V_y}{dy^2} = \frac{e}{\epsilon_y \epsilon_o}\, n_o \left[\exp\left[-\left(\frac{\mu_y\, V_y}{D}\right) + \left(\frac{\mu_y\, \mu_H\, E_x\, B_z}{D}\right) y\right] - 1\right] \qquad (5.24)$$

The boundary conditions for eq.(5.24) are:

$$V_y(0) = 0 \qquad (5.25)$$

and

$$\left(\frac{dV_y}{dy}\right)_{y=\pm\frac{1}{2}w} = 0 \qquad (5.26)$$

Equation (5.25) follows from symmetry considerations, while eq.(5.26) involves the neglect of edge effects due to the finite extension of the sample in the x and z directions. Banbury et al[25] obtained as the solution to eq.(5.24):

$$V_y = V_H\left[\left(\frac{y}{w}\right) - \left(\frac{L}{w}\right)\frac{\sinh(y/L)}{\cosh(w/2L)}\right] \qquad (5.27)$$

But, since $2\,V_m = V_y(+\frac{1}{2}w) - V_y(-\frac{1}{2}w)$, one obtains the relation:

$$2\,V_m = V_H\,S = V_H\left[1 - \left(\frac{2L}{w}\right)\tanh\left(\frac{w}{2L}\right)\right] \tag{5.28}$$

This gives for S

$$S = 1 - \left(\frac{2L}{w}\right)\tanh\left(\frac{w}{2L}\right) \tag{5.29}$$

where L is

$$L = \left[\varepsilon_y\varepsilon_o\left(\frac{kT}{e}\right)\left(\frac{2t}{\eta}\right)\left(\frac{\mu_x}{I_x}\right)\right]^{\frac{1}{2}} \tag{5.30}$$

I_x being the photo-current of the photo-injected charge carriers, and η is given by:

$$\eta = \frac{2}{w\,E_x} \tag{5.31a}$$

where the value of E_x is the one calculated at the position of the Hall probe; for $(x/\ell) = (x_o/\ell)$, E_x is given by eq.(5.13), and thus

$$\eta = \frac{4}{3}\left(\frac{\ell}{w}\right)\frac{1}{(V_L)^{1/3}\left(V_L + V_D\right)^{2/3}} \tag{5.31b}$$

3e. Calculation of the Hall Mobility

From $$\mu_H = \frac{V_H}{w\,E_x\,B_z} \tag{4.12}$$

and $$V_H = \frac{2\,V_m}{G\,S} \tag{5.14}$$

and eq.(5.31a), one obtains:

$$\mu_H = \left(\frac{\eta}{G\,S}\right)\left(\frac{V_m}{B_z}\right) \tag{5.32}$$

If μ_H is to be expressed in terms of $cm^2/V\text{-sec}$, V_m in millivolts, B_z in kilogauss, and η in V^{-1} , eq.(5.32) must be written as:

$$\mu_H = \left(\frac{100\,\eta}{G\,S}\right)\left(\frac{V_m}{B_z}\right) \tag{5.33}$$

4. Techniques and Results

After the high-pressure cell was introduced in the pole gap and the electronic system connected, argon was allowed to flow into the high-pressure

system, in order to keep the naphthalene crystal at a pressure of about 10 atmospheres, to slow the sublimation process.

The leakage current was then checked; this was usually of the order of 10^{-13} amperes or less, and provided a check on the integrity of the insulation and isolation of the electrical contacts, as well as the cleanliness of the delrin base (fig. 5.6) and the surfaces of the lucalox rings (fig. 5.5). Similar crystals were reported by Spielberg[21] to have dark current values of the order of 10^{-15} to 10^{-14} amperes. However, due to the small sizes involved in this experiment (the sample holder was about half the size of the one used by Spielberg and the crystal dimensions were correspondingly smaller), leakage currents prevented an accurate determination of the dark current.

The guard ring was effective in eliminating surface currents. With the guard ring absent, the photo-current was typically an order of magnitude larger.

The usual method of performing the Hall effect measurement starts with adjusting the potential of the dark electrode, V_D , so that one of the Hall probe potentials is zero with respect to ground potential; the bucking potentiometers are then used to eliminate the unbalance of the Hall probes. However, it was found that the use of power supplies in the circuit, caused instabilities in both the photo-current and the Hall probe potential. Therefore, all three electrodes (the illuminated electrode, the guard ring and the dark electrode) were connected to batteries.

In addition, it was also found that the use of the current electrometer on the dark electrode side of the sample, caused a considerable reduction in the measured dark current, due to the elimination of the surface currents flowing between the illuminated electrode and the guard ring.

Finally, only the lower Hall probe (on the surface opposite to the one facing the stack) could be adjusted to have a small enough drift to make a measurement possible.

The measurement was carried out by allowing for a sufficiently slow rate of drift to be achieved at the Hall probe; at that point, the recorder trace would indicate a zero magnetic field baseline. The magnetic field was then turned on, and as quickly as possible brought up to a full strength. The time required to achieve full field was typically 10 to 20 seconds. The recorder would monitor the build-up in the Hall probe potential, until

saturation occured. The probe would then resume drifting with the slope of the initial drift for zero magnetic field. When the magnetic field was turned off, the Hall probe potential would revert back to the zero field baseline. A typical recorder trace is shown in fig. 5.10 .

It was found that the Hall probe potential did not reverse its sign upon reversing the direction of the magnetic field. The Hall voltage corresponding to a certain value of the magnetic field, was therefore taken to be the difference between the two signals obtained with the field in the normal and reverse directions, respectively.

Among the six possible relative orientations of the electric and magnetic field directions, it was found that for the crystal geometry used, only two combinations of $\vec{E}$ and $\vec{B}$ fields gave reliable measurements of the Hall probe signal. These were for the electric field in the a direction and the magnetic field in the b direction, or vice versa, and thus resulted in the determination of the Hall mobilities μ_{12} and μ_{21} , following the notation given in chapter four.

Measurements of the Hall probe potential were carried out at various values of the magnetic field, and the results were plotted as a function of field strength. Using a least-squares fitting routine, straight lines were found to provide a good fit to the data obtained from each direction of the magnetic field (normal or reverse). The Hall voltage as a function of field strength, was then obtained as the difference between the two lines corresponding to the normal and reverse directions of the magnetic field.

The Hall mobilities were computed from eq.(5.33), where η is calculated from eq.(5.31a), S from eq.(5.29), and G from eq.(5.19). For the evaluation of L in the expression of S, the dielectric tensor of naphthalene single crystals was required. This was measured by Munn and Williams[26] and is given in table 5.1 .

The results obtained at atmospheric pressure are given in tables 5.2 and 5.3 . Figures 5.11 and 5.12 are plots of the data shown in table 5.2 , while figs. 5.13 and 5.14 correspond to the data given in table 5.3 .

Measurements of the Hall mobility μ_{12} (current along the a direction and magnetic field along the b direction) were carried out at a pressure of 2.2 kilobars, and for magnetic field strengths of 16 kilogauss. The resulting data are given in table 5.4 . To calculate L, as given by eq.(5.30),

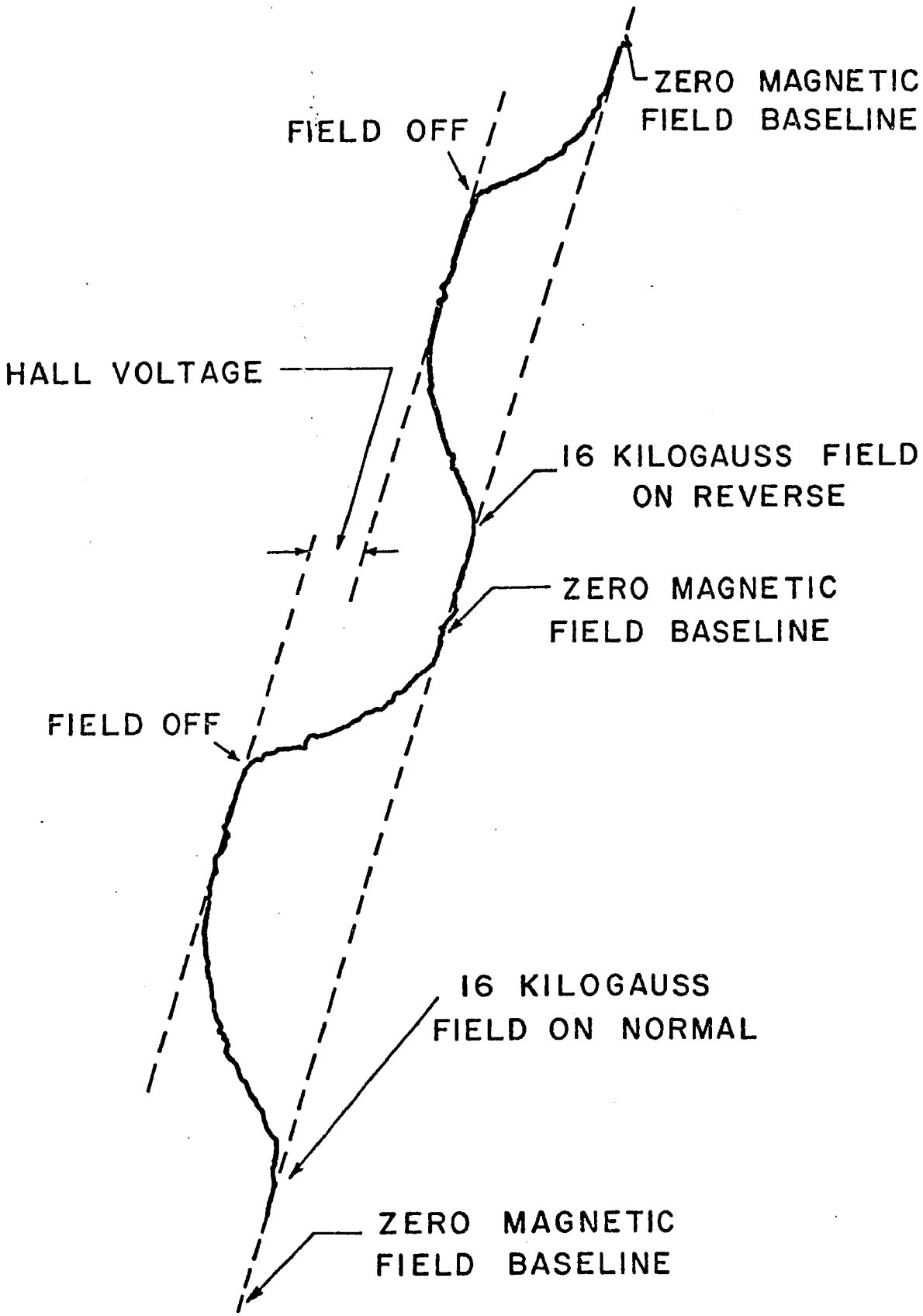

FIG. 5.10

Table 5.1 - Dielectric constant of naphthalene in the three crystallographic directions[26].

Crystal direction	Dielectric constant
a	2.65 ± 0.06
b	2.87 ± 0.05
c'	3.21 ± 0.07

Table 5.2 - Experimental data for the Hall mobility μ_{21} (current parallel to b, magnetic field parallel to a) at atmospheric pressure.

V_L (volt)	V_D (volt)	Photocurrent (10^{-12}amp)	V_m/B_z (mv/kg)	S	G	μ_H (cm^2/V-sec)
70	70	0.25	0.044	0.00337	0.937	40 ± 9

V_L is the positive bias applied to the illuminated electrode.

V_D is the negative bias applied to the collecting electrode.

V_m is the Hall voltage.

B_z is the magnetic field intensity.

S is the factor due to space charge effects.

G is the geometrical factor due to the finite dimensions of the sample.

Table 5.3 - Experimental data for the Hall mobility μ_{12} (current parallel to a, magnetic field parallel to b) at atmospheric pressure.

V_L (volt)	V_D (volt)	Photocurrent (10^{-12} amp)	V_m/B_z (mv/kg)	S	G	μ_H (cm^2/V-sec)
70	70	0.16	0.0025	0.0034	0.937	2.3 ± 1.2

V_L is the positive bias applied to the illuminated electrode.

V_D is the negative bias applied to the collecting electrode.

V_m is the Hall voltage.

B_z is the magnetic field intensity.

S is the factor due to space charge effects.

G is the geometrical factor due to the finite dimensions of the sample.

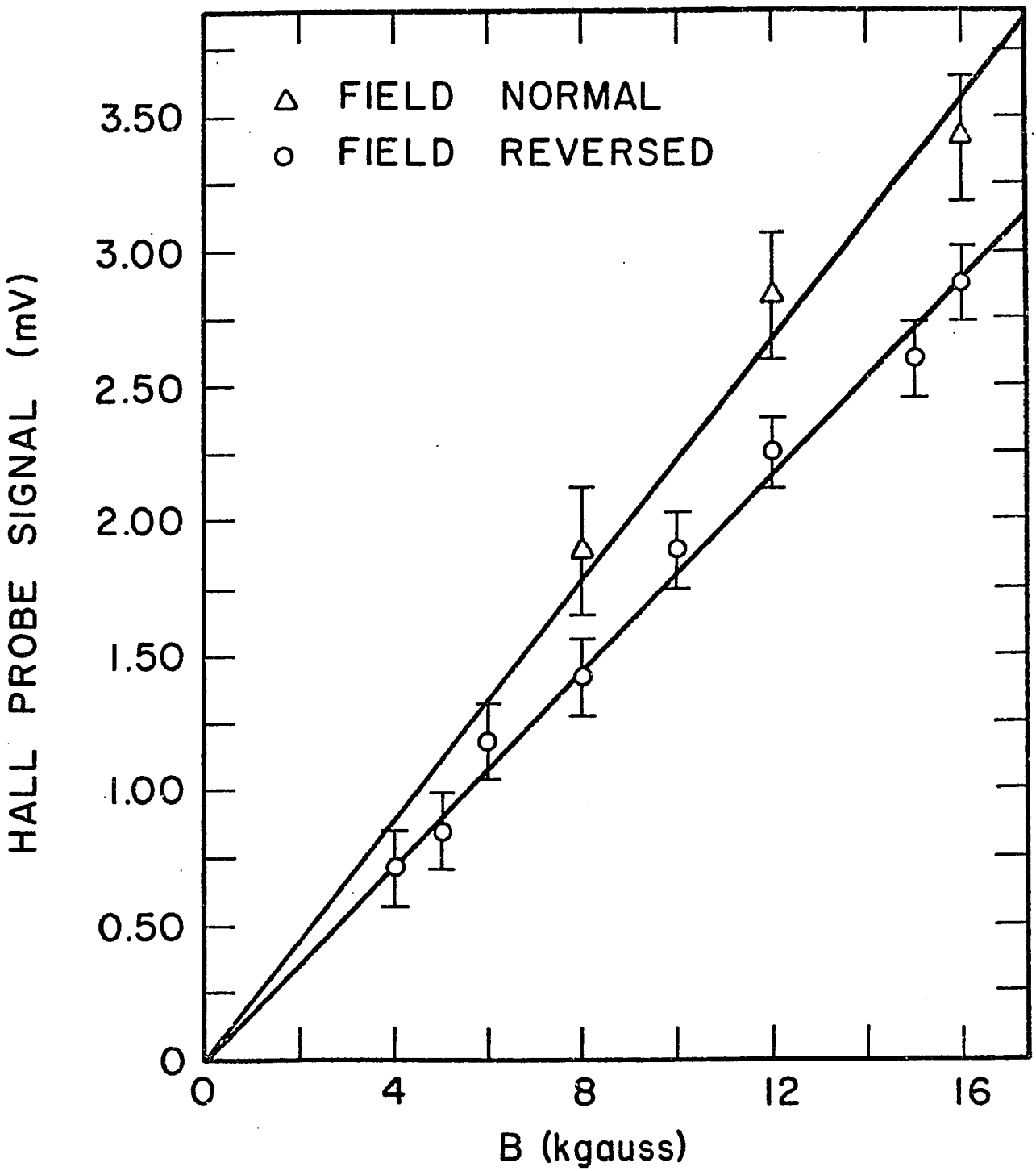

FIG. 5.11

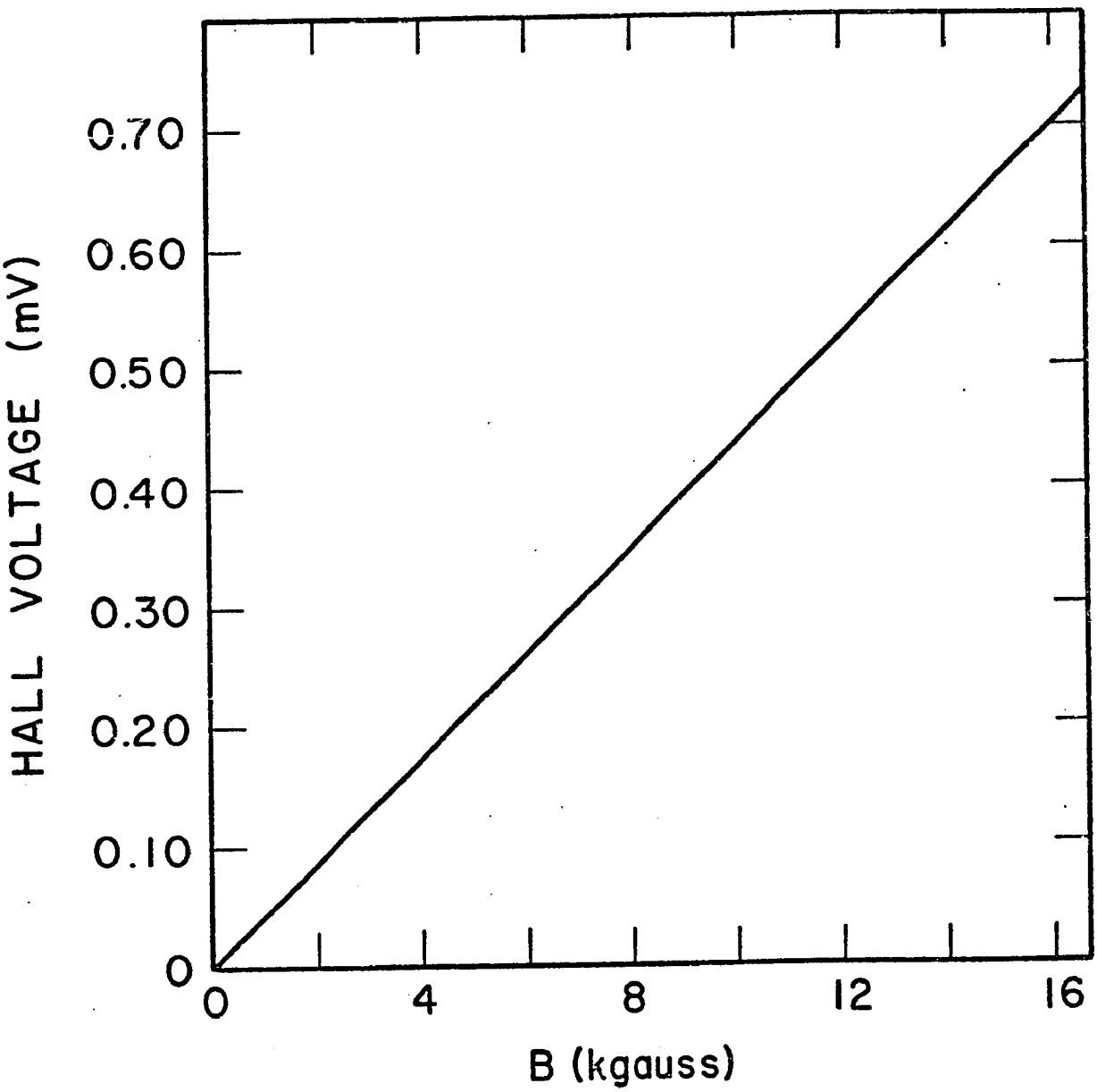

FIG. 5.12

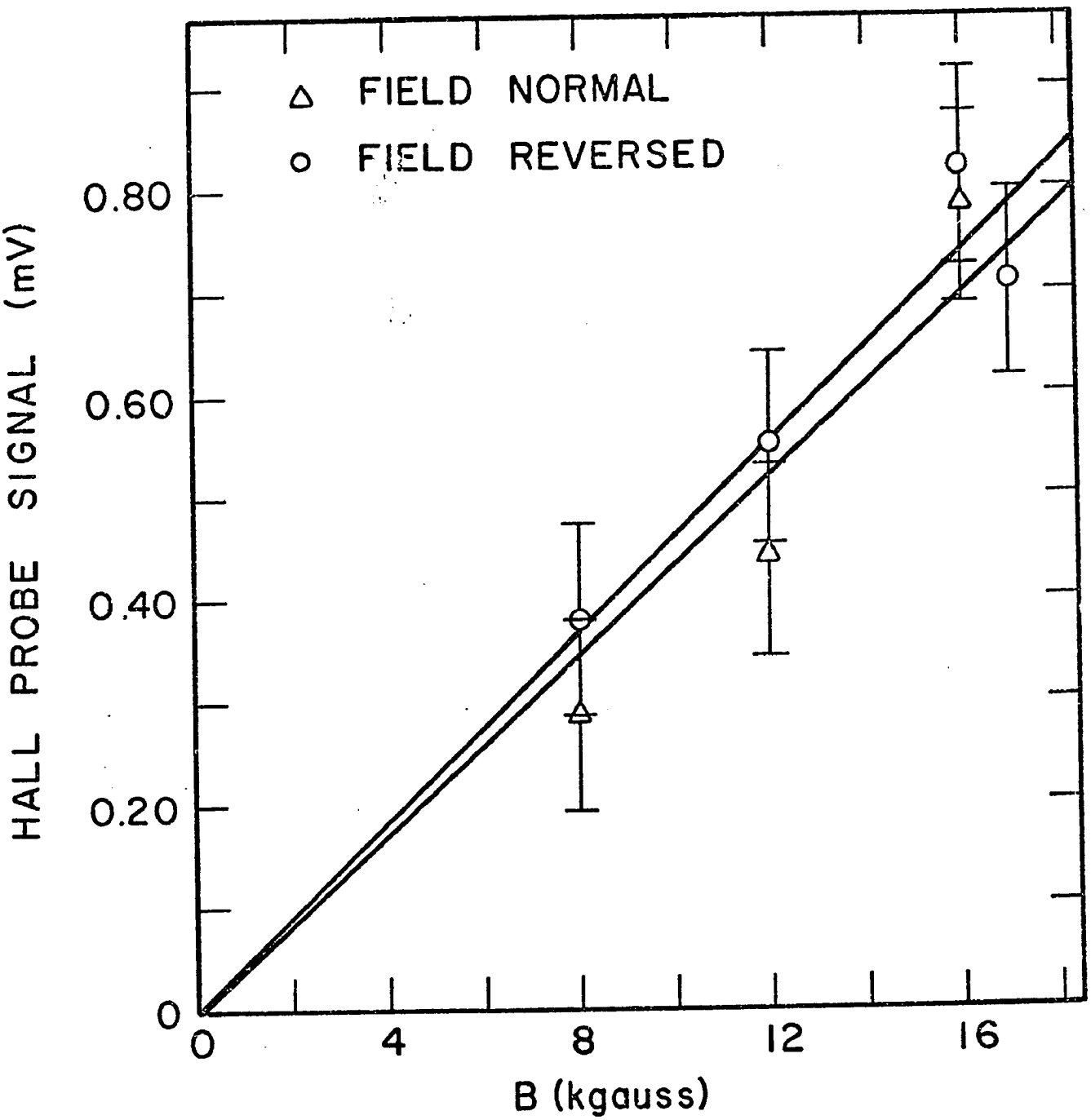

FIG. 5.13

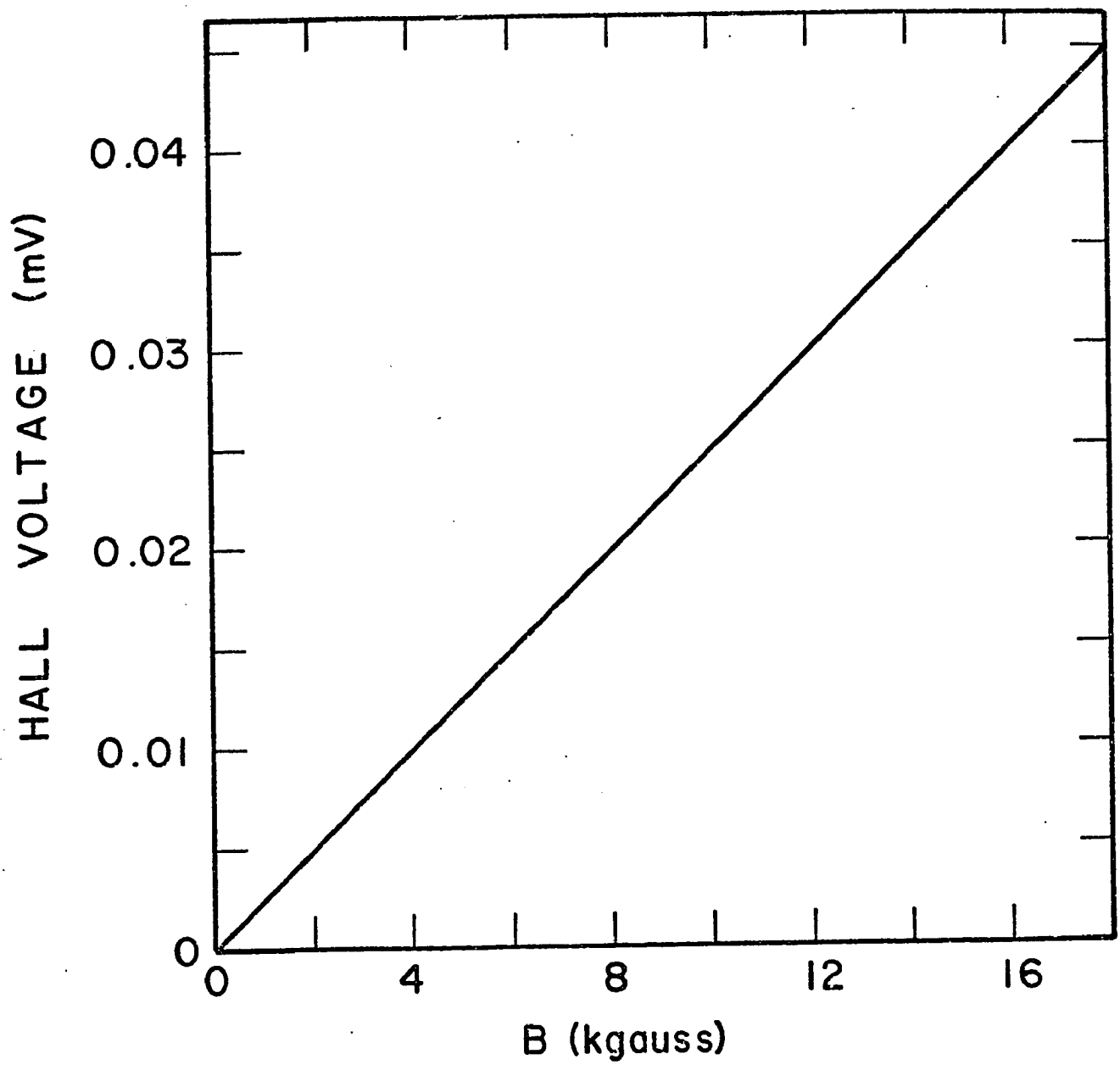

FIG. 5.14

Table 5.4 - Experimental data for the Hall mobility μ_{12} (current parallel to a, magnetic field parallel to b) at atmospheric pressure and at 2.2 kilobars.

V_L (volt)	V_D	Photocurrent (10^{-12}amp)	V_m/B_z (mv/kg)	S	G	μ_H (cm^2/V-sec)
			Atmospheric pressure			
70	70	0.25	0.0031	0.0052	0.937	1.9 ± 0.7
			2.2 kilobars			
70	70	0.17	0.0027	0.0029	0.937	2.9 ± 1.1

V_L is the positive bias applied to the illuminated electrode.

V_D is the negative bias applied to the collecting electrode.

V_m is the Hall voltage.

B_z is the magnetic field intensity.

S is the factor due to space charge effects.

G is the geometrical factor due to the finite dimensions of the sample.

the value of μ_x (μ_{aa}) at 2.2 kilobars was required. However, since there are no available data on the drift mobility tensor of naphthalene at high pressures, the value of μ_{aa} at 2.2 kilobars was taken from figs. 4.13 and 4.14 , which give the variation with pressure of the drift mobility tensor components in the constant τ and constant λ approximations, respectively.

Table 5.4 also gives the ratio of the Hall mobility μ_{12} at 2.2 kilobars to its value at atmospheric pressure.

No reliable measurements could be made for the Hall effect of electrons, because the two Hall signals obtained with the magnetic field in the normal and reverse directions, were almost equal.

5. Discussion

The absence of reversal in the sign of the Hall probe potential, upon reversing the direction of the magnetic field, has also been observed by Dresner[4,5] in the measurement of the photo-Hall effect of holes in anthracene. He explained this effect as being due to the presence of surface defects in his samples.

In the present work, the absence of reversal is interpreted in terms of the interaction between a triplet exciton (produced by intersystem crossover from a singlet state) and a trapped hole, in which process the triplet exciton is annihilated. In the presence of an external magnetic field, the triplet exciton-trapped hole interaction decreases, thus resulting in a change of the potential distribution in the crystal, including the region of the Hall probe. This change is larger than the actual Hall voltage, and its sign is independent of the direction of the magnetic field.

This interpretation is supported by the observation that when the injected carriers were electrons, the sign of the Hall probe potential was opposite to that obtained when holes were the injected carriers, thus indicating an interaction between triplet excitons and trapped electrons.

The interaction between triplet excitons and trapped carriers was first presented by Geacintov et al[27] and by Frankevich et al[28], to explain the magnetic field effect on the change in photoconductivity of anthracene, then, more recently, by Bouchriha et al[29] and Pope et al[30] to interpret similar effects in pyrene and tetracene, respectively. Bouchriha et al[31] measured a decrease in the triplet exciton-trapped hole interaction, in

anthracene, of up to 9% at 4.2 kilogauss.

Ern et al[32] and Weisz et al[33] used similar arguments, to interpret the change in triplet exciton quenching rate with the concentration of carriers injected in anthracene.

Referring back to tables 5.2 and 5.3 , it can be seen that the Hall mobilities of holes, μ_{12} and μ_{21} , both have a positive sign (non-anomalous effect). By comparing this result with the calculations that were carried out using the various band models (tables 4.7 to 4.12), one notices that only one model predicts positive Hall mobilities of holes, μ_{12} and μ_{21} ; this is the band model corresponding to table 4.12 , which takes into consideration the resonance integrals as well as the exchange and vibrational effects, in the constant λ approximation.

This conclusion is confirmed when the ratio

$$\frac{\mu_{12}\big|_{2.2\text{Kb.}}}{\mu_{12}\big|_{\text{atm.}}} = 1.6$$

is compared with the values predicted by the various band models. It can be seen that all calculations carried out in the constant λ approximation (tables 4.8, 4.10 and 4.12) give an increase of 17-48% in the value of μ_{12} at 2.2 kilobars, while the calculations done in the constant τ approximation (tables 4.7, 4.9 and 4.11) do not all predict a consistent variation with pressure for μ_{12}. These results are summarized in table 5.5 .

From tables 4.11 and 5.5, it can be seen that calculations carried out in the constant τ approximation, and taking into consideration the exchange and vibrational effects, give a non-anomalous value for μ_{12} (holes), as well as the correct variation with pressure; however, such a calculation gives a negative sign for μ_{21} (holes), contrary to the experimental data. Table 5.5 also shows that calculations done in the constant λ approximation, using only the resonance integrals, predict a variation of μ_{12} with pressure ($\sim$ 1.48) close to the experimental value of 1.6 . However, such a calculation (see table 4.10) fails to predict the positive sign for the Hall mobilities of holes, μ_{12} and μ_{21} .

On the other hand, the discrepancy between the experimental value of 1.6 and the value 1.17 calculated in the constant λ approximation (exchange and vibrational effects taken into consideration), can be ex-

Table 5.5 - Comparison between the values of μ_{12} , at 2.2 kilobars, in the various band models.

Constant λ			Constant τ			Exp.
2-center only	2-and 3 center	(IRS-IE).F	2-center only	2-and 3 center	(IRS-IE).F	
1.32	1.48	1.17	0.84	0.54	1.71	1.6 ± 70%

plained by the uncertainties occuring in the measurement of the Hall mobility μ_{12} (see table 5.4).

The available Hall mobility data thus suggest that calculations carried out in the constant λ approximation, using a band model and taking into consideration the resonance and exchange integrals, as well as the vibrational overlap, predict the correct sign for the Hall mobilities of holes in naphthalene. However, due to the large uncertainties, the variation with pressure of the Hall mobility μ_{12} cannot be used alone to favor one band model over the other.

These results, along with similar conclusions regarding the drift mobility tensor (see chapter four), thus seem to favor a band conduction mechanism in naphthalene, where the mean free path, rather than the mean free time, is constant.

References - Chapter 5

1. R.G. Kepler, Organic Semiconductors, (Eds. J.J. Brophy and J.W. Buttrey), MacMillan, New York, 1962.

2. T. Kajiwara, H. Inokuchi and S. Minomura, Bull. Chem. Soc. Japan, 40, 1055 (1967).

3. D.H. Spielberg, A.I. Korn and A.C. Damask, Phys. Rev. B, 3, 2012 (1971).

4. J. Dresner, Phys. Rev., 143, 558 (1966).

5. J. Dresner, J. Chem. Phys., 52, 6343 (1970).

6. G. Delacote and M. Schott, Solid State Comm., 4, 177 (1966).

7. G. Delacote, Ph.D. Thesis, Universite de Paris, 1968.

8. E.L. Frankevich and E.I. Balabanov, Soviet Phys.- Solid State, 8, 682 (1966).

9. R. Pethig and K. Morgan, Nature, 214, 266 (1967).

10. T. Toombs, Ph.D. Thesis, Princeton University, 1968.

11. G.C. Smith, Phys. Rev., 185, 1133 (1969).

12. A.G. Redfield, Phys. Rev., 94, 526 (1954).

13. M. Schadt and D.F. Williams, Phys. Stat. Sol., 39, 223 (1970).

14. A.I. Korn, R.A. Arndt and A.C. Damask, Phys. Rev., 186, 938 (1969).

15. A.I. Korn, Ph.D. Thesis, City University of New York, 1969.

16. P.W. Bridgman, The Physics of High Pressure, p 70, Dover Publications, Inc., New York, 1970.

17. O.H. Leblanc, Jr., Physics and Chemistry of the Organic Solid State, vol 3, (Eds. D. Fox, M.M. Labes and A. Weissberger), Wiley-Interscience, New York, 1967.

18. M. Pope and H. Kallmann, Disc. Faraday Soc., 51, 7 (1971).

19. W. Helfrich, Physics and Chemistry of the Organic Solid State, vol 3, (Eds. D. Fox, M.M. Labes and A. Weissberger), Wiley-Interscience, New York, 1967.

20. N.F. Mott and R.W. Gurney, Electronic Processes in Ionic Crystals, Clarendon Press, Oxford, England, 1940.

21. D.H. Spielberg, Ph.D. Thesis, City University of New York, 1970.

22. M. Campos, Molec. Cryst. Liq. Cryst., 18, 105 (1972).

23. A. Rose, Phys. Rev., 97, 1538 (1955).

24. I. Isenberg, B.R. Russel and R.F. Greene, Rev. Sci. Inst., 19, 685 (1949).

25. P.C. Banbury, H.K. Henisch and A. Many, Proc. Phys. Soc., 66A, 753 (1953).

26. R.W. Munn and D.F. Williams, J. Chem. Phys., 59, 1742 (1973).

27. N.E. Geacintov, M. Pope and S. Fox, J. Phys. Chem. Solids, 31, 1375 (1970).

28. E.L. Frankevich and I.A. Sokolik, Solid State Commun., 8, 251 (1970).

29. H. Bouchriha, M. Schott and J.L. Fave, J. Phys. (Paris), 36, 399 (1975).

30. M. Pope and Y. Solowiejczyk, Molec. Cryst. Liq. Cryst., 30, 175 (1975).

31. H. Bouchriha, G. Delacote, P. Delannoy and M. Schott, J. Phys. (Paris), 35, 577 (1974).

32. V. Ern, H. Bouchriha, J. Fourny and G. Delacote, Solid State Commun., 9, 1201 (1971).

33. S.Z. Weisz, J. Levinson and A. Cobas, Proc. Third International Conference on Photoconductivity, 297 (Ed. E.M. Pell), Pergamon Press, Oxford and New York, 1971

Appendix

A Comparison Between the Band Model Descriptions for Naphthalene and Anthracene

The anisotropy of the drift mobility tensor of naphthalene at atmospheric pressure (see chapter four) is compared with similar results obtained for anthracene[1]. The last two columns of table A.1 show the various drift mobility ratios in the anisotropic τ and the anisotropic λ approximations; in the anisotropic approximation, the relaxation time τ and the mean free path λ for each drift mobility component are taken to be inversely proportional to the corresponding bandwidth.

From this table it can be seen that calculations carried out in the anisotropic λ approximation give, in general, a better agreement with the experimental anisotropies of the drift mobility tensor at atmospheric pressure, for both anthracene and naphthalene. For anthracene, the improvement resulting from the use of the anisotropic λ approximation is mainly in the calculated drift mobility component of electrons in the c' direction, while the calculated components in the a and b directions in the anisotropic τ approximation are very close to the corresponding values calculated in the anisotropic λ approximation.

On the other hand, table A.2 shows that calculations done in the constant τ approximation give a closer agreement with Kepler's[3] measurements of the pressure dependence of the drift mobility tensor of anthracene. Therefore, calculations of the drift mobility tensor of anthracene in the constant τ approximation give in general a closer agreement with the corresponding experimental data, though not for the mobility component of electrons in the c' direction.

For naphthalene, it has been shown in chapters four and five that the available drift mobility data at atmospheric pressure, and Hall mobility data at atmospheric pressure and at 2.2 kilobars, seem to favor a band conduction mechanism, where the mean free path, rather than the mean free time, is constant.

Table A.1 - Comparison of the drift mobility ratios for naphthalene and anthracene in the anisotropic τ and the anisotropic λ approximations[a].

Ratio	B.W. ratios[b]	Exp.[c]	Mobility ratios const.τ[d]	const.λ[d]	anisot.τ[e]	anisot.λ[e]
			NAPHTHALENE			
			Hole			
bb/aa	8.019	1.55	16.471	14.916	2.054	1.860
c c/aa	5.560	0.73	2.947	2.835	0.530	0.510
			Electron			
bb/aa	1.000	1.02	0.619	0.637	0.619	0.637
cc/aa	0.099	0.97	0.026	0.044	0.261	0.439
			ANTHRACENE			
			Hole			
bb/aa	2.403	2.00	2.141	2.036	0.891	0.847
cc/aa	1.296	0.80	0.448	0.544	0.346	0.419
			Electron			
bb/aa	1.006	0.59	0.663	0.641	0.659	0.637
cc/aa	0.040	0.24	0.001	0.002	0.023	0.047

[a] The data for naphthalene were reproduced from table 4.13 .

[b] The bandwidth ratios for anthracene were taken from reference 1.

[c] The values for anthracene are the drift mobility data given in reference 2.

[d] The drift mobility ratios for anthracene were taken from reference 1.

[e] All values in the last two columns were obtained by multiplying the corresponding mobility ratios in the constant τ or constant λ approximations (fourth and fifth columns respectively) by the reciprocal of the bandwidth ratio given in the second column.

Table A.2 - The pressure dependence of the electron and hole drift mobility in anthracene[a].

	Electron $\mu_{3kb}/\mu_{atm.}$			Hole $\mu_{3kb}/\mu_{atm.}$		
	Exp.	Calc.		Exp.	Calc.	
Crystal direction		const.τ	const.λ		const.τ	const.λ
a	1.40	1.14	1.07	1.40	1.05	0.98
b	1.30	1.14	1.06	1.40	1.17	1.08
c'	1.00	2.70	2.61	1.40	1.41	1.26

[a] The experimental data were taken from reference 3, and the calculated values from reference 1.

References - Appendix

1. S. Elnahwy, Ph.D. Thesis, City University of New York, 1976.

2. R.G. Kepler, Phys. Rev., 119, 1226 (1960).

3. R.G. Kepler, Organic Semiconductors, (Eds. J.J. Brophy and J.W. Buttrey), MacMillan, New York, 1962.